



KTH ROYAL INSTITUTE
OF TECHNOLOGY

Doctoral Thesis in Geodesy

Monitoring lithospheric motions by Satellite geodesy

Nureldin Ahmed Adam Gido

TRITA-ABE-DLT-2023
ISBN: 978-91-7873-586-0

Monitoring lithospheric motions by Satellite geodesy

Nureldin Ahmed Adam Gido

Academic Dissertation which, with due permission of the KTH Royal Institute of Technology, is submitted for public defence for the Degree of Doctor of Philosophy on Friday the 18th September 2020, at 10:00 a.m. in Kollegiesalen, Brinellvägen 8, Stockholm

Doctoral Thesis in Geodesy
KTH Royal Institute of technology
Stockholm, Sweden, 2020

© Nureldin Ahmed Adam Gido, 2020

TRITA-ABE-DLT-2023

ISBN: 978-91-7873-586-0

Printed by: Universitetsservice US-AB, Sweden 2020

Abstract

Understanding of global and local Earth's dynamic processes is of great importance to the Earth's system knowledge, human life, and sustainability goals (e.g. climatic change and geo-hazard assessment, etc.). The processes are largely affected by the Earth's mass distribution and redistribution, which can be quantified and modelled using simultaneous and complementary data from various geoscience and environmental near earth-orbiting artificial satellites. In this thesis, which is based on five peer-reviewed papers, we study the lithospheric motion and the Earth's mass change in terms of gravity variation, using a combination of geodetic satellite data and non-geodetic observations.

The first paper is concerned with using of gravimetric approach to model sub-crustal horizontal stresses in the Earth's mantle and their temporal changes using the Gravity Recovery and Climate Experiment (GRACE) data, caused by geodynamical processes such as mantle convection, in Fennoscandia region. We show that the determined horizontal stresses obtained by a gravimetric method are consistent with tectonics and seismic activities. In addition, the secular rate of change of the horizontal stress, which is within 95 kPa/year, is larger outside the uplift dome than inside in the study area.

In the second paper, permafrost thawing and its associated gravity change, in terms of groundwater storage (GWS) anomalies changes is studied using the GRACE data and other satellites (e.g. AIRS) and ground-based observations in the northern high-latitude regions. The results of a preliminary numerical analysis reveal a high correlation between the secular trends of greenhouse gases (CO_2), temperature, and the equivalent water thickness in the selected regions. Furthermore, the GRACE-based GWS estimates attributed to the permafrost thawing is increased at the annual rates of 3 to 4 cm/year in selected study areas.

The third paper investigates the large-scale GRACE-based GWS changes together with different hydrological models over the major oil reservoirs in Sudan. The outcomes are correlated with the available oil wells production data. Moreover, using the freely available Sentinel-1 data, the ground surface deformation associated with oil and water depletion is studied. Our results show that there is a significant correlation between the GRACE-based GWS anomalies and the extracted oil and water volumes. The trend of GWS anomaly changes due to water and oil depletion varies from -18.5 ± 6.3 to -6.2 ± 1.3 mm/year using the CSR GRACE monthly solutions and the best tested hydrological model in this study. Moreover, our Sentinel-1 Synthetic Aperture Radar (SAR) data analysis using Persistent Scatterer Interferometry (PSI) method shows high rate of subsidence, i.e. -24.5 ± 0.85 , -23.8 ± 0.96 , -14.2 ± 0.85 and -6 ± 0.88 mm/year, over the selected study area.

In the fourth paper, a combined Moho model using seismic and gravity data is determined to investigate the relationship between the isostatic state of the lithosphere and seismic activities in the study area (which includes East Africa, Egypt, Congo and Saudi Arabia). Our results show that isostatic equilibrium and compensation state are closely correlated to the seismicity patterns in the study area. This paper presents a method to determine the crustal thickness and crust-mantle density contrast, and consequently one can detect low-density contrast (about 200 kg/m^3) and thin crust (about 30 km) near the triple junction plate tectonics in East Africa (Afar triple junction), which confirms the state of over-compensation in the rift valley areas. Furthermore, the density contrast structure of the crust-mantle shows a large correlation with the earthquake activity, sub-crustal stress and volcanic distribution across East Africa.

The fifth and last paper investigates the ground surface deformation of Gävle city in Sweden using Sentinel-1 data and PSI technique, as well as analyzing the historical leveling data. The PSI technique is used to map the location of risk zones, and their ongoing subsidence rate. Our PSI analysis reveals that the centre of Gävle city is relatively stable with minor deformation ranging between -2.0 mm/year and $+2.0 \text{ mm/year}$ in the vertical and East-West components. Furthermore, the land surface toward the northeast of the city is significantly subsiding with an annual rate of about -6 mm/year . The comparison at sparse locations shows a close agreement between the subsidence rates obtained from precise leveling and PSI results. The regional quaternary deposit distribution was correlated with PSI results, and it shows that the subsidence areas are mostly located in zones where the sub-surface layer is marked by artificial fill materials.

Sammanfattning

Förståelsen av globala och lokala dynamiska processer på jorden har stor betydelse för vår kännedom om olika förlopp av betydelse för liv och hållbarhetsmål på planeten (t.ex. klimatförändringar, geo-riskbedömning, etc.). Processerna påverkas till stor del av jordens olika typer av massfördelning och dessas förändringar i tiden, som kan kvantifieras och modelleras med hjälp av samtidiga och kompletterande data från olika vetenskaper, särskilt geovetenskaper som utnyttjar artificiella satelliter. I denna avhandling, som är baserad på fem vetenskapligt granskade artiklar, studerar vi massförändringar i litosfären (dvs jordskorpan och övre manteln) och även deformationer i skorpan som registreras som tyngdkraftsvariationer i kombinationer med data från bl.a. geodetiska satelliter.

I den första uppsatsen studeras horisontella tektoniska spänningar i jordens mantel i Fennoscandia och dessas förändringar i tiden orsakade av geodynamiska processer med hjälp av data från satellitprojektet Gravity Recovery and Climate Experiment (GRACE). Vi visar att de beräknade spänningarna överensstämmer med de tektoniska och seismiska aktiviteterna. Den sekulära förändringshastigheten för den horisontella spänningen, som ligger inom 95 kPa/år, visar sig vara större utanför landhöjningskupolen än inne i studieområdet.

I den andra uppsatsen studeras avsmältningen av permafrost i polartrakterna och de tyngdkraftsförändringar som därav följer i termer av förändringar av grundvattenlagring (Δ GWS). Även här används GRACE-data, men också observationer från andra satelliter och markbaserade instrument i de nordliga polartrakterna. Resultaten av en preliminär numerisk analys avslöjar en hög korrelation mellan de sekulära trenderna för växthusgasen CO_2 , temperatur och ekvivalent vattennivån i de utvalda regionerna. Vidare ökar de GRACE-baserade GWS-uppskattningarna, som hänför sig till permafrostens avsmältning, med hastigheter av 3 - 4 cm/år.

Den tredje artikeln undersöker de storskaliga GWS-förändringarna baserade på data från GRACE och olika hydrologiska modeller över de stora oljereservoarerna i Sudan. Resultaten är korrelerade med tillgängliga produktionsdata för oljebrunnar. Med användning av fritt tillgängliga data från satelliten Sentinel-1 studeras dessutom deformationsytan på marken, som är förknippad med olje- och vattenutarmning. Våra resultat visar att det finns en signifikant korrelation mellan de GRACE-baserade GWS-avvikelsena och de extraherade olje- och vattenvolymerna. Trenden med Δ GWS-förändringar på grund av uttagen av vatten och olja varierar mellan $-18,5 \pm 6,3$ och $-6,2 \pm 1,3$ mm/år med månadsuppgifterna från Center for Space Research GRACE-lösningar och den bästa testade hydrologiska modellen i denna studie. Dessutom visar

vår analys av data från Sentinel-1 Synthetic Aperture Radar (SAR) vid användning av metoden Persistent Scatterer Interferometry (PSI) att markytan i området sjunker med en hastighet av mellan $-24,5 \pm 0,85$ och $-6 \pm 0,88$ mm/år.

I den fjärde artikeln beräknas en kombinerad Moho-modell med seismik- och tyngdkrafts-data. Syftet är att undersöka sambandet mellan litosfärens isostatiska tillstånd och seismisk aktivitet i Östafrika, Egypten, Kongo och Saudiarabien. Resultaten visar att isostatisk balans och kompenstationstillstånd är nära korrelerade med seismicitetens mönster i regionen. Artikel presenterar en metod för att bestämma jordskorpans tjocklek och densitetskontrasten mellan skorpa och mantel. Vi finner en låg densitetskontrast om cirka 200 kg/m^3 och en tunn skorpa om cirka 30 km i området Afar i Östafrika, där tre kontinentalplattor glider isär ("triple junction"), som bekräftar tillståndet för överkompensation i riftdals-områdena. Dessutom är densitetskontrasten kraftigt korrelerad med jordbävningsaktiviteten, spänningar i manteln samt och vulkanfördelningen i Östafrika.

Den femte och sista uppsatsen undersöker markytans deformation över Gävle stad i Sverige med hjälp av Sentinel-1 data och PSI teknik, och analyserar även historiska avväggningsdata. PSI-tekniken används för att kartlägga platsen för riskzoner och pågående sättningar. Vår PSI-analys visar att Gävle centrum är relativt stabilt med mindre deformationer som sträcker sig mellan $-2,0$ mm/år och $+2,0$ mm/år i vertikala och öst-väst riktningar. Däremot sjunker markytan nordost om staden med en årlig hastighet om cirka -6 mm/år. Jämförelser visar en nära överensstämmelse mellan markytans sättning erhållen med finavvägning och PSI. De regionala geologiska uppgifterna jämfördes med PSI-resultaten, och resultatet visar att områdena där marken sjunker mestadels är belägna i zoner där massorna under markytan är markerade med konstgjorda fyllmaterial.

To the soul of my mother

“Neima Nureldin”

Acknowledgment

First and foremost, I would like to express my sincerest gratitude to my main supervisor Professor Mohammad Bagherbandi, for his extreme support and guidance, from the first day I reached Sweden, and during the course of this study. His insightful guidance, valuable discussions helped me in all the time of research and writing of this thesis. Without his knowledge and encouragement, the thesis would never have reached its completion.

I am also deeply grateful to my co-supervisors Docent Famarz Nilfouroushan and Professor Lars Sjöberg for their guidance, valuable discussions and thorough comments during my studies.

My deepest gratitude goes to Dr. Jonas Boustedt, head of the department of computer and geospatial sciences, and Docent Gunilla Mårtensson, head of the faculty of Engineering and Sustainable Development, at the University of Gävle for their support and providing financial assistance and facilitate the present research work.

I would like also to thank Docent Milan Horemuz, head of the division of Geodesy and Satellite Positioning for his support, reading, and editing the thesis draft. Special thanks to Professor Anna Jensen, the former head of the division of Geodesy and Satellite Positioning, for her support and kindly cooperation during her leading of the department.

Special thanks to my friend and colleague Hadi Amin at the University of Gävle for the valuable discussions and support.

Also, I would like to thank J. Gust Richert stiftelse foundation for their financial support (Gävle project), GNPOC and Gävle municipality for sharing us their valuable data.

Finally, my deepest gratitude goes to my family for their understanding, unconditional love and support.

Nureldin Gido
Stockholm, 2020

Contents

Abstract.....	i
Acknowledgment	vi
List of Papers.....	ix
List of Tables	x
List of Figures.....	xi
List of Acronyms	xiii
Chapter 1: Introduction	1
1.1 Motivations.....	1
1.2 Aim and objectives	2
1.3 Thesis structure.....	4
1.4 Contributions	4
1.5 Contributions for national and international meetings and conferences	5
Chapter 2: Mass Redistribution in the Earth system	7
2.1 Studying Earth’s Gravity field using satellite data.....	7
2.1.1 GRACE mission	10
2.1.2 GRACE data processing	11
2.1.2.1 Gaussian filter	13
2.1.2.2 Non-isotropic filter	14
2.1.2.3 Degree one, degree two and ocean tide corrections	16
2.1.2.4 Glacial Isostatic Adjustment (GIA) correction	17
2.1.2.5 GRACE data gap problem.....	19
2.2 Mass redistribution (GRACE applications)	19
2.2.1 Total Water Storage (TWS) derived from GRACE	20
2.2.2 Ground Water Storage (GWS) changes.....	22
2.3 Global hydrological models.....	23
2.3.1 Global Land Data Assimilation System (GLDAS).....	24
2.3.2 WaterGAP model	25
2.4 Case studies.....	25
2.4.1 Paper II.....	25
2.4.2 Paper III.....	27

Chapter 3: Isostatic equilibrium and disturbances	31
3.1 Introduction.....	31
3.2 Isostatic and seismic crust models (the Moho).....	32
3.3 Veining Meinesz-Moritz model.....	35
3.3.1 Gravimetric forward modelling	36
3.4 Moho density contrast determination	41
3.5 Moho parameters determination: A combined model to estimate Moho depth and density contrast.....	41
3.6 Sub-crustal stress determination	43
3.6.1 Static horizontal sub-crustal stress using potential components.....	44
3.6.2 Static horizontal sub-crustal stress using gravimetric-isostatic crustal method: an alternative method	45
3.6.3 Temporal variation in sub-crustal horizontal stress using satellite gravimetry data.....	46
3.7 Numerical results	47
3.7.1 Paper IV: A case study in Africa.....	47
3.7.2 Paper I: A case study in Fennoscandia	53
Chapter 4: Earth’s surface deformation measurement using InSAR.....	57
4.1 Introduction.....	57
4.2 Synthetic Aperture Radar (SAR)	58
4.3 SAR Interferometry (InSAR).....	60
4.4 Differential SAR Interferometry (DInSAR).....	61
4.5 Persistent Scatterer Interferometry (PSI) technique.....	63
4.5.1 Case studies	65
Chapter 5: Conclusions and outlook.....	73
5.1 Future studies.....	76
Author’s contributions	77
References	78
Published papers (I-V)	89

List of Papers

Paper I:

Gido, N.A.A., Bagherbandi, M., Sjöberg, L.E. (2019) A gravimetric method to determine horizontal stress field due to flow in the mantle in Fennoscandia. *Geoscience Journal* (2019) 23, 377–389 doi:10.1007/s12303-018-0046-8.

Paper II:

Gido, N.A.A., Bagherbandi, M., Sjöberg, L.E., Tenzer, R. (2019) Studying permafrost by integration of satellite and in situ data in the northern high-latitude. *Acta Geophysica*. (2019) 67: 721. <https://doi.org/10.1007/s11600-019-00276-4>.

Paper III:

Gido, N.A.A., Amin, H., Bagherbandi, M., Nilfouroushan. F. (2020) Satellite monitoring of mass changes and ground subsidence in Sudan's oil fields using GRACE and Sentinel-1 data. *Remote Sensing*. 2020, 12, 1792.

Paper IV:

Bagherbandi, M., Gido, N.A.A. (*In review – Journal of Geodynamics*) A study on the relationship between isostatic equilibrium and seismicity: A case study in Africa.

Paper V:

Gido, N.A.A., Bagherbandi, M., Nilfouroushan. F. (*Accepted – Remote sensing*) Localized subsidence zones in Gävle City detected by Sentinel-1 PSI and Leveling data.

List of Tables

Table 2.1. Elastic k_n Love numbers computed by <i>Bevis et al. (2016)</i>	12
Table 2.2. Different non-isotropic filters based on damping parameter α	15
Table 2.3. GRACE and GRACE-FO on calendar. (Hatch patterns and GFO donates on GRACE data gaps and GRACE-FO, respectively).....	19
Table 2.4. Secular trends of permafrost equivalent water height (EWHP), average surface temperature, and CO ₂ at selected stations.....	27
Table 3.1. Different isostatic and seismic crustal models.....	33
Table 3.2. Free-air gravity disturbances, Bouguer gravity disturbances, additive corrections, compensation attraction, and isostatic gravity disturbances. Unit: mGal.....	48
Table 3.3. Horizontal stress due to mantle convection. Unit: MPa.....	54
Table 4.1. Specifications of Sentinel-1 satellite missions.	59
Table 4.2. Details of the Sentinel-1 A and B datasets used for the PSI time series analysis and their properties in the oil fields in Sudan.....	66
Table 4.3. Details of the Sentinel-1 A and B datasets used for the PSI time series analysis and their properties in Gävle city.	69
Table 4.4. Comparison between the computed precise leveling rates (Pre. Lev) using four different levelling records relative to four different BMs, and the relative vertical rate of the generated combined PS points in the four validation buildings using the ascending and descending combination of the 41 and 50 SAR images respectively, collected between 2015 to 2020 (see Figure 1 in Paper V).	70

List of Figures

Figure 1.1. A schematic diagram showing permafrost thawing, mantle convection, GIA process, oil/water depletion, sub-crustal stress cause, Moho boundary, and ground surface subsidence, which have been studied using different types of geodetic satellite data (e.g. the GRACE and sentinel-1), and in-situ data which is not shown here (the figure not to scale). ... 3

Figure 2.1. Illustrates general concepts of a) high-low satellite-to satellite tracking (SST-hl), b) high-low/low-low satellite-to-satellite tracking (SST-hl/SST-ll) and c) high-low satellite-to-satellite tracking/satellite gravity gradient mode (SST-hl/SGG)..... 9

Figure 2.2. TWS based on applying different decorrelation and spatial smoothing filters to a single month of CSR GRACE RL06 solutions, i.e. August 2016. Unit: cm 16

Figure 2.3. Land uplift rate using ICE-6G (VM5a) model (*Peltier et al. 2015*). Unit: mm/year. 18

Figure 2.4. a) GLDAS surface water storage changes (including soil moisture, snow, and runoff water changes) using NOAHv1 model between 2002 and 2016, and b) Water storage changes in soil, snow, and surface water bodies from WaterGap model estimates for the same period. No smoothing or truncation has been applied to the data. Unit: mm/year. 24

Figure 2.5. Secular rate of (a) the estimated total water storage anomaly (ΔTWS) and (b) the estimated groundwater storage anomaly (ΔGWS), using Gravity Recovery and Climate Experiment (GRACE) (Centre for Space Research (CSR) centre and DDK1 filter) and GLDAS (CLSM model) data, respectively, over the period of Jan 2003–Sep 2012. Unit: cm/year. 29

Figure 3.1. Local vs. regional topographic mass compensation using a) Airy, b) Pratt, and c) VMM model (figure modified after: *Sjöberg and Bagherbandi 2017*)..... 34

Figure 3.2. a) Earth2014 topography, bathymetry, and b) Earth2014 ice-sheet thickness models (*Hirt and Rexer 2015*) with spatial resolution of 1×1 arc-degree. Unit: meter. 38

Figure 3.3. a) Crustal thickness, and b) Sediment thickness using CRUST1.0 model (*Laske et al. 2013*) with spatial resolution of 1×1 arc-degree. Unit: km. 39

Figure 3.4. Gravity disturbance δg^f (using XGM2016 model) with spatial resolution of 1×1 arc-degree. Unit: mGal..... 40

Figure 3.5. Topography (δg^t), bathymetry (δg^b), ice (δg^i) (using Earth2014 model), and sediment (δg^s), using CRUST1.0 gravity corrections with spatial resolution of 1×1 arc-degree. Unit: mGal. 40

Figure 3.6. Isostatic gravity disturbances using the VMM model. Unit: mGal. 50

Figure 3.7. a) Crustal thickness using combination of the VMM, CRUST1 and Baranov models (Unit: km), and b) Crust-mantle density contrast determined using combined model (red stars show volcanic areas, white color circles denote on the location of earthquakes larger than 4 Richter magnitude scale between 2008-2018 (no scaled), and solid magenta line shows the main plate boundaries). Unit: kg/m^3 51

Figure 3.8. Gravimetric sub-crustal stress obtained from modified Runcorn method (*Runcorn 1967*), and solid magenta line shows the main plate boundaries. The arrows in the figure show velocity/gradients vectors of the sub-crustal stress and dark red arrows illustrate larger gradients. 52

Figure 3.9. a) Absolute sub-crustal horizontal stress due to mantle convection (tectonics), Unit: MPa. b) Temporal variation of sub-crustal horizontal stress using CSR GRACE data for the period of 2003 to 2016 (secular rate of the horizontal stress are shown as color circles (Unit: kPa/year) and direction of the horizontal stress changes with black arrows, Unit: kPa/year). 55

Figure 4.1. Acquisition geometry of SAR system. H and V are the flying height and velocity. The side looking system illuminates a certain area on the ground (blue part). 59

Figure 4.2. Principle of DInSAR deformation measurement. M denotes for image acquired at time (t_1) for ground target P (before deformation), S denotes for image acquired at time (t_2) for target P' (target P after deformation). d is the change in the measured range due to surface deformation. 63

Figure 4.3. a) General map showing digital elevation of the region (Unit: m), the Basins and the study area in oil fields concessions, and b) the location of the nine oil fields in the study area and their total extraction between Jan 2003 and Sep 2012 in m^3 . The footprint of the three descending Sentinel-1 data sets over the nine oil fields are shown by rectangles, covering the period between November 2015 and April 2019. 66

Figure 4.4. Cumulative displacement in (mm) of the selected PSI points relative to reference point (H-124) in Heglig and Bamboo oil fields. 68

Figure 4.5. LOS displacement rates of all generated descending PS points in Gävle city relative to the reference point (pink color). Area-1 shows the maximum displacement zone. A1, A2, A3, A4, and A5 refer to the five different small areas. The observation period is from June 2015 to May 2020. 71

Figure 4.6. The vertical displacement rate of the combined ascending and descending PS points overlaid on the quaternary deposits map of the city of Gävle. Negative values denote for subsidence, while the positive denotes for uplift. Base map: Quaternary deposit © Geological Survey of Sweden (SGU). Coordinate system: SWEREF 99. Unit: mm/year 72

List of Acronyms

APS	Atmospheric Phase Screen
CHAMP	Challenging Mini-Satellite Payload for Geophysical Research and Application
CLSM	Catchment Land Surface Model
CSR	Centre for Space Research
DEM	Digital Elevation Model
DInSAR	Differential Interferometry Synthetic Aperture Radar
DLR	German Aerospace Centre
ESA	European Space Agency
EWH	Equivalent Water Height
GFZ	GeoForschungsZentrum
GIA	Glacial Isostatic Adjustment
GLDAS	Global Land Data Assimilation System
GLONASS	GLOBAL NAVIGATION Satellite System
GOCE	Gravity Field and Steady-state Ocean Circulation Explorer
GPS	Global Positioning System
GRACE	Gravity Recovery and Climate Experiment
GRACE-FO	Gravity Recovery and Climate Experiment Follow-On
GWS	Ground Water Storage
InSAR	Interferometric Synthetic Aperture Radar
JPL	Jet Propulsion Laboratory
LAGEOS	LASER GEODYNAMIC Satellite
LEO	Low-Earth Orbit
LOS	Line OF Sight
LSM	Land Surface Model
Moho	Mohorovičić discontinuity
NASA	National Aeronautics and Space Administration
NKG	Nordic Geodetic Commission
PS	Persistent Scatterer
PSC	Persistent Scatterer Candidates
PSI	Persistent Scatterer Interferometry
SAR	Synthetic Aperture Radar
SGG	Satellite Gravity Gradiometry
SHC	Spherical Harmonic Coefficients
SLC	Single Look Complex
SLR	Satellite Laser Ranging

SRTM	Shuttle Radar Topography Mission
SST	Satellite-to-Satellite Tracking
SST-hl	high-low Satellite-to-Satellite Tracking
SST-ll	low-low Satellite-to-Satellite Tracking
SWM	Surface Water Mass
SWS	Surface Water Storage
TWS	Total Water Storage
VMM	Vening Meinesz-Moritz
W3RA	World-Wide Water Resources Assessment
WGHM	WaterGAP Global Hydrology Model
Δ	Anomaly

Chapter 1

Introduction

1.1 Motivations

Natural and anthropogenic processes such as permafrost thawing, earthquakes, glacial isostatic adjustment (GIA), mantle convection and ground surface subsidence that related to the sub-surface geology and/or groundwater/oil depletion have great impact on human life and sustainability goals. All these processes can be result of or cause the so-called lithospheric motion, which generally herein take place at the Earth's surface and/or within its interior including lower lithospheric part (see Figure 1.1). Such processes are largely affected by the Earth's mass transport and redistribution, which can be quantified in terms of gravity variation and crustal deformation using e.g. the Gravity Recovery and Climate Experiment (GRACE) and Synthetic Aperture Radar (SAR) satellite data, respectively. The modelling of the Earth's mass distributions at different layers, as well as the temporal changes/transport of such masses, are most important in studying the geodynamics of relevance. Such studies will improve our capability to understand, monitor, and predict geo-hazard and environmental assessment. We aim at using global data products such as satellite observations, in addition to some in situ measurements. The outcome might contribute to mapping some uncharted areas of different scales based mainly on geodetic techniques.

In this study, we intend to apply and develop geodetic methods to study: 1) permafrost thawing and its relation to the global warming, 2) sub-crustal stress field modelling due to the mass change in the Earth's deep layer, 3) relation between isostatic equilibrium and seismicity, and finally, 4) ground surface subsidence monitoring due to mass depletion in the near-surface layer of the Earth, and the type of sub-surface geology of the study area. For example, studying permafrost thawing, which is attributed to the global warming, and its associated organic material changes are of great importance, not only from a perspective of localized geo-hazard such as erosion, damage to building and infrastructure but also with respect to its possible global impact due to greenhouse emissions. However, its estimation requires combined

information from various sources, particularly by using the gravity field change, surface temperature, and the Glacial Isostatic Adjustment (GIA).

The outcomes of this study might allow investigating a long-term development of the Earth's shape interior, gravity field, climate change, and assessment of its impact. Moreover, extraction of large volume of water and oil can decrease the reservoir pressure, form compaction, and consequently, land subsidence may occur, which can be analyzed using remote sensing techniques (i.e. GRACE and SAR data). Land subsidence can also be attributed to sub-surface geology in urban areas that are studied here. Furthermore, tectonic processes, earthquake and seismic activities might largely be attributed to the Earth's crust parameters (i.e. density, depth, etc.) and to the mass changes and flow in the Earth's mantle, which can produce major stress in the lithosphere. Gravimetric methods are utilized for such investigation and modelling in this thesis.

1.2 Aim and objectives

The general aim of this thesis is to use integrated geodetic satellite and non-geodetic observations to understand better the environmental and deep Earth's processes (see Figure 1.1). Particular research objectives of this thesis include:

- Studying the gravity variation in terms of Groundwater storage anomalies (ΔGWS) change, associated to permafrost thawing and groundwater/ oil depletion using best examined filtered GRACE data, and hydrological models.
- Using of gravimetric approach to model sub-crustal horizontal stress and its temporal changes caused by geodynamical processes such as mantle convection.
- Investigating the relationship between the isostatic state of the lithosphere and seismic activities, using a combined Moho model calculated by seismic and gravity data.
- Measuring and analysing the ground surface deformation associated with the sub-surface geology type and water/oil depletion using InSAR technique.

Figure 1.1. Shows a summary of the main research topics and the exploited satellite missions.

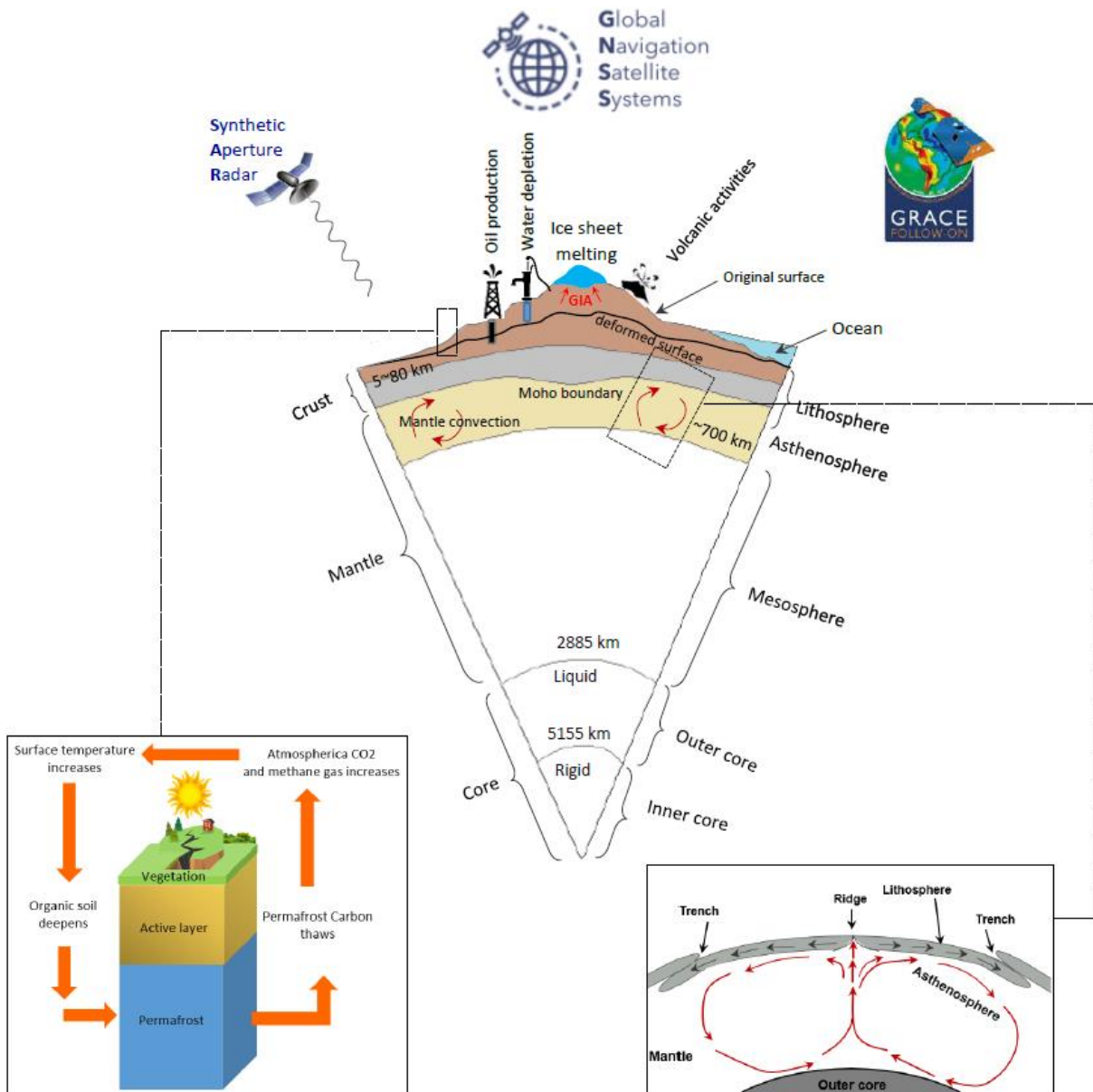


Figure 1.1. A schematic diagram showing permafrost thawing, mantle convection, GIA process, oil/water depletion, sub-crustal stress cause, Moho boundary, and ground surface subsidence, which have been studied using different types of geodetic satellite data (e.g. the GRACE and sentinel-1), and in-situ data which is not shown here (the figure not to scale).

1.3 Thesis structure

The thesis is written as a comprehensive summary of a compilation of five papers (four published and one under review). There are two major parts, where the first one describes all methodologies developed in the research and the achieved results by implementing these methods. In the second part, all research papers that have been produced during the PhD studies, both published and submitted, are included.

The structure of the first part is as follows: Chapter 1 provides a short introduction to the thesis, along with the research aim and objectives. A review of temporal gravity field variation and its applications is given in Chapter 2. Isostatic equilibrium and disturbances are discussed in Chapter 3. Earth's surface subsidence monitoring using PSI technique is described in Chapter 4. Finally, conclusions and suggestions for future work are presented in Chapter 5.

1.4 Contributions

Through the five papers, the contributions of this thesis can be summarized as follow:

- In the first paper, an absolute stress induced by mantle convection in Fennoscandian region was studied using gravimetric approach. Furthermore, its temporal changes were investigated using GRACE monthly data. The numerical results show that there is a relation between secular rate of sub-lithosphere horizontal stress and earthquake activities in Fennoscandia. The outcomes of this study explain the reasons of the obtained inhomogeneous stress in the study area.
- In the second paper, permafrost thawing and its associated gravity change, in terms of groundwater storage anomaly (ΔGWS) change were studied using CSR GRACE monthly solutions and other satellite and ground-based observations in the northern high-latitude region, covering period from August 2002 to May 2016. The GRACE data were filtered and corrected for GIA, ice melting in Greenland, and hydrological signal in order to estimate the equivalent water height (EWH) changes due to the permafrost thawing. Glaciers melting correction data in Greenland was prepared by Shfaqat A. Khan from DTU Space, Technical University of Denmark. Using the outcomes of this study, a possible correlation between the trends of greenhouse gases (CO_2), temperature, and the EWH in some selected regions can be investigated.
- In the third paper, mass variations were estimated in terms of large-scale groundwater storage (GWS) changes and surface deformation, using CSR

GRACE monthly solutions and Sentinel-1 SAR data, over major oil fields in Sudan. The GRACE data were filtered and corrected using different isotropic and non-isotropic filters. Different hydrological models were used and studied. A correlation were performed between the estimated GRACE-based GWS changes and the extracted oil using the best tested hydrological models in the study. In addition, land subsidence associated with oil extraction is investigated using SAR data.

- In the fourth paper, the relationship between the isostatic state of the lithosphere and seismic activities was investigated using a combined Moho model of seismic and gravity data in a region that includes East Africa, Egypt, Congo, and Saudi Arabia.
- In the fifth paper, ground surface deformation associated with the sub-surface geology of the study area was investigated using Sentinel-1 SAR data as well as analyzing the historical leveling data in Gävle city, Sweden. The PSI technique was used to map the location of risk zones and their ongoing subsidence rate.

1.5 Contributions for national and international meetings and conferences

Gido, N.A.A., Bagherbandi, M. & Sjöberg, L.E. A gravimetric method to determine horizontal stress field due to flow in the mantle in Fennoscandia. Nordic Geodetic Commission (NKG) Summer School 2016, 29 August-1 September, Båstad, Sweden.

Gido, N.A.A., Bagherbandi, M. Sjöberg, L.E. A gravimetric method to determine horizontal stress field due to flow in the mantle in Fennoscandia. Kartdagar 2017, Örebro, Sweden.

Nilfouroushan, F., Bagherbandi, M., Gido, N.A.A. Ground Subsidence and Groundwater Depletion In Iran: Integrated approach Using InSAR and Satellite Gravimetry, Fringe (European Space Agency) 2017, 5-9 June, Helsinki, Finland.

Bagherbandi M., Amin, H., Gido, N.A.A., Sjöberg, L.E. A novel approach to study ice mass change using satellite data in Greenland and Antarctica. Joint Scientific Assembly of the International Association of Geodesy (IAG) and International Association of Seismology and Physics of the Earth's Interior (IASPEI) 2017, 30 July-4 August, Kobe, Japan.

Gido, N.A.A., Bagherbandi, M., Sjöberg, L.E., Tenzer, R. Studying permafrost by integration of satellite and in situ data in Arctic region. Nordic Geodetic Commission (NKG) General Assembly 2018, 3-6 September, Helsinki, Finland.

Gido, N.A.A., Bagherbandi, M., Sjöberg, L.E., Tenzer, R. Studying permafrost by integration of satellite and in situ data in Arctic region. IX Hotine-Marussi Symposium 2018, 18-22 June, Faculty of Civil and Industrial Engineering of the University of Rome "La Sapienza", Italy.

Gido, N.A.A., Amin, H., Bagherbandi, M., Nilfouroushan, F. Satellite monitoring of mass changes and ground subsidence in Sudan's oil fields using GRACE and Sentinel-1 data. EGU General Assembly 2020, 3-5 May, Vienna, Austria.

Chapter 2

Mass Redistribution in the Earth system

2.1 Studying Earth's Gravity field using satellite data

The Earth's gravity field change is a primary physical parameter that reflects mass changes in the Earth's system, including the solid Earth and its geophysical fluid envelope (e.g. atmosphere and hydrosphere). The static gravity field is largely controlled by mass distribution in the solid Earth (i.e. the crust, mantle and core). The internal density structure of the Earth, land topography and ocean bathymetry are more or less reflected by the static gravity anomalies. However, the short-term scale (within, say, 100 years) time-variable gravity field is dominated by air and water mass redistribution within the Earth's climate system (*Wahr et al. 1998; Cazenave and Chen 2010*), in terms of total water storage (TWS) changes, floods and droughts, permafrost thawing, and groundwater storage (GWS) change. At long-term time scales e.g. 100's to 1000's of years, the solid Earth geophysical effects, such as Glacial Isostatic Adjustment (GIA), tide effects, plate and intraplate tectonics, seismicity, man-made mass changes, etc., will also lead to time-variable gravity field. Accurate determination of the gravity field and its temporal changes are of great importance to study and monitor mass redistribution in the Earth's system, including various physical and geodynamic processes such as GIA (*Simons and Hager 1997*), hydrologic cycle (*Rodell et al. 2009*), sea-level change (*Velicogna and Wahr 2006*), the mass balance of ice sheets and glaciers (*Velicogna and Wahr 2006*) and rotation of the earth and mass displacement (*Jin et al. 2010*), in addition to its role in geodesy by studying the size and shape of the Earth.

Traditionally, three measuring techniques can be used for gravity field determination. The first one is terrestrial gravimetry, which is a cost-intensive method in addition to its low temporal-spatial resolution. The second one is the satellite altimetry, which can provide both static and temporal variation of the gravity field and geoid over the ocean. Thirdly, a global to regional scale of gravity field can be estimated by tracking artificial satellites in Earth's orbit using laser ranging (SLR). Because the orbital motion of the satellite is largely governed by gravitational forces, the orbit solution based on

precise satellite tracking measurement can be utilized to invert for gravity field. Due to the high-altitude of such targeted satellite, e.g. LAGEOS (LAsER GEODynamic Satellite) which is at about 6000 km, the provided gravity information is only at long wavelengths (*Wahr et al. 1998*). The SLR observations to LAGEOS and other satellites, have also been used to detect temporal variation in the Earth's gravity field that subject to the mass redistribution due to dynamic process (e.g. seasonal, decadal and secular change) within the Earth and on and above its surface (*cf. Yoder et al. 1983; Dong et al. 1996*).

The SLR technique has an important contribution to the Earth's climate studies through the accurate measuring of low-degree gravitational change, which provides observational constraint on global scale mass redistribution in the climate system (*Cheng and Tapley 1999; Cox and Chao 2002*). The long record of degree-2 zonal term c_{20} using the SLR system is believed to be the best determined term, and it helps for better understanding of climate change (*Cox and Chao 2002; Dickey et al. 2002*).

The precision of the Earth's gravity field model and temporal-spatial resolution were greatly increased with the recent development of the low-earth orbit (LEO) satellite gravimetry. Unlike the traditional gravity measurement methods (e.g. high-altitude orbital perturbation analysis), the most advanced Satellite-to-Satellite Tracking (SST) and Satellite Gravity Gradiometry (SGG) techniques are used to estimate the global-high precision gravity field and its time variation.

Since 2000, four dedicated gravity recovery satellite missions have been launched, i.e., Challenging Mini-Satellite Payload for Geophysical Research and Application (CHAMP), Gravity Field and Steady-state Ocean Circulation Explorer (GOCE), Gravity Recovery and Climate Experiment (GRACE), and Gravity Recovery and Climate Experiment Follow-On (GRACE-FO). The SST technique includes the so-called high-low Satellite-to-Satellite Tracking (SST-hl) (*Baker ML R 1960*) e.g. CHAMP satellite mission, and the low-low Satellite-to-Satellite Tracking (SST-ll) (*Wolff 1969*) e.g. GRACE and GRACE-FO satellite missions, which can determine the variation rate of the distance between the satellites very precisely. CHAMP is a German geophysical mini satellite mission of GFZ (GeoForschungsZentrum), in cooperation with DLR (German Aerospace Centre), was launched and decommissioned between July 15, 2000 and September 19, 2010, using the SST-hl mode and GPS satellites as high orbital satellites (*Reigber et al. 1999; see Figure 2.1a*). The primary objectives of CHAMP mission were to obtain precise global long-to medium wavelength feature of the static and time-variable Earth gravity field from orbit perturbation analysis, global Earth magnetic field recovery and atmospheric and ionospheric investigation from GPS radio occultation with applications in weather forecasting, navigation, space weather,

and global climate change. CHAMP's orbit was determined using the on-board GPS receivers and the SLR ground-based. The non-gravitational accelerations were measured using the three-axes STAR accelerometer.

GOCE is a European Space Agency (ESA) mission, with a primary objective to provide global and regional models of the Earth's gravity field with an accuracy of 1 mGal, and the geoid with an accuracy of 1-2 cm, in addition to achieve high spatial resolution better than 100 km. It was launched and decommissioned between 17 March 2009 and 21 October 2013 with a mean altitude of about 263 km, and high-low satellite-to-satellite tracking and satellite gravity Gradiometry mode (*ESA report 1999*; see Figure 2.1c). The mission equipped with three pairs of ultra-sensitive accelerometer and on-board GPS/GLONAS receivers for high accuracy positioning. Therefore, CHAMP and GOCE missions are capable to recover the global Earth gravity field with higher resolution and accuracy, in addition to GRACE and GRACE-FO. Figure 2.1 shows the general concept of the SST-hl, SST-ll, and SST-hl/SGG techniques.

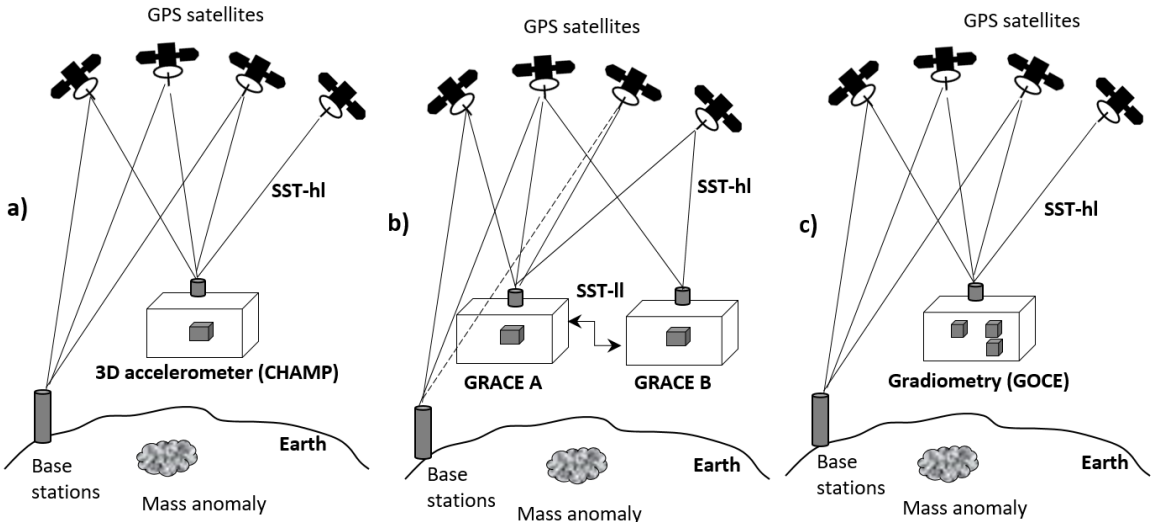


Figure 2.1. Illustrates general concepts of a) high-low satellite-to satellite tracking (SST-hl), b) high-low/low-low satellite-to-satellite tracking (SST-hl/SST-ll) and c) high-low satellite-to-satellite tracking/satellite gravity gradient mode (SST-hl/SGG).

Since its launch in 2002, GRACE (Figure 2.1b) offers a unique alternative to the classical remote sensing technique for measuring the temporal variation of the Earth's gravity field with unprecedented accuracy, and also a new tool for measuring mass redistribution in the climate system i.e. total water storage and groundwater (*Tapley et al. 2004a*).

2.1.1 GRACE mission

The Gravity Recovery and Climate Experiment (GRACE) was a joint US-German mission (NASA/ German Aerospace Centre), launched in 17 March 2002 and decommissioned in 27 October 2017, to map the Earth's gravity field. The mission consisted of two identical twin satellites GRACE-A and GRACE-B, following each other on the same orbital path, with a mean distance of approximately 220 km in a satellite-to-satellite tracking (SST) configuration in the low-low mode (*Wolff 1969*), and orbiting the Earth at an altitude of about 450 km (Figure 2.1b). The primary objectives of the mission was to provide with unprecedented accuracy, global and high-resolution of the Earth's gravity field models, of both static and time variable components (*Tapley et al. 2004b*).

By continuously monitoring the relative motion between the two satellites (i.e. the range and the range rate) using K-band microwave ranging system (*Tapley et al. 2004b*) the gravity acceleration which varies proportionally to the distance and sensed by the satellites (*Schmidt et al. 2008*) can be estimated in the form of corrections to a well-defined background gravity model used in the data processing producer (*Bettadpur 2012*). The K-band system provides accuracy better than 1 micrometre using carrier phase measurement in the K (26 GHz) and Ka (32 GHz) frequencies for measuring the distance between the two satellites. On-board GPS receivers to determine the position of each sensor in a geocentric reference frame. On-board accelerometer used to detect the non-gravitational effects. By removing the non-gravitational effects from the satellite-to-satellite range, the geopotential estimation with an unprecedented accuracy can be achieved using the corrected variation of the measured distance.

Analyses of the GRACE data allow determination of the temporal changes of the Earth's gravity field to high accuracy. Level 1b GRACE products consist of processed position and velocities that were measured by the on-board GPS, the K-band system, and the accelerometer. These measurements are used to compute level 2 products or the monthly gravity field modes in terms of geoid height or Equivalent Water Height (EWH) (*Wahr et al. 1998*). Level 2 GRACE products are estimated using a dynamic approach that is based on the Newtonian formulation of the satellite's equation of motion in an inertial frame, with the Earth's centre as origin, combined with a dedicated modeling of gravitational and non-conservative forces acting on the satellites (*Schmidt et al. 2008*).

The GRACE monthly products are generally delivered in the form of fully normalized spherical harmonic coefficients (SHCs) up to certain maximum degree and order (typically, up to 60, and also 96 or 120 are available) (*Chen 2019*). During GRACE data processing the known gravitational effects (changes in atmosphere and oceans masses, and tidal effects) are removed using atmospheric and ocean circulation models through the dealiasing process (*Dahle et al. 2013*), as well as the non-gravitational

effects that were measured by the on-board accelerometers. Monthly GRACE global gravity solutions are provided by three data centres including Centre for Space Research (CSR) at the University of Texas, Austin, United States, Deutsches GeoForschungsZentrum, German Research Centre for Geosciences (GFZ) in Potsdam, Germany, and the NASA Jet Propulsion Laboratory (JPL) in the United States. The GRACE solutions are distributed by the NASA PODAAC (<http://podaac.jpl.nasa.gov/grace/>) and GFZ Information System and Data Centre (<http://isdc.gfz-potsdam.de/grace-isdc/>).

Using of the GRACE-based solutions the time variation of the Earth's gravity field can be determined, which is very useful for many areas of scientific research such as hydrology, solid Earth science, and glaciology, and it leads to better understanding of time-variable process e.g. soil moisture changes (*Swenson et al. 2008*), continents storage changes of water and snow (*Swenson and Wahr 2002*), and in permafrost thawing studies (*Gido et al. 2019*). However, the GRACE solutions are prone to some limitations, e.g. noises due to the sensor errors, the background models used in the analysis, the mission geometry, and the satellite orbit and its effect on data collection. Therefore, proper filtering and processing methods have to be applied to ensure proper GRACE data. The general GRACE data processing steps can be summarized as below:

Corrected GSM =

$$\text{GSM} + c_{20} \text{ Correction} + c_{10}, c_{11} \text{ and } s_{11} \text{ Corrections} + \text{GIA Correction} + \text{GAD}$$

where GSM denotes the GRACE monthly SHCs, c_{20}, c_{10}, c_{11} and s_{11} are GRACE-derived Stokes coefficients of degree 2 and degree 1 (will be defined and discussed in section 2.1.2.3), GAD denotes the modeled atmospheric and oceanic contributions to the Stokes coefficients which have had the atmospheric signals over land set to zero. The coefficients in the GAD file therefore represent the ocean bottom pressure variations.

2.1.2 GRACE data processing

According to *Chao (2005)*, the inversion of 3D mass variation from time-variable gravity solutions require some constraints from other independent observations or assumptions. By assuming that mass variations mostly occur on the near Earth surface in the Earth geophysical fluids envelope (atmosphere and hydrosphere) at decadal or shorter time scale, the GRACE monthly SHCs i.e. c_{nm} and s_{nm} can be converted into a surface mass change in terms of the EWH as in *Wahr et al. (1998)*:

$$\Delta\sigma(\theta, \lambda) = \frac{M_E}{4\pi R^2} \sum_{n=0}^{n_{\max}} \sum_{m=0}^n \frac{2n+1}{1+k_n} W_n P_{nm}(\sin\theta) (\Delta c_{nm} \cos(m\lambda) + \Delta s_{nm} \sin(m\lambda)) \quad (2.1a)$$

$$\begin{aligned} \Delta c_{nm} &= c_{nm} - \bar{c}_{nm} \\ \Delta s_{nm} &= s_{nm} - \bar{s}_{nm} \end{aligned} \quad (2.1b)$$

where θ and λ are the co-latitude and longitude, respectively, R is the Earth's mean radius, P_{nm} are the fully normalized Legendre polynomial of degree n and order m , M_E is the mass of the Earth, $\Delta\sigma(\theta, \lambda)$ is the mass load change (in kg/m² or equivalent water height in mm), k_n are the load love numbers of the solid Earth that account for mass redistribution of the Earth due to changing surface load (Table 2.1). W_n is the normalized Gaussian weighting function to smooth the estimated equivalent water height. \bar{c}_{nm} and \bar{s}_{nm} are the mean value of the SHCs over time.

Table 2.1. Elastic k_n Love numbers computed by *Bevis et al. (2016)*.

Degree n	k_n
1	0.0000
2	0.0270
3	-0.3058
4	-0.1963
5	-0.1338
6	-0.1048
7	-0.0903
8	-0.0821
9	-0.0765
10	-0.0724
11	-0.0691
20	-0.0522
30	-0.0414
40	-0.0336
50	-0.0280
60	-0.0238

GRACE high degree and order (e.g. after 30 degrees and order) SHCs are dominated by longitudinal stripping noises, which originated from the existing correlation between the odd and even degree pairs of the GRACE SHCs of a certain order and it can be suppressed using the so-called decorrelation filtering (*Swenson and Wahr 2006*). Isotropic filtering such as Gaussian smoothing filter (*Wahr et al. 1998*) and non-isotropic filter (*Han et al. 2005; Kusche et al. 2009*) can be applied to the SHCs to the corresponding degree. It is worth noting that, the decorrelation filtering may affect the real signal in regions where mass changes are mostly south-north pattern.

2.1.2.1 Gaussian filter

By using spatial averaging, developed by *Jekeli (1981)*, a low-pass filter is used to reduce the noise effects in the high-order spherical harmonics using normalized Gaussian averaging function, GRACE can deliver useful results. According to *Wahr et al. (1998)*, the spatial average of the surface mass density change ($\Delta\sigma$) can be formulated as:

$$\overline{\Delta\sigma} = \int \cos\theta' d\theta' d\lambda' \Delta\sigma(\theta', \lambda') W(\theta, \lambda, \theta', \lambda') \quad (2.2)$$

where $W(\theta, \lambda, \theta', \lambda')$ is an averaging function.

By expanding Eq. (2.2) in terms of the SHCs, Δc_{nm} and Δs_{nm} , and doing some manipulations according to *Wahr et al. (1998, eq. 14)*, Eq. (2.2) can be rewritten as:

$$\begin{aligned} \overline{\Delta\sigma}(\theta, \lambda) = & \frac{R\rho_e}{12\pi} \sum_{n=0}^{n_{\max}} \sum_{m=0}^n P_{nm}(\sin\theta) \sum_{n'=0}^{n'_{\max}} \sum_{m'=0}^{n'} \frac{2n'+1}{1+k_{n'}} \\ & \left[(\Delta c_{n'm'} W_{nmc}^{n'm'c} + \Delta s_{n'm'} W_{nmc}^{n'm's}) \cos(m\lambda) + (\Delta c_{n'm'} W_{nms}^{n'm'c} + \Delta s_{n'm'} W_{nms}^{n'm's}) \sin(m\lambda) \right] \end{aligned} \quad (2.3)$$

where ρ_e is the average density of the Earth (5500 kg/m³), and

$$\begin{aligned} \begin{Bmatrix} W_{nmc}^{n'm'c} \\ W_{nms}^{n'm'c} \\ W_{nmc}^{n'm's} \\ W_{nms}^{n'm's} \end{Bmatrix} = & \int \cos\theta d\theta d\lambda \int \cos\theta' d\theta' d\lambda' \begin{Bmatrix} \cos(m'\lambda') \cos(m\lambda) \\ \cos(m'\lambda') \sin(m\lambda) \\ \sin(m'\lambda') \cos(m\lambda) \\ \sin(m'\lambda') \sin(m\lambda) \end{Bmatrix} \times \\ & W(\theta, \lambda, \theta', \lambda') P_{nm}(\sin\theta) P_{n'm'}(\sin\theta') \end{aligned} \quad (2.4)$$

For averaging over large regions, the $W_{nmc}^{n'm'c}$, $W_{nms}^{n'm'c}$, $W_{nmc}^{n'm's}$ and $W_{nms}^{n'm's}$ are small for large degrees and orders (n, m, n', m'). Thus the contribution to $\overline{\Delta\sigma}$ from the poorly known $\Delta c_{n'm'}$ and $\Delta s_{n'm'}$ at large values of (n', m') tend to be small. *Jekeli (1981)* also assumed that $W(\theta, \lambda, \theta', \lambda')$ is depend only on the angle α between the two points (θ, λ) and (θ', λ') i.e.:

$$W(\theta, \lambda, \theta', \lambda') = W(\alpha) \quad (2.5a)$$

where $\cos\alpha = \cos\theta\cos\theta' + \sin\theta\sin\theta'\cos(\lambda - \lambda')$ then Eq. (2.3) and (2.4) can be written:

$$\overline{\Delta\sigma}(\theta, \lambda) = \frac{2R\rho_e\pi}{3} \sum_{n=0}^{n_{\max}} \sum_{m=0}^n \frac{2n+1}{1+k_n} W_n P_{nm}(\sin\theta) [\Delta c_{nm} \cos(m\lambda) + \Delta s_{nm} \sin(m\lambda)] \quad (2.5b)$$

where

$$W_n = \int_0^\pi W(\alpha) P_n(\cos\alpha) \sin\alpha d\alpha \quad (2.5c)$$

and P_n are the Legendre polynomials.

Jekeli's Gaussian averaging function is given by:

$$W(\alpha) = \frac{b}{2\pi} \frac{\exp[-b(1-\cos\alpha)]}{1-e^{-2b}} \quad (2.6a)$$

$$b = \frac{\ln(2)}{1-\cos\left(\frac{r}{R}\right)} \quad (2.6b)$$

where r is the distance on the Earth's surface, where the kernel dropped to 1/2 its value at $\alpha = 0$, (which is commonly used to indicate the degree of smoothing). *Jekeli (1981)* showed that the coefficients W_n can be computed with the recursion formulas as follow (multiplied by a normalization factor 2π):

$$W_0 = 1 \quad (2.7a)$$

$$W_1 = \frac{1+e^{-2b}}{1-e^{-2b}} - \frac{1}{b} \quad (2.7b)$$

$$W_{n+1} = -\frac{2n+1}{b} W_n + W_{n-1} \quad (2.7c)$$

In this study, wherever GRACE solution is used, the Gaussian spatial smoothing function on the monthly GRACE gravity coefficients has been applied/evaluated using different radius (r). The radii should be selected precisely because of their high ($r=300$ km) and low ($r=700$ km) pass properties and sometimes they can filter out the desired signals.

2.1.2.2 Non-isotropic filter

By assuming that, the averaging function $W(\theta, \lambda, \theta', \lambda')$ depends on both spherical harmonic degree and order, $W(\theta, \lambda, \theta', \lambda')$ can be written as follows:

$$W(\theta, \lambda, \theta', \lambda') = \frac{1}{4\pi} \sum_{n=0}^{n_{\max}} \sum_{m=0}^n P_{nm}(\sin\theta) [\Delta A_{nm}^c(\theta', \lambda') \cos(m\lambda) + \Delta A_{nm}^s(\theta', \lambda') \sin(m\lambda)] \quad (2.8a)$$

where

$$\begin{aligned}\Delta A_{nm}^c(\theta', \lambda') &= W_{nm} P_{nm}(\sin \theta') \cos(m\lambda') \\ \Delta A_{nm}^s(\theta', \lambda') &= W_{nm} P_{nm}(\sin \theta') \sin(m\lambda')\end{aligned}\tag{2.8b}$$

and W_{nm} is the non-isotropic kernel that should be defined.

Kusche (2007) introduced some non-isotropic DDK filters derived by regularization of a normal equation matrix. With the normal equation matrix \mathbf{N} , and right-hand side vector \mathbf{b} , the least square adjustment to estimate the spherical harmonic coefficients (\mathbf{x}):

$$\hat{\mathbf{x}} = \mathbf{N}^{-1}\mathbf{b}\tag{2.9a}$$

Using an approximation to the GRACE error covariance (\mathbf{N}^{-1}) and GRACE a prior signal covariance (\mathbf{M}^{-1}), the regularized unknown can be estimated as:

$$\hat{\mathbf{x}}_{\alpha} = (\mathbf{N} + \alpha\mathbf{M})^{-1} \mathbf{b} = (\mathbf{N} + \alpha\mathbf{M})^{-1} \mathbf{N}\hat{\mathbf{x}} = \mathbf{W}_{\alpha} \hat{\mathbf{x}}\tag{2.9b}$$

where, the matrix \mathbf{W}_{α} is defined as the non-isotropic filter (DDK), and α controls the degree of smoothing. Table 2.2 shows different damping parameters that determine low to high pass filters.

Table 2.2. Different non-isotropic filters based on damping parameter α

	DDK1	DDK2	DDK3	DDK4	DDK5	DDK6	DDK7	DDK8
α	1×10^{14}	1×10^{13}	1×10^{12}	5×10^{11}	1×10^{11}	5×10^{10}	1×10^{10}	5×10^9

Figure 2.2 illustrates the effect of applying different decorrelation (i.e. DDK1, DDK2... and DDK7), and spatial smoothing filters (using Gaussian filter i.e. 300 and 500 km radius) to a single month (i.e. August 2016) of RL06 CSR GRACE-based TWS estimates in a global scale. The figure shows clearly the effect of low and high pass filters.

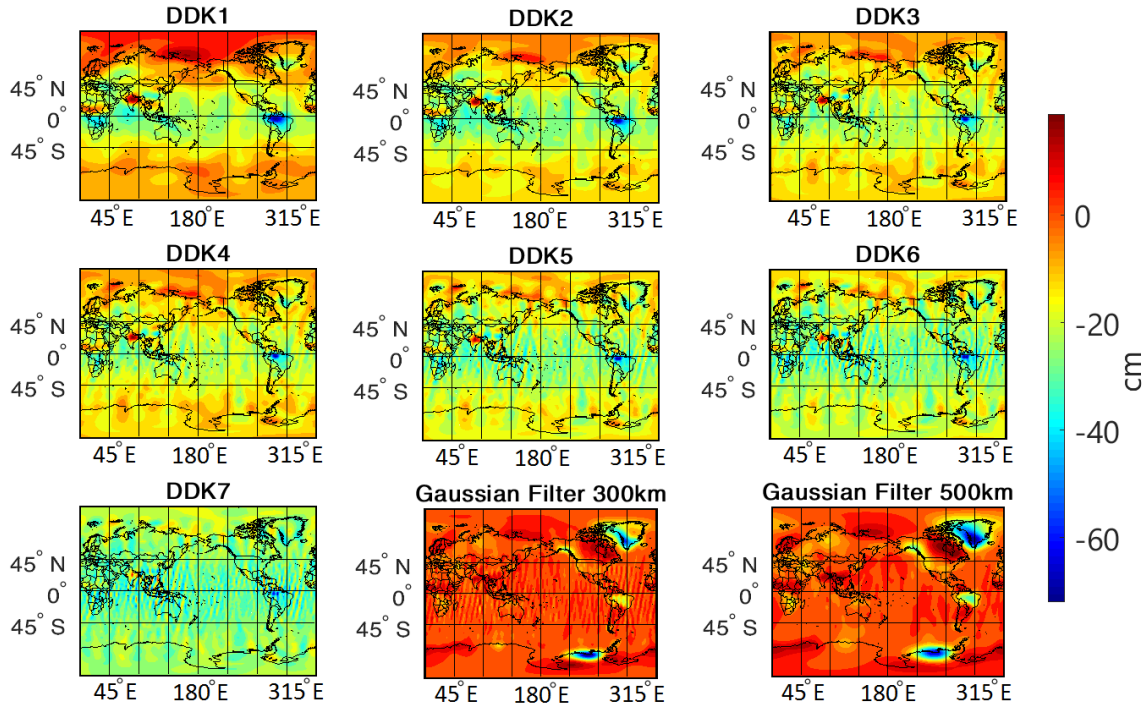


Figure 2.2. TWS based on applying different decorrelation and spatial smoothing filters to a single month of CSR GRACE RL06 solutions, i.e. August 2016. Unit: cm

2.1.2.3 Degree one, degree two and ocean tide corrections

The GRACE-derived Stokes coefficients are prone to some errors, and special corrections are needed for the degree-one coefficients (c_{10} , c_{11} , and s_{11}) and the zonal harmonic of degree 2 (c_{20}) (see more in *Swenson and Wahr 2002*; *Cheng and Ries 2017*). The Earth gravity field is defined in the Earth centre of mass (i.e. as origin) with respect to the centre of the terrestrial reference frame. Therefore, and due to the geocenter variation of the Earth centre of mass to the centre of terrestrial reference frame, the GRACE time variable gravity fields only provide SHCs of degree 2 or above, correctly. Thus, special corrections are needed for the degree-one coefficients (c_{10} , c_{11} , and s_{11}), which represent the position of the Earth's mass centre relative to an Earth-fixed reference frame (*Crétaux et al. 2002*). Because the satellite gravimetry is not sensitive to the Earth's geocenter motion, degree one coefficients, need to be added to the GRACE products by a model of the degree one variations (*Crétaux et al. 2002*; *Amin et al. 2020*). The missing degree-1 SHCs are linearly related to the (x, y, z) components of the geocenter motion, and according to *Crétaux et al. (2002)*, converting geocentric fluctuations to normalized degree one gravity coefficients can be achieved as follow:

$$c_{10} = \frac{z(t)}{\sqrt{3a_E}}, \quad c_{11} = \frac{x(t)}{\sqrt{3a_E}}, \quad s_{11} = \frac{y(t)}{\sqrt{3a_E}} \quad (2.10)$$

where $x(t)$, $y(t)$, and $z(t)$ denotes for the geocenter variations and a_E is the mean equatorial radius. Geocenter motion can be determined using different geodetic methods including SLR, DORIS, GNSS and other various combinations (*Blewitt and Clarke 2003*). More precisely, here we use the monthly estimates model provided by JPL i.e. GRACE Technical Note #13a (<https://podaac.jpl.nasa.gov/gravity/grace-documentation>), based on the method of (*Swenson et al. 2008*).

Furthermore, the GRACE lower degree SHCs are prone to large uncertainty, especially the c_{20} zonal SHC due to e.g. tidal errors, satellite orbit configuration, and other limitations. Therefore, it is recommended to replace c_{20} with independent accurate estimate from SLR (LAGEOS-1 and -2, Starlette, Stella and Ajisai) provided by JPL (<https://podaac.jpl.nasa.gov/gravity/grace-documentation>), see GRACE Technical Note #11 (*Cheng and Ries 2017*). According to *Chen (2019)*, the uncertainty of the GRACE c_{20} is much larger on large scale mass change such as over Antarctica, and Greenland when compared to regional or small basin scale e.g. the GRACE-based global mean ocean mass estimate over 2005-2016 was reduced by about 0.3 mm/year by replacing the c_{20} with SLR estimate.

2.1.2.4 Glacial Isostatic Adjustment (GIA) correction

GIA is the viscoelastic response of the solid Earth and mantle to the past changes in surface loading by ice (glaciation and deglaciation). During the last ice age, a large volume of ice sheets was accumulated over Greenland, North America, Scandinavia, and Antarctica with thickness as large as 3-4 km, reaching its maximum about 21000 years ago (Last Glacial Maximum). Since then, these ice sheets began to melt and completed around 4000 years ago (*Huang 2013*). The melted water flowed and caused the sea level rise, which reported as 120 m approximately, since the last glacial maximum (*Peltier 2004*). During the ice age, the solid Earth crust had to experience subsiding caused by the load of the large thickness of the ice sheet, which results in the flow away of the mantle from the loading centre to the surrounding region. When the ice melted or decreased in size, the mantle material flowed back to the glaciated region causing crust uplift. This geophysical process of the crust relaxation (uplift) can still be observable e.g. it reaches over a centimetre per year in the Hudson Bay area (see Figure 2.3). The phenome is well documented from various studies (*see e.g. Ekman*

(1991); *Peltier et al. (2015)*, for historical reviews). The ongoing GIA process affects sea-level change observation, satellite altimetry, tide gauges, and most crucially to the time variable part of the Earth's gravity field (*Peltier 2004; Sjöberg and Bagherbandi 2017, Sect. 8*). Therefore, the estimation of mass change using GRACE data, in regions dominant with this phenomenon, should be corrected by removing the GIA signal. The only straightforward way to exclude this signal from the GRACE observation is to use a GIA model. Different ice loading history and Earth parameters have been used to infer the effects of GIA signal using GIA forward modeling. This prediction can be used in studying and correcting for different phenomena. The GRACE-based estimate of mass change in terms of equivalent water thickness can be corrected using the equivalent land uplift water thickness.

The GIA correction is only applied in our study for permafrost thawing in the northern high-latitude region, where the GIA signal is dominant. For this purpose, the land uplift rate using the ICE-6G (VM5a) model (*Peltier et al. 2015; see Figure 2.3*) is converted to equivalent land uplift water height (ELUWH) (*see Gido et al. 2019*) using the following formula:

$$ELUWH = \frac{\rho_e}{3\rho_w} \sum_{n=0}^{n_{max}} \frac{2n+1}{1+k_n} \sum_{m=-n}^n \dot{h}_{nm} Y_{nm}(\theta, \lambda) \quad (2.11)$$

where ρ_w is the water density \dot{h} is the land uplift rate. The secular rate computation will be explained later in section 2.2.

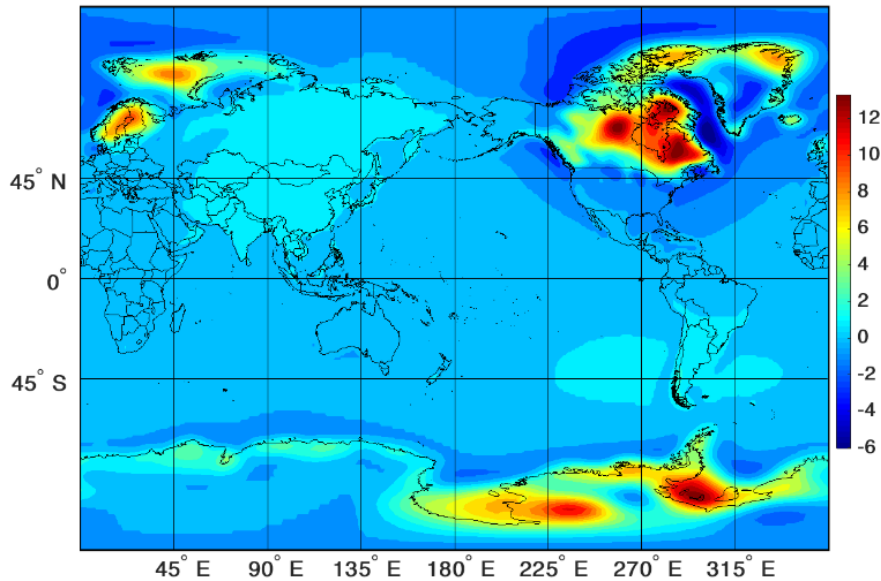


Figure 2.3. Land uplift rate using ICE-6G (VM5a) model (*Peltier et al. 2015*). Unit: mm/year.

2.1.2.5 GRACE data gap problem

In the GRACE solutions, some monthly data are missing, and in order to overcome this problem, the mean values of the data from months before and after the missing months are used for filling such gaps. It is worth mentioning here that all our data (i.e. that we used in the research paper) are within the period of GRACE mission, therefore we do not have to fill the gap between GRACE and GRACE-FO (see Table 2.3).

Table 2.3. GRACE and GRACE-FO on calendar. (Hatch patterns and GFO donates on GRACE data gaps and GRACE-FO, respectively).

Date	Jan	Feb	Mar	Apr	Maj	Jun	Jul	Aug	Sep	Oct	Nov	Dec
2002				1	2			3	4	5	6	7
2003	8	9	10	11	12		13	14	15	16	17	18
2004	19	20	21	22	23	24	25	26	27	28	29	30
2005	31	32	33	34	35	36	37	38	39	40	41	42
2006	43	44	45	46	47	48	49	50	51	52	53	54
2007	55	56	57	58	59	60	61	62	63	64	65	66
2008	67	68	69	70	71	72	73	74	75	76	77	78
2009	79	80	81	82	83	84	85	86	87	88	89	90
2010	91	92	93	94	95	96	97	98	99	100	101	102
2011		103	104	105	106		107	108	109	110	111	112
2012	113	114	115	116		117	118	119	120		121	122
2013	123	124		125	126	127	128			129	130	131
2014	132		133	134	135	136		137	138	139	140	
2015	141	142	143	144	145		146	147	148			149
2016	150	151	152		153	154	155	156			157	158
2017	159		160	161	162	163					---	--
2018	--	--	--	--	--	1 ^{GFO}	2 ^{GFO}			3 ^{GFO}	4 ^{GFO}	5 ^{GFO}
2019	6 ^{GFO}	7 ^{GFO}	8 ^{GFO}	9 ^{GFO}	10 ^{GFO}	11 ^{GFO}	12 ^{GFO}	13 ^{GFO}	14 ^{GFO}	15 ^{GFO}	16 ^{GFO}	17 ^{GFO}
2020	18 ^{GFO}	19 ^{GFO}	20 ^{GFO}									

2.2 Mass redistribution (GRACE applications)

Most of the month variability in the gravity field is caused by redistribution of mass within the ocean, atmosphere and water/snow stored on land. The mass variation is estimated from the GRACE Stokes coefficients similar to Eq. (2.1a), when mass changes within a thin layer at the Earth's surface, and by deformation of solid Earth in response to those mass redistribution.

By repeating the GRACE satellite tracks for estimating the gravity field, the linear least square regression analysis can be applied to compute the Earth's gravity field temporal changes (cf. *Sjöberg and Bagherbandi 2017, Ch. 2*). The linear regression formulas in time (t_i) with observation equation obtained from GRACE mission observed at different epochs can be given as:

$$a + bt_i = \Delta T_i - \varepsilon_i; \quad i = 1, \dots, n, \quad (2.12a)$$

where ε_i is the observations' random errors. In particular, if the time interval (Δt) between successive epochs is constant, ΔT_i is the disturbing potential anomaly (i.e. difference between consecutive months), and b is secular trend of the disturbing potential anomaly that is determined using least squares adjustment (*Sjöberg and Bagherbandi 2017*):

$$\hat{b} = \frac{2}{\Delta t} \frac{\sum_{i=1}^n (2i - n - 1) \Delta T_i}{\sum_{i=1}^n (2i - n - 1)^2} \quad (2.12b)$$

The periodic terms (annual, semi-annual and seasonal periods) should be estimated and removed, if they are necessary in the case studies (*Sjöberg and Bagherbandi 2017, Ch. 2*).

2.2.1 Total Water Storage (TWS) derived from GRACE

The global water cycle plays an important role in the Earth's climate system. Where the global atmosphere and oceanic circulation are directly affected by water mass redistribution and transportation (e.g. precipitation, evapotranspiration, moisture flow, ice melting, etc.) and their effects on the Earth's surface and atmosphere (i.e. heating and cooling). During the last several decades, Earth's climate system has experienced significant changes and variations with observable consequences and events (e.g. El Niño and La Niña, severe storms and floods, etc.). Therefore, for a better understanding of the Earth's climate system, improved monitoring of different hydrological components (e.g. precipitation, evapotranspiration, soil moisture, groundwater, etc.) are critical.

In the river basin and regions, Total Water Storage (TWS) change associated with the global water cycle can be achieved by the water balance equation as a function of unit time (Δt) as follow (*Chen 2019*):

$$\frac{\Delta TWS}{\Delta t} = P - ET - R \quad (2.13)$$

where P , ET and R denote for precipitation, evapotranspiration, and surface and sub-surface runoff parameters. Moreover, the water balance equation can also be expressed as an integration of water stored in the soil moisture, surface snow, groundwater, and surface water storage:

$$TWS = SM + SN + GWS + SWS \quad (2.14)$$

where SM , SN , GWS and SWS denote for soil moisture, snow, groundwater storage, and surface water storage, respectively. However, due to the lack of adequate in situ observations and continuous monitoring of all related components at basin or regional scales the total continental water storage is not well-known (*Rodell and Famiglietti 1999*).

The GRACE satellite gravity mission is greatly capable to monitor and quantify large scale TWS change globally. The GRACE data can be used for monitoring various types of mass changes in the Earth system, including the ice mass loss, sea level change, groundwater resource variations, and the mass variation inside the Earth. Therefore, the GRACE mission is capable to provide important information about land hydrology i.e. the sum of land water storage, which consists of surface and groundwater.

Due to the Earth's mass change, a time-dependent change in the gravity field causes changes in the spherical harmonic coefficient, which can be described by the residual spherical harmonic coefficients ΔC_{nm} that are obtained by subtracting the mean value of the GRACE-derived spherical harmonic coefficients \bar{C}_{nm} (i.e. the mean value within the desired period) from monthly GRACE solutions (SHCs). The absolute disturbing potential T and its anomaly (ΔT) can be estimated as follows:

$$\begin{pmatrix} T \\ \Delta T \end{pmatrix} = \frac{GM}{R} \sum_{n=0}^{n_{\max}} \left(\frac{R}{r} \right)^{n+1} \sum_{m=-n}^n \begin{pmatrix} C_{nm} \\ \Delta C_{nm} \end{pmatrix} Y_{nm}(\theta, \lambda), \quad (2.15)$$

$$\Delta C_{nm} = C_{nm} - \bar{C}_{nm}, \quad (2.16)$$

where GM is the geocentric gravitational constant (i.e. the product of Newton's gravitational constant and the total mass of the Earth including the atmosphere), C_{nm} are SHCs (i.e. c_{nm} and s_{nm}), R is the Earth's mean radius, Y_{nm} is the surface spherical harmonic of degree n and order m , and n_{\max} is maximum degree of harmonic expansion. (r, θ, λ) are, respectively, the geocentric radius, co-latitude and longitude of the computational point. Using linear regression analysis explained in section 2.2,

for the repeated GRACE satellite tracks, secular trend of the disturbing potential can be determined as:

$$\Delta\dot{T} = \frac{GM}{R} \sum_{n=0}^{n_{\max}} \left(\frac{R}{r}\right)^{n+1} \sum_{m=-n}^n \Delta\dot{C}_{nm} Y_{nm}(\theta, \lambda), \quad (2.17)$$

where $\Delta\dot{C}_{nm}$ is the secular change of the residual spherical harmonic coefficients. According to *Wahr et al. (1998)* the GRACE-based secular trend of the TWS change can be achieved by:

$$\Delta T\dot{W}S = \frac{R\rho_e}{3\rho_w} \sum_{n=0}^{n_{\max}} \frac{2n+1}{1+k_n} \sum_{m=-n}^n \Delta\dot{C}_{nm} Y_{nm}(\theta, \lambda), \quad (2.18)$$

where ρ_w is the density of fresh water, ρ_e is the Earth's mean density and k_n are load Love numbers of degree n , which can be modeled based on some Earth models (*Farrell 1972; Sun and Sjöberg 1999*) (see Table 2.1). For extracting the rate of ΔGWS , a hydrological model, e.g. GLDAS, should be used to estimate for the SWS (surface water storage).

2.2.2 Ground Water Storage (GWS) changes

In many parts of the world, groundwater is a vital resource for water supply. In addition, it is a major component of the global water cycle. However, accurate quantification of GWS has been challenging due to the lack of reliable in situ observation. Theoretically, it is possible to study any related components in the water balance equation (Eqs. 2.13 and 2.14) as long as others can be determined (*Chen 2019*). Therefore, an alternative tool has been provided by GRACE satellite gravimetry for monitoring and quantifying GWS at different spatial and temporal scales. Since 2009, numerous studies have used GRACE gravity data to detect and quantify GWS depletion in different regions over the globe, including Middle East (*Voss et al. 2013; Joodaki et al. 2014*), California's central valley (*Famiglietti et al. 2011; Scanlon et al. 2012*), and India (*Rodell et al. 2009; Chen et al. 2014; Tiwari et al. 2009*).

To use the GRACE-based TWS estimates to quantify for the GWS changes, other hydrological components (i.e. soil moisture, snow, runoff, etc.), determined from an independent source (e.g. land surface models (LSM) and/or in situ observation), should be removed from TWS :

$$G\dot{W}S = T\dot{W}S - (S\dot{M} + S\dot{N} + S\dot{W}S), \quad (2.19)$$

where \dot{SM} , \dot{SN} and \dot{SWS} are the rate of soil moisture, snow, surface water storage, respectively. It is worth noting that, any uncertainty in these components (i.e. SWS) will result as uncertainty in the GWS estimates.

2.3 Global hydrological models

Global and regional land surface models (LSMs) output or hydrological models such as Global Land Data Assimilation System (GLDAS) (Rodell et al. 2004), WaterGAP Global Hydrology Model (WGHM) (Döll et al. 2003) and World-Wide Water Resources Assessment (W3RA) provide an alternative means for studying TWS changes. Due to the lack of in situ observations as constraints, the water mass changes in the terrestrial water cycle can only be approximated by these models (Chen 2019). Therefore, they may be considered essential tools to compensate for the disturbance factors that contaminate the GRACE-based GWS estimates (e.g. soil moisture, precipitation, runoff, etc.). The models provide global information on land surface meteorological and hydrological status (e.g. surface temperature and soil moisture) with temporal resolutions based on integrating satellite and ground-based observations. According to Rodell et al. (2004) and Güntner et al. (2007) the LSMs may perform well at seasonal time scale, unlike at inter-annual and long term time scales, where often they show large uncertainty. Currently, different LSMs are used e.g. GLDAS Version-1, GLDAS Version-2, and WaterGap. Figure 2.4 shows the global surface water storage change (including soil moisture, snow, and runoff water changes) based on a) GLDAS NOAHv1 model, and b) WaterGap model for the period between 2002 and 2016 in mm/year. In the context of this thesis, both models (i.e. GLDAS and WaterGap) have been utilized in our study of mass changes and ground subsidence in Sudan's oil fields (**Paper III**) using GRACE data. Furthermore, the GLDAS was used in the permafrost study (**Paper II**) by the integration of satellite and in situ data in the northern high-latitude

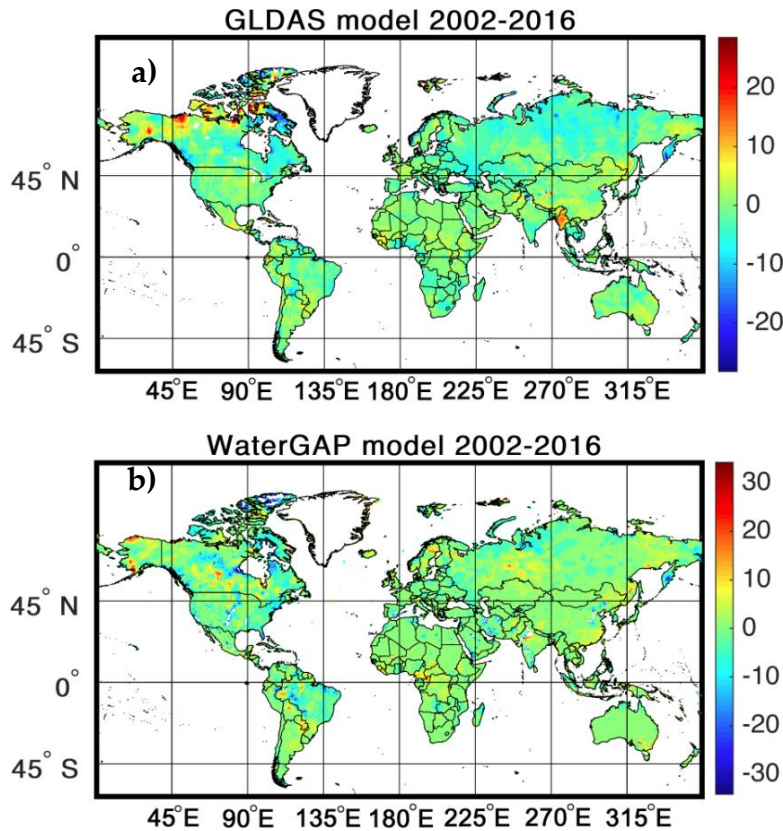


Figure 2.4. a) GLDAS surface water storage changes (including soil moisture, snow, and runoff water changes) using NOAHv1 model between 2002 and 2016, and b) Water storage changes in soil, snow, and surface water bodies from WaterGap model estimates for the same period. No smoothing or truncation has been applied to the data. Unit: mm/year.

2.3.1 Global Land Data Assimilation System (GLDAS)

The GLDAS integrates satellite and ground-based observational data, using advanced land surface modeling and data assimilation methods to generate an optimal field of land surface state (e.g. soil moisture, canopy, and temperature) and flux (e.g. evaporation and sensible heat flux) (Rodell *et al.* 2004). Currently, different GLDAS LSMs are in used e.g. GLDAS Version-1 that drives four models: NOAH, Mosaic, Variable Infiltration Capacity (VIC), and the Common Land Model (CLM). Whereas, the GLDAS Version-2 contains as well four models, NOAH, VIC, CLM, and the Catchment Land Surface Model (CLSM). The models have different spatial resolutions, e.g. 1.0 and 0.25 arc-degrees for NOAH and 1.0 arc-degree for the others. Temporal coverage of version-1 is from January 1, 1979 to present for the 1.0 arc-degree, and from February 24, 2000 to July 2017 for the 0.25 are-degree data (replaced by the corresponding GLDAS-2.1). In addition, the layers and depths are varied, e.g. NOAH contains four layers ranged from 0-2 meter depths. The GLDAS archived data

can be accessed through <http://disc.sci.gsfc.nasa.gov/>. These models have been utilized in **Paper II** and **Paper III**.

2.3.2 WaterGAP model

The WaterGAP Global Hydrology Model (WGHM) is a 0.5 arc-degree spatial resolutions, which has been developed at the Centre for Environmental Systems Research of the University of Kassel, Germany, in cooperation with the National Institute of Public Health and the Environment of The Netherlands (RIVM) (Döll *et al.* 2003; Döll *et al.* 2014a; Döll *et al.* 2014b). The model simulates continental water flows among all relevant water storage components for all land areas of the globe excluding Antarctica, including anthropogenic groundwater and surface water abstractions. The model has been calibrated against mean annual measured run-off. However, the models have limitations in reproducing observed large scale water storage change due to errors in climate forcing, and it has been reported in a number of studies including water storage data derived from the GRACE solutions (Eicker *et al.* 2014). In Figure 2.4b, we used monthly total storage for the period between 2002 and 2016. For more information about the model see e.g. (www.watergap.de; Schmied *et al.* 2014; Schmied 2017). This model has been used in **Paper III**.

2.4 Case studies

In this section, two case studies are presented, where geodetic satellite missions (e.g. GRACE) integrated by in situ data were used to study on large-scale mass changes.

2.4.1 Paper II:

"Studying permafrost by integrating satellite and in situ data in the northern high-latitude regions" Gido et al. (2019).

In this study, permafrost thawing and its associated gravity change in terms of GWS changes, and organic material changes have been studied using the GRACE solutions and other satellite and ground-based observations in the northern high-latitude regions. The estimation of permafrost changes in this region requires combining information from various sources, particularly using the gravity field change, surface temperature change, and glacial isostatic adjustment (GIA). The most significant factor for careful monitoring of this phenomena is, its possible contribution for releasing an additional enormous amount of greenhouse gases emitted to the atmosphere, most

important ones are the carbon dioxide (CO₂) and the methane that are currently stored in the frozen ground. Hence, studying thawing permafrost is very important, not only from a perspective of localized geo-hazard such as erosion, damage to buildings and infrastructure but also with respect to its possible global impact due to greenhouse gas emissions.

For this purpose, GRACE monthly solutions (RL05) processed by the CSR Centre (<ftp://podaac-ftp.jpl.nasa.gov/allData/grace/L2/CSR/RL05/>), covering the period between August 2002 to May 2016, and provided in terms of fully normalized geopotential SHC were used, to quantify the monthly rate of the TWS in the region. The mass variations due to permafrost thawing were estimated in terms of GWS changes using LSMs (e.g. GLDAS model). Moreover, the permafrost-related near-surface mass changes (due to permafrost thawing) were correlated with the released greenhouse gases. In order to achieve accurate results, the GRACE data processing (i.e. GIA, noises, etc.) should be addressed properly.

Similar to section (2.2.1), the GRACE-based TWS rates were estimated using time series analysis explained in section (2.2) and Eq. (2.18). The provided estimates were filtered and corrected for the GIA, hydrological signal, and the glacier melting, where the DDK2 non-isotropic filter, introduced by *Kusche (2007)*, was utilized to remove stripping pattern in the CSR GRACE data. For the GIA correction, the signal was converted to equivalent land uplift water height similar to Eq. (2.11) using the ICE-6G (VM5a) model, introduced by *Peltier et al. (2015)*. The GLDAS NOAHv1.0 LSM data were used over the period between Jan 2002 to May 2016 in order to estimate the permafrost related GWS. For the water storage change extraction due to permafrost thawing, the effect of ice-mass loss of Greenland ice sheet, triggered by regional warming, should be removed from the GRACE-based data. The rates of ice elevation changes were computed using altimeter surveys over the period of 2003-2012 supplemented with high-resolution ice, cloud, and land elevation satellite (ICESat) data from 2003 to 2009 (see *Khan et al. 2014*). However, the result showed that it is difficult to remove the ice elevation changes from GRACE data using the above-mentioned dataset and the estimated permafrost related GWS in Greenland is not trustable and should be ignored. The ice rate signal is very large because of the resolution of the altimetry data.

Similar to Eq. (2.19), the equivalent water height permafrost rates $\dot{E}WHP$ were achieved using the following formula:

$$\dot{E}WHP = \dot{T}WS - \dot{E}L\dot{U}WH - \dot{S}\dot{W}M \quad (2.20)$$

where ($\dot{E}L\dot{U}WH$) is the equivalent land uplift water height rate, ($\dot{S}\dot{W}M$) is the rate of surface water mass i.e. the rate of summation of the snow water equivalent, canopy, surface and subsurface run-off, soil moisture, and the water storage from the ice

melting in Greenland. The resulted GRACE-based TWS estimation, reveals the significant contribution of the GIA signal in the study region (see Figure 4 in **Paper II**).

The resulted *EWHP* were verified using in situ data e.g. land surface temperature from GLDAS (Rodell et al. 2004), borehole data and carbon dioxide changes (e.g. using NASA's EOS Aqua mission, see https://mirador.gsfc.nasa.gov/collections/AIRX3C2M_005.shtml).

Four selected stations located in Siberia (Turukhansky), North Alaska (Sagwon) and two more stations in Canada (Yukon and East of Hudson Bay) were used for further comparisons (see Figure 6 in **Paper II**), where reliable in situ data were available for the same time span as GRACE data. The GRACE-based GWS change showed positive trend of 3.4, 3.8, 4.4, and 4.0 cm/year in Siberia, North Alaska, Canada (Yukon), and Canada (Hudson Bay, Nunavut), respectively, most probably due to permafrost thawing (see Figure 8 in **Paper II**). The greenhouse gases, i.e. carbon dioxide (CO₂) and methane, increased up to 2.2 PPM/year in the study areas over the same period (see Figure 7 in **Paper II**). Temperature also showed positive trend generally in the study area (see Figure 9 in **Paper II**) as well as CO₂ and equivalent water height trend (due to permafrost thawing) which might confirm the permafrost carbon feedback process (see Table 2.4).

Table 2.4. Secular trends of permafrost equivalent water height (EWHP), average surface temperature, and CO₂ at selected stations.

Location	EWHP (cm/year)	Soil surface temperature C° /year)	Soil surface temperature (Celsius within 100 years)	CO ₂ (PPM)
Siberia (Turukhansky)	+3.4	+ 0.013	+1.2	2.31
North Alaska (Sagwon)	+3.8	+ 0.081	+8.1	2.16
Canada (Yukon)	+4.4	- 0.114	-11.4	2.21
Canada (Hudson Bay, Nunavut)	+4.0	+ 0.050	+5.0	2.20

2.4.2 Paper III:

"Satellite monitoring of mass changes and ground subsidence in Sudan's oil fields using GRACE and Sentinel-1 data", Gido et al. (2020).

In this study, a comprehensive investigation about the relation between oil production, GRACE-based GWS estimation, and monitoring ground subsidence in response to extraction cycles in nine oil fields in Sudan, have been performed (see Figure 1, **Paper**

III). GRACE monthly solutions (RL06) processed by the CSR Centre (<ftp://podaac-ftp.jpl.nasa.gov/allData/grace/L2/CSR/RL06/>), covering the period between Jan 2003 to Sep 2012, were used, to quantify monthly TWS in the region using time series analysis explained in section (2.2). Since using GRACE data one cannot differentiate between the various surface water storage signals (e.g. soil moisture, groundwater, and precipitation), the obtained secular rate has been filtered by external hydrological models. The integration of the GRACE data with the land surface hydrological models, e.g. GLDAS or WaterGap models, allowed us to extract the individual components from the equivalent water storage estimated and leads to determine the GWS changes due to the oil mass depletion in the study area. Then the results were correlated with the available oil wells production data (i.e. in situ) for the period of 2003-2012.

Extraction of large volumes of water and oil decreases the reservoir pressure, form compaction, and consequently, land subsidence occurs which can be analyzed by both GRACE and Synthetic Aperture Radar (SAR) data (e.g. Sentinel-1). Using the freely available Sentinel-1 SAR data, collected between November 2015 and April 2019, the ground surface deformation associated with this oil and water depletion has been studied. Due to the lack of terrestrial geodetic monitoring data in Sudan, the use of GRACE and Sentinel-1 satellite data is very valuable to monitor water and oil storage changes and their associated land subsidence.

The GRACE-based TWS has been estimated after applying the steps in Section 2.1.2 i.e. degree one coefficients, which represent the position of the Earth's instantaneous centre of mass relative to an Earth-fixed reference frame, have been added based on the GRACE Technical Note #13b. Degree 2 coefficients have been replaced by those introduced by SLR solutions in TN-11_C20_SLR_RL06 (GRACE Technical Note TN-11) consistent with the GRACE SDS recommendations. The maximum degree/order of 96/96 has been considered, and seasonal signals have not been removed. Moreover, the gravity data collected by the GRACE require smoothing to reduce the effects of errors present in short-wavelength components. Various methods have been proposed to filter the data (*Kusche 2007; Wouters and Schrama 2007*). Both isotropic (Gaussian) associated with 300 and 500 km radius and non-isotropic (DDK) filters were employed to reduce the effect of the correlated noises in the GRACE data. However, none of these methods account for correlated errors in the data. GIA correction was not considered in this area.

Similar to sections (2.2.1), the GRACE-based ΔTWS rate has been estimated using Eq. (2.18). Moreover, four different data sets of monthly hydrological LSMs, the 1.0 arc-degree of GLDAS data i.e. NOAHv1.0, NOAHv2.1, CLSMv2.0 (Version-1 and -2 respectively), and the 0.5 arc-degree WGHM, were utilized to remove the hydrological effects (i.e. SWM) from the GRACE-based TWS using Eq. (2.19).

Figure 2.5 shows the secular rate of the estimated ΔTWS and ΔGWS , using GRACE (CSR centre and DDK1 filter) and GLDAS (CLSM model) data, respectively, over the study period and region. The results were correlated with the available oil wells production data (see Figure 1 and 3, **Paper III**) for the period of 2003-2012.

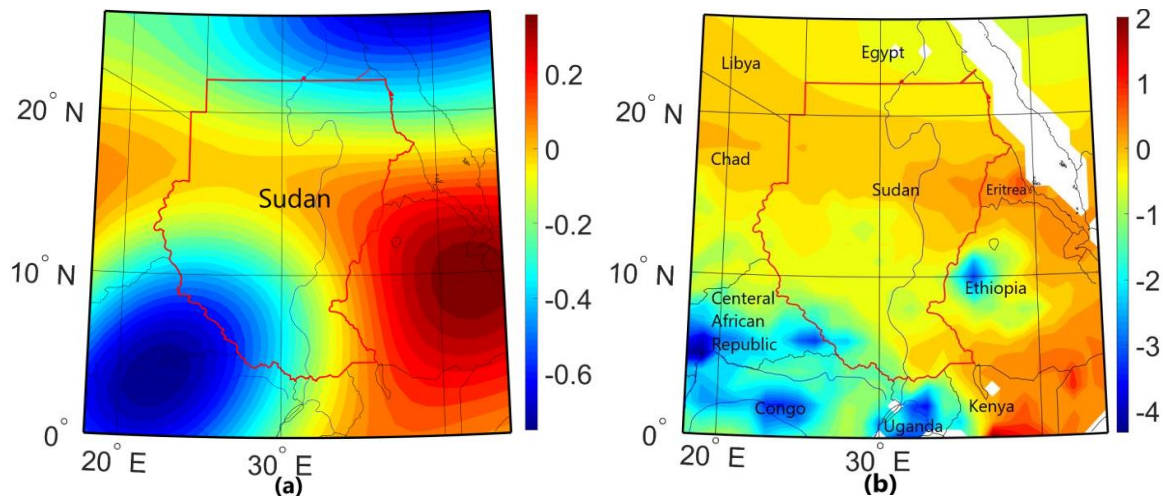


Figure 2.5. Secular rate of (a) the estimated total water storage anomaly (ΔTWS) and (b) the estimated groundwater storage anomaly (ΔGWS), using Gravity Recovery and Climate Experiment (GRACE) (Centre for Space Research (CSR) centre and DDK1 filter) and GLDAS (CLSM model) data, respectively, over the period of Jan 2003–Sep 2012. Unit: cm/year.

The results show that the trend of GWS changes due to water and oil depletion ranged from -18.5 ± 6.3 to -6.2 ± 1.3 mm/year using the CSR GRACE monthly solutions and the best tested hydrological model in this study, where the achieved rates are highly dependent on the choice of decorrelation filter and the hydrological models. The analysis based on applying DDK1 decorrelation filter and utilizing the GLDAS-CLSMv2.0 model results in a high correlation (0.74 correlation coefficients) between the estimated GWS and oil and water extraction in the study area (see Table 4 in **Paper III**). Except for the resolution of GRACE data, the main source of uncertainty in the GWS estimates is related to hydrological models, which reveal a strong relation with the rainfall trend in the region. According to the achieved results, GRACE data can significantly help to monitor the mass changes due to heavy oil productions, if we could solve the remarkable uncertainty in hydrological models in the future (see Figures 5 and 6 in **Paper III**). Furthermore, three Sentinel-1 A and B data sets were utilized and processed in this study. Their results and finding will be discussed and presented in chapter 4.

Chapter 3

Isostatic equilibrium and disturbances

3.1 Introduction

The main motivation for presenting isostasy in this section is to explain the relationship between isostatic equilibrium and the Earth's dynamic processes particularly the density heterogeneity of the crust and mantle, which can control tectonic processes and seismicity. Isostasy is a fundamental concept in the geoscience and its definition can be found in *Sjöberg and Bagherbandi (2014)*:

"Isostasy (Greek isos "equal", stasis "stand still") is a term in geology, geophysics and geodesy to describe the state of mass balance (equilibrium) between the Earth's crust and upper mantle. It describes a condition to which the mantle tends to balance the mass of the crust in the absence of external forces."

Archimedes' principle of hydrostatic equilibrium can be used to define the isostatic equilibrium. In accordance with Archimedes' principle, a mass can float in a dense environment and it displaces its own weight. An iceberg that sinks lower in the water is a good example of isostatic equilibrium. Similarly, Earth's crust floats in the upper mantle. Earth topography or in proper term a mountain range is floating on the denser mantle (*Watts 2001*). According to *Bagherbandi (2011)* and *Sjöberg and Bagherbandi (2014)*:

"When a certain area of the crust reaches the "state of isostasy", it is said to be in isostatic equilibrium (balance), and the depth at which isostatic equilibrium prevails is called the compensation depth. Although it is generally accepted that the Earth is a dynamic system that responds to loads in many different ways, isostasy still provides an important view of the on-going processes."

Therefore, isostasy is important principle for analysing geodynamic processes in the crust and upper mantle. As the isostasist can serve the seismologist for studying the causes and effects of geodynamics phenomena, such as earthquakes and seismicity, meanwhile the seismologist can be of great assistance to the isostasist (*Bowie 1926*). Our

numerical studies (**Paper I and IV**) are good examples that confirm this. For example, it shows that the distribution of earthquakes and volcanic areas has a direct relationship with very weak crust. The correlation between the large negative isostatic gravity disturbances and seismicity is also approved by observed data and theoretically (*cf. Artemjev et al. 1972*). For instance, (*Eshagh 2015*) showed the relation between the sub-crustal stress components and the Moho depth induced by mantle convection. In other words, the isostatic equilibrium can be disturbed by the stresses set up by variations in volume and also by the displacing of the Earth's interior materials horizontally or vertically. In addition, isostasy can explain the state of mass balance in the earth's interior as it is very important for studying the mass deficiency or extra mass beneath the Earth surface and complete and incomplete isostatic equilibrium (*Bagherbandi 2011*). *Heiskanen and Vening Meinesz (1958 p. 124)* introduced under- and over-compensation instead of incomplete isostatic equilibrium. Therefore, having knowledge about crustal parameters variations (depth and density contrast) under different geological units is a major contribution in understanding of tectonic and geodynamics processes.

3.2 Isostatic and seismic crust models (the Moho)

The Mohorovičić discontinuity (or Moho) is the boundary between Earth's crust and mantle. The Moho depth varies between 25 to more than 80 km beneath continents and from 5 to 15 km beneath oceans. Determination of the Moho depth is essential for geodynamic modeling, such as evaluation of seismic hazard or understanding earthquake source mechanism, and other geophysical applications. The Moho can be obtained using isostatic or seismic models (Table 3.1). The Moho depth is primarily detected from seismic data. Unfortunately, seismic data coverage in many places is low e.g. in Africa. Gravity data is used to determine the Moho depth where seismic surveys are insufficient. Gravimetric campaigns have been carried out in many countries to the extent that large parts of the continents are now covered by gravity measurements. Moreover, satellite gravity missions provide information about Earth's gravity field globally. Today, gravimetric-isostatic methods are much more cost-effective, allowing crustal thickness to be estimated by gravity inversion under the assumption of some isostatic models, e.g. (*Airy 1855*), (*Pratt 1855*), (*Vening-Meinesz 1931*), and *Vening Meinesz–Mortiz*, (*Moritz 1990; Sjöberg 2009*).

Table 3.1. Different isostatic and seismic crustal models.

	Model	Reference	Area of compensation	Region
Isostatic Models	Airy	<i>Airy (1855)</i>	Local	Global
	Pratt	<i>Pratt (1855)</i>	Local	Global
	Vening Meinesz	<i>Vening-Meinesz (1931)</i>	Regional	Global
	Parker-Oldenburg	<i>Parker-Oldenburg (1974)</i>	Regional	Global
	Vening Meinesz	<i>Vening-Meinesz (1931)</i> <i>Moritz (1990)</i>	Regional/Global	Global
	Vening Meinesz Moritz (VMM)	<i>Sjöberg (2009)</i>	Regional/Global	Global
Seismic Models	CM91	<i>Čadek and Martinec (1991)</i>	----	Global 6°×6°
	CRUST5.0	<i>Mooney et al. (1998)</i>	----	Global 5°×5°
	CRUST2.0	<i>Laske et al. (2000)</i>	----	Global 2°×2°
	CRUST1.0	<i>Laske et al. (2013)</i>	----	Global 1°×1°
	GRAD	<i>Grad et al. (2009)</i>	----	Europe
	Baranov	<i>Baranov (2010)</i>	----	Asia and East Africa

The seismic models are determined using tomography technique that is primarily used to detect the Moho depth based on the analysis of seismic waves due to earthquakes and (controlled) explosions. This technique involves several different methods for processing the P (Primary wave), S (Secondary wave or shear wave), and surface waves on the principle of solving inverse problems for finding locations of reflection and refraction of the wave pathways in order to create tomographic models. This method has, however, practical limitations. Since active seismic experiments are relatively expensive, large parts of the world are not yet covered sufficiently by seismic surveys. Nevertheless, the Moho depth estimates from seismic data are essential to constraint the Moho depth model determined based on the gravity data inversion. The CRUST1.0 global seismic crustal model (*Laske et al. 2013*) is an upgraded version of the previous CRUST2.0 and CRUST5.1 models, where the Moho depth of unsampled regions (such as large parts of Africa and Asia) was statistically inferred according to basement age or tectonic setting. CRUST2.0 and CRUST1.0 were the most frequently used models in geodynamic and gravity modeling. Both models have also been extensively used for crustal corrections in seismological studies.

The principles of isostasy by *Airy (1855)* and *Pratt (1855)* models are based on local compensation i.e. they assume the topographic mass is uniformly compensated along each vertical column (i.e. local compensation). Pratt's model is based on a constant

compensation depth and a variable density contrast, while Airy's model assumes a constant topographic density contrast with a variable compensation depth. As the Earth's crust is very complicated, the assumption of constant density or compensation depth for different topographic columns is not realistic and it is closer to a regional compensation model rather than the local compensation model (Figure 3.1). Therefore, a gravimetric-isostatic model that assumes a variable Moho depth and crustal density (density contrast) should be considered to overcome this problem. Recently, number of gravity-based global Moho depth models were presented, which take advantage of a global coverage of Earth's gravity field measured by satellite gravity missions. Inverting gravity data for the Moho depth determination has been applied to generate models that are only based on gravity observations, such as the *Vening Meinesz-Moritz* model by *Sjöberg (2009)* and *Bagherbandi et al. 2013*).

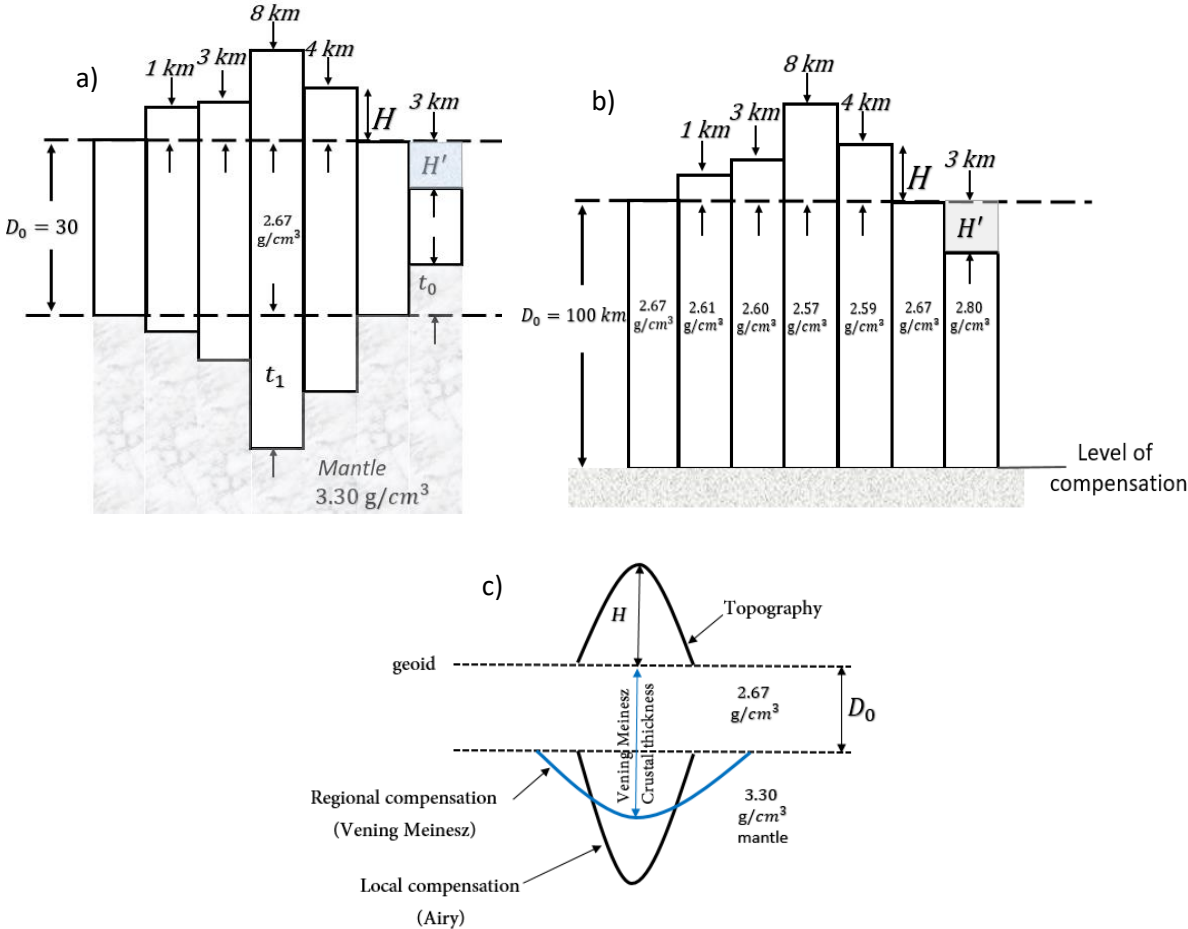


Figure 3.1. Local vs. regional topographic mass compensation using a) Airy, b) Pratt, and c) VMM model (figure modified after: *Sjöberg and Bagherbandi 2017*).

3.3 Veining Meinesz-Moritz model

Vening Meinesz isostatic hypothesis model was generalized by *Moritz (1990, Sect. 8)*. He modified the original *Vening Meinesz* model (that assumes a regional isostatic compensation and a flat Earth approximation) into a model with a global compensation and spherical sea level approximation (Figure 3.1c). Later, *Sjöberg (2009)* presented the *Vening Meinesz-Moritz (VMM)* method by modifying the *Moritz's* solution using a non-linear Fredholm integral equation of the first kind. The VMM solution was modified more by *Tenzer and Bagherbandi (2012)*, *Sjöberg (2013)*, and *Bagherbandi et al. (2013)* using more trustworthy reduction of the topographic attraction correction in the gravimetric observation (it is so-called no-topography gravity anomaly or the Bouguer gravity disturbance in *Sjöberg and Bagherbandi 2017, Ch. 8*).

By considering *Vening Meinesz* hypothesis the Moho depth D can be determined by adding compensating attraction A_c to the Bouguer gravity disturbance δg_B :

$$\delta g^f = \delta g_B + A_c \approx 0 \quad (3.1)$$

such that, the compensation attraction A_c compensates the δg_B . However, as stated in **Paper IV**, there are other effects e.g. non-isostatic effects that disturb the isostatic equilibrium. The Moho depth, exists implicitly in Eq. (3.1) and it can be estimated using an inversion technique. This gravimetric-isostatic method is called *Vening Meinesz-Mortiz (VMM)* method (*Sjöberg (2009)*; *Bagherbandi et al. 2013*). According to *Sjöberg (2009)* the gravimetric-isostatic Moho depth can be obtained by the following Fredholm's integral equation of the first kind (cf. *Bagherbandi et al. 2013*):

$$R \iint_{\sigma} \left[\sum_{n=0}^{\infty} \frac{n+1}{n+3} [1 - (1-\tau)^{n+3}] P_n(\cos\psi) \right] d\sigma = -(\delta g^{TBIS} + A_{c0}) / (G\Delta\rho), \quad (3.2)$$

by assuming

$$A_c = A_{c_0} + RG\Delta\rho \iint_{\sigma} \left[\sum_{n=0}^{\infty} \frac{n+1}{n+3} [1 - (1-\tau)^{n+3}] P_n(\cos\psi) \right] d\sigma, \quad (3.3)$$

where $\tau = D/R$, G is gravitational constant, R is the Earth's mean radius, σ is the unit sphere, P_n Legendre polynomials, $\Delta\rho$ is crust-mantle density contrast ($\Delta\rho = \rho_{mantle} - \rho_{crust}$), A_{c_0} is normal compensation attraction ($\approx -4\pi G\Delta\rho D_0$), D_0 is mean Moho depth, ψ is the geocentric angle between the computation (P) and integration (Q) points and δg^{TBIS} is the free-air gravity disturbance (δg^f) corrected by additive gravity corrections due to

the topographic mass δg^t , density contrasts of the ocean (i.e., the bathymetry δg^b), ice δg^i , and sediments δg^s i.e.:

$$\delta g^{TBIS} = \delta g^f + \delta g^t + \delta g^b + \delta g^i + \delta g^s \quad (3.4)$$

After some simplifications the Moho depth can be estimated by:

$$D(P) = D'(P) + \frac{D'^2(P)}{R} - \frac{1}{32\pi R} \iint_{\sigma} \frac{D'^2(Q) - D'^2(P)}{\sin^3(\psi/2)} d\sigma_Q, \quad (3.5)$$

where

$$D'(P) = \frac{1}{4\pi G \Delta \rho} \sum_{n=0}^{\infty} \left(2 - \frac{1}{n+1} \right) \sum_{m=-n}^n \delta g_{nm}^{TBIS} Y_{nm}(P), \quad (3.6)$$

Y_{nm} is the fully-normalized spherical harmonic of degree n and order m . δg_{nm}^{TBIS} is spherical harmonic coefficients of δg^{TBIS} . In order to solve for singularity problem in Eq. 3.5, *Sjöberg (2009)* proposed the near zone contribution method by using a planar approximation within the cap size ψ .

3.3.1 Gravimetric forward modelling

The medium and short wavelengths of observed gravity field largely reflect the gravitational signal of topography and crustal density heterogeneities, while the long-wavelength part of the gravity field is controlled by the gravitational signature of deep masses i.e. deep mantle. The gravitational signature of the Moho is not apparent in the observed gravity field, then the signature of the Moho can be inferred by employing gravity corrections. The gravity corrections should be subtracted from observed gravity data i.e. subtracting the gravitational signature of topography (including crustal density heterogeneities) from the gravity data. The outcome of this procedure is the Bouguer gravity data, which is used for the Moho determination (see Eq. 3.1). By using the Newtonian integration one can determine the gravity corrections (it is also called forward modelling). For example, for removing the topographic effect using the Newtonian integration, the topographic potential is given by:

$$V^t(P) = G \iint_{\sigma} \bar{\rho}_c \int_R^{R+H} \frac{r_Q^2}{l_{PQ}} dr d\sigma, \quad (3.7a)$$

where H is topographic height, l_{PQ} is distance between points P and Q , r_Q is the Earth radius at point Q , and $\bar{\rho}_c$ is the mean density of the crust:

$$\bar{\rho}_c = \begin{cases} \rho_c & \text{continent} \\ \rho_c - \rho_w & \text{ocean} \end{cases} \quad (3.7b)$$

The Bouguer gravity anomalies are determined by subtracting the gravitational contribution of topography from the free-air gravity anomaly (Δg) i.e.:

$$\Delta g_B = \Delta g - A^t \quad (3.7c)$$

where $A^t = -\partial V^t / \partial r_p$. To calculate the Bouguer gravity data one needs to utilize the additional correction to obtain the no-topography gravity anomaly according to the definition of the fundamental equation of the physical geodesy (*Heiskanen and Moritz 1967; Vaníček et al. 2004; Sjöberg 2013*). Using the fundamental equation of physical geodesy, we know that (*Sjöberg and Bagherbandi 2017, Ch. 8*):

$$\Delta g = \delta g + \frac{\partial \gamma}{\partial h} \frac{T}{\gamma} \approx \delta g - 2 \frac{T}{r} \quad (3.7d)$$

where δg is the gravity disturbance, γ is normal gravity, T is disturbing potential, r is the radius from the geocentre and h is the height along the normal to the ellipsoid.

If we replace the disturbing potential T with topographical potential (*Sjöberg 2013*), the topographic effect on the gravity anomaly Δg^t becomes:

$$\Delta g^t = A^t + \frac{\partial \gamma}{\partial h} \frac{V^t}{\gamma} \approx A^t - 2 \frac{V^t}{r} \quad (3.7e)$$

Therefore, the no-topography gravity anomaly (Δg^{nt}) can be written by:

$$\Delta g^{nt} = \Delta g - \Delta g^t, \quad (3.7f)$$

The no-topography gravity anomaly is compatible with the Bouguer gravity disturbance (δg_B) according to *Sjöberg and Bagherbandi (2017, Ch. 8)*. The Bouguer gravity disturbance is given by:

$$\delta g_B = \delta g - A^t \quad (3.7g)$$

As it can be seen in Eq. (3.7e) A^t is the direct effect of the topographic gravity anomaly which differs from the gravity disturbance by the term $2V^t / r$, which is the secondarily indirect topographic effect. Therefore, the Bouguer gravity disturbance is closer to the

no-topography gravity data because it contains a remaining topographic contribution that is only removed by applying $2V' / r$ term. Preliminary numerical results of *Tenzer and Bagherbandi (2012)* and *Tenzer et al. (2015)* confirm this theory. Therefore all gravitational signals should be taken into account. This is the reason for employing the gravity disturbances data, in this study, instead of the gravity anomaly data in Eq. (3.1).

To model the gravitational signature of topography and crustal density heterogeneities, we used CRUST1.0 model. This model gives data on a 1×1 degree grid for several layers comprising the ice sheets (in Greenland and Antarctica), water thickness (in three areas are forced to NOT have water even though they are below sea level: Caspian Depression, Qattara Depression in Egypt, Lake Eyre in Australia), and upper, middle and lower sediments crustal layers (*Laske et al. 2000* and *Laske et al. 2013*). To model the gravitational signature of topography using forward modeling (*Gladkikh and Tenzer 2012*); *Bagherbandi et al. 2013*; *Tenzer et al. 2015*), we used the 1×1 arc-degree data from the Earth2014 (*Hirt and Rexer 2015*) datasets of topography, bathymetry, inland bathymetry (major lakes) and glacier bedrock. The Earth2014 was compiled from the latest data releases of the SRTM30_PLUSv9, the SRTMv4.1, the BEDMAP2 and the Greenland Bedrock Topography GBTv3. Figure 3.2 shows a global maps of topography, bathymetry, and ice-sheet thickness using Earth2014 model (*Hirt and Rexer 2015*). Figure 3.3 shows global maps of crustal thickness and sediment thickness using CRUST1.0 model (*Laske et al. 2013*).

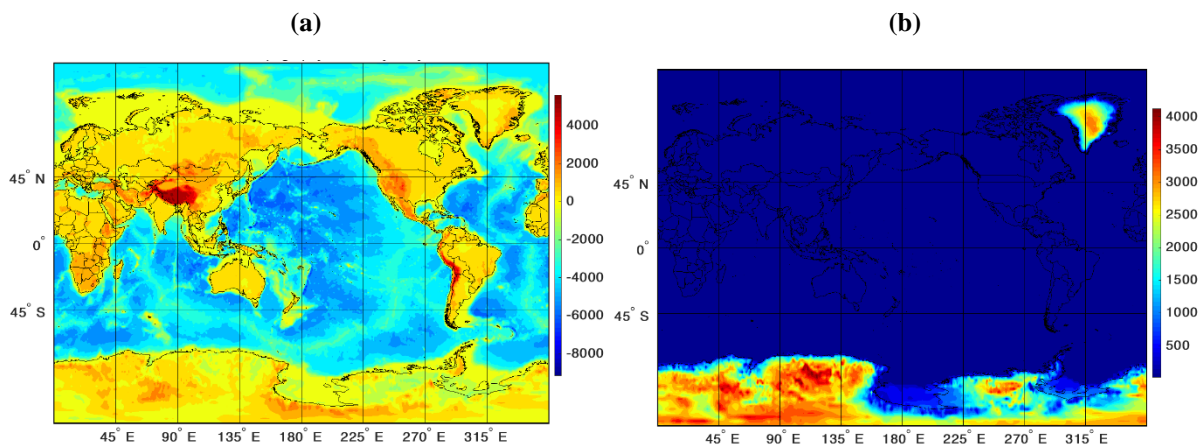


Figure 3.2. a) Earth2014 topography, bathymetry, and b) Earth2014 ice-sheet thickness models (*Hirt and Rexer 2015*) with spatial resolution of 1×1 arc-degree. Unit: meter.

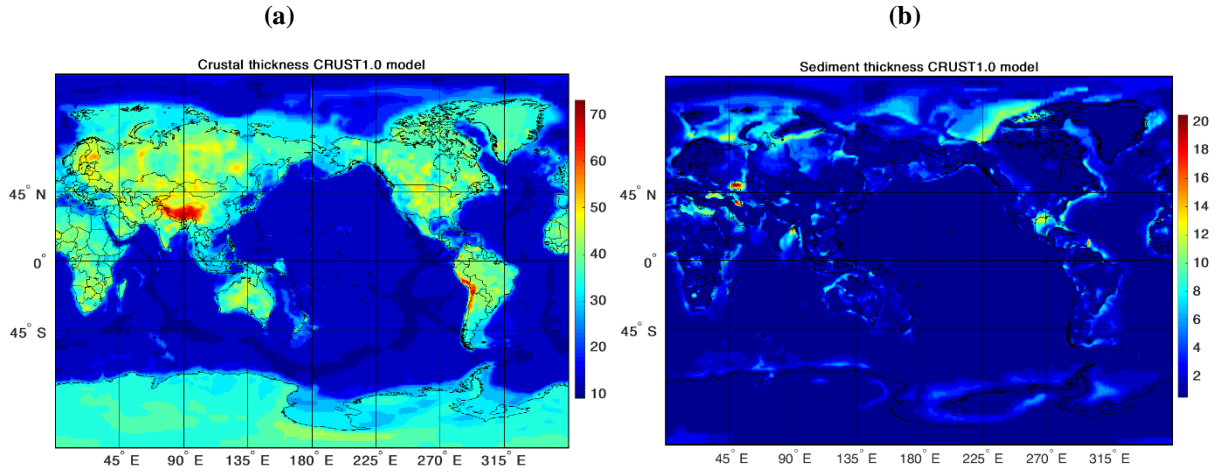


Figure 3.3. a) Crustal thickness, and b) Sediment thickness using CRUST1.0 model (Laske et al. 2013) with spatial resolution of 1×1 arc-degree. Unit: km.

Using the above-mentioned data in the forward modelling one can model the gravitational signatures of topography, bathymetry, ice, and crustal density heterogeneities. This is also called additive corrections in *Sjöberg and Bagherbandi (2017, Ch. 8)*.

The expression for the gravitational attraction generated by an arbitrary volumetric mass layer with a variable depth and thickness can be obtained using the following equations. Simply, the spherical harmonic analysis for determination of the effects of major known crustal density structures can be written:

$$c_{nm}^q = \frac{3}{(2n+1)\rho_e} \left[\frac{(\rho^q L_q)_{nm}}{R} + \frac{n+2}{2} \frac{(\rho^q L_q^2)_{nm}}{R^2} + O_{nm} \right], \quad (3.8a)$$

and

$$(\rho^q L_q^j)_{nm} = \frac{1}{4\pi} \iint_{\sigma} (\text{density})^q (\text{thickness}^j)^q Y_{nm}(Q) d\sigma, \quad j = 1 \text{ and } 2, \quad (3.8b)$$

where $\rho_e \approx 5500 \text{ kg/m}^3$ is the mean density of the Earth's mass, ρ^q and L_q are density and thickness of the layers. Here q denotes either the topography, bathymetry, ice, and sediment. O_{nm} is the effect of higher order terms. Finally, the gravity disturbance corrections (in Eq. 3.4) are given by

$$\delta g^q = \frac{GM}{R^2} \sum_n^{n_{max}} (n+1) \sum_{m=0}^n c_{nm}^q Y_{nm}(P), \quad (3.8c)$$

GM is the geocentric gravitational constant and n_{max} is maximum spherical harmonic degree.

Figure 3.4 shows a global map of the gravity disturbance δg^f , using XGM2016 model (Pail et al. 2017). Figure 3.5 shows global maps of the additive gravity corrections (using Eq. 3.8c) for topography (δg^t), bathymetry (δg^b), ice (δg^i), using Earth2014 model, and sediment (δg^s), using CRUST1.0 gravity corrections with spatial resolution of 1×1 arc-degree.

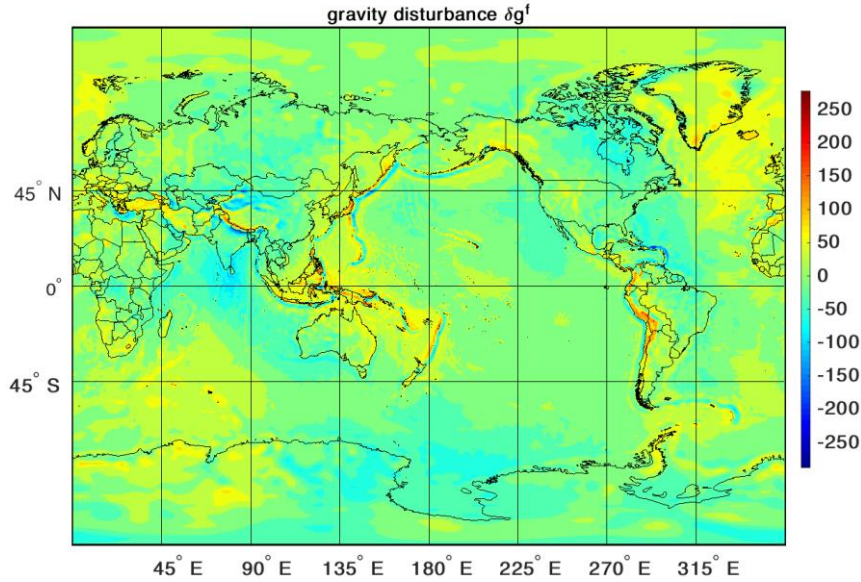


Figure 3.4. Gravity disturbance δg^f (using XGM2016 model) with spatial resolution of 1×1 arc-degree. Unit: mGal.

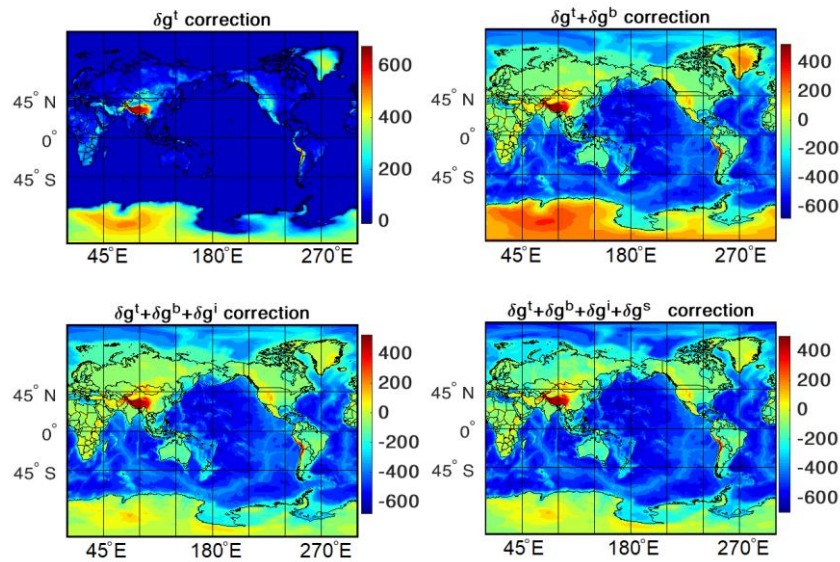


Figure 3.5. Topography (δg^t), bathymetry (δg^b), ice (δg^i) (using Earth2014 model), and sediment (δg^s), using CRUST1.0 gravity corrections with spatial resolution of 1×1 arc-degree. Unit: mGal.

3.4 Moho density contrast determination

Using the first-order Fredholm integral equation presented by *Sjöberg (2009)*, we can determine the Moho density contrast using the VMM method if we assume that the Moho depth D is known e.g. from the seismic Moho model of CRUST1.0 (*Sjöberg and Bagherbandi 2011*):

$$R \iint_{\sigma} \Delta\rho \left[\sum_{n=0}^{\infty} \frac{n+1}{n+3} \left[1 - (1-\tau)^{n+3} \right] P_n(\cos\psi) \right] = -(\delta g^{TBIS} + A_{C0}) / G, \quad (3.9a)$$

The right hand-side of Eq. (3.9a) can be expanded into a Taylor series and after performing some simplifications (see Appendix B in **Paper IV**):

$$R \iint_{\sigma} \Delta\rho \left[\sum_{n=0}^{\infty} \frac{n+1}{n+3} \left[1 - (1-\tau)^{n+3} \right] P_n(\cos\psi) \right] d\sigma = 4\pi \sum_{n=0}^{\infty} \sum_{m=-n}^n \frac{n+1}{2n+1} \left[(\Delta\rho D)_{nm} - \frac{n+2}{2R} (\Delta\rho D^2)_{nm} \right] Y_{nm}(P), \quad (3.9b)$$

From Eqs. (3.9a) and (3.9b) we obtain the spectral equation

$$\left[(\Delta\rho D)_{nm} - \frac{n+2}{2R} (\Delta\rho D^2)_{nm} \right] = \frac{2n+1}{4\pi(n+1)} \left[-(\delta g^{TBIS} + A_{C0}) / G \right]_{nm}, \quad (3.9c)$$

By considering an approximation $(\Delta\rho D^2)_{nm}$ by $D_0 (\Delta\rho D)_{nm}$, the Moho density contrast can be estimated using:

$$\Delta\rho \approx \frac{1}{4\pi D} \sum_{n=0}^{\infty} \sum_{m=-n}^n \frac{2n+1}{n+1} \left(1 + \frac{D_0}{R} \frac{1}{\frac{2}{n+2} - \frac{D_0}{R}} \right) \left[-(\delta g^{TBIS} + A_{C0}) / G \right]_{nm} Y_{nm}(P), \quad (3.9d)$$

3.5 Moho parameters determination: A combined model to estimate Moho depth and density contrast

The gravimetric Moho usually differs from the seismic Moho models due to several reasons, such as uncertainties of density models used for the gravimetric forward modeling and the remaining (unmodeled) gravitational contribution of deep mantle density heterogeneities (non-isostatic effects, *Bagherbandi and Sjöberg 2012*), etc. Furthermore, the gravimetric Moho depth is based on adopting a particular isostatic

theory while some crustal structures are either under or over-compensated (*Heiskanen and Vening Meinesz 1958*). Consequently, the Moho depth estimated from gravity data will not coincide with the one that estimated using seismic data. To solve this problem, the Moho depth determined from gravity can be combined with seismic estimates (*Bagherbandi 2011*).

The proposed method is almost similar to *Sjöberg and Bagherbandi (2011)*, where we added one more observation equation in the combined least-squares adjustment technique (see l_4 Eq. 3.10b):

$$\hat{\mathbf{X}} = (\mathbf{A}^T \mathbf{Q}^{-1} \mathbf{A})^{-1} \mathbf{A}^T \mathbf{Q}^{-1} \mathbf{L}, \quad (3.10a)$$

where

$$\mathbf{A} = \begin{bmatrix} \Delta\rho_o & D_o \\ 0 & 1 \\ 1 & 0 \\ 0 & 1 \end{bmatrix}, \mathbf{X} = \begin{bmatrix} dD \\ d\Delta\rho \end{bmatrix} \text{ and } \mathbf{L} = \begin{bmatrix} l_1 - \Delta\rho_o D_o \\ l_2 - \Delta\rho_o \\ l_3 - D_o \\ l_4 - \Delta\rho_o \end{bmatrix}, \quad (3.10b)$$

Here, D_o and $\Delta\rho_o$ are the approximate values of the Moho depth (\hat{D}) and the crust-mantle density contrast ($\Delta\hat{\rho}$), respectively. The observation vector \mathbf{L} is composed of the observations $l_1 = \Delta\rho D$ (see Appendix B Eq. B4 in **Paper IV**), $l_2 = \Delta\rho_{VMM}$ (this parameter can be estimated using the VMM method presented in section 3.4, Eq. 3.9d), $l_3 = D_{seismic}$, given by a seismic crustal thickness model (*Baranov 2010*), and $l_4 = \Delta\rho_{CRUST1}$ is estimated by the density contrast obtained from CRUST1.0 model (*Laske et al. 2013*). The variance-covariance matrix is defined by (*Sjöberg and Bagherbandi 2011*):

$$\mathbf{Q} = \begin{pmatrix} \sigma_{\Delta\rho D}^2 & \sigma_{\Delta\rho D}^2 / D_o & 0 & 0 \\ \sigma_{\Delta\rho D}^2 / D_o & \sigma_{\Delta\rho_{VMM}}^2 & 0 & 0 \\ 0 & 0 & \sigma_D^2 & 0 \\ 0 & 0 & 0 & \sigma_{\Delta\rho_{CRUST1}}^2 \end{pmatrix}, \quad (3.10c)$$

where $\sigma_{\Delta\rho D}$ and σ_D are the standard errors of $\Delta\rho D$ and D , respectively:

$$\sigma_{\Delta\rho D}^2 \approx \left(\frac{\gamma}{4\pi G} \right)^2 \sum_{n,m} \left(\frac{(2n+1)(n-1)}{(n+1)} \right)^2 \sigma_{nm}^2 + 2 \left(\frac{\gamma}{4\pi G} \right)^2 \sum_{n,m} \sum_{k,l \neq n,m} N_{nm} N_{kl} \sigma_{nmkl}, \quad (3.10d)$$

$$\sigma_{\Delta\rho_{VMM}}^2 = \sigma_{\Delta\rho D}^2 / D_o^2 + \sigma_D^2 (\Delta\rho D)^2 / D_o^4, \quad (3.10e)$$

$N_{mm} = (2n+1)(n-1)/(n+1)$, γ is normal gravity, σ_{mm}^2 and σ_{nmkl} are the potential coefficient error degree and order variances and covariances, respectively. The final least-squares solutions for the Moho depth (\hat{D}) and the density contrast ($\Delta\hat{\rho}$) are estimated by:

$$\hat{D} = D_o + d\hat{D} \text{ and } \Delta\hat{\rho} = \Delta\rho_o + d\Delta\hat{\rho}, \quad (3.10f)$$

Finally, the Moho parameters i.e. depth and density are obtained after n iterations by considering the following convergence criteria:

$$\begin{aligned} \|dD_{i+1} - dD_i\| &\leq \varepsilon_D \\ \|d\Delta\rho_{i+1} - d\Delta\rho_i\| &\leq \varepsilon_{\Delta\rho} \end{aligned} \quad (3.10g)$$

3.6 Sub-crustal stress determination

According to *Sjöberg and Bagherbandi (2017, Ch. 8)*, the relation between tectonics and mantle convection is still debated. Tectonics is relevant to the processes that control the structure and the properties of the crust. While the mantle convection is the primary engine of Earth's dynamic that controls most of the Earth's atmospheric, oceanic, mantle and outer-core system process. Therefore, the theory of mantle convection is useful and relevant in many applications such as plate velocities, gravity changes, GIA, stress in the mantle, etc. In addition, the role of plate rheology is important to understand lithospheric stress ended by mantle convection. To better understanding crustal and lithospheric deformation and seismicity, stress modeling in the lithosphere caused by mantle convection is a crucial process (*Becker and O'Connell 2001*).

The crustal stress is defined as the exerted force along the boundaries of tectonic plates in response to their movement toward each other, and it depends on the direction of motion of the plate. In geoscience, there are three different type of stresses: compression, tension and shear (*Sjöberg and Bagherbandi 2017, Ch. 8*). Using repeated observations from different types of satellite geodetic techniques e.g. GNSS (*Scherneck et al. 2010*), Very Long Baseline Interferometry (VLBI) (*Haas et al. 2002*), SLR (*Noomen et al. 1996*), and InSAR (*Hanssen 2001*), offer a great tool to define the pattern of relative plate tectonic motions and displacement (*Sjöberg and Bagherbandi 2017, Ch. 8*).

3.6.1 Static horizontal sub-crustal stress using potential components

Runcorn (1967) estimated the stress between two different Earth layers using the Navier-Stokes equation, by assuming that the upper part of the Earth consists of two layers (the outer layer i.e. the rigid crust, and the inner viscous layer i.e. the mantle), which satisfy the following conditions:

- a) The size of the upper part of the Earth is large enough so that the gravitational effect of the lower boundary can be neglected, and
- b) The shape of the upper boundary is such that it is hydrostatic equilibrium, and furthermore,
- c) The mantle viscosity coefficient is constant.

Following these conditions and using the disturbing potential of the Earth's gravity field T (*Heiskanen and Moritz 1967, p. 88*), *Runcorn (1967)* presents the stress components exerted by the mantle convection on the crust in the north-south and east-west direction as follow (*cf. Pick 1994*):

$$\sigma_x = \frac{M g}{4\pi R^2} \sum_{n=2}^{\infty} \left(\frac{R}{R-D_0} \right)^{n+3} \frac{2n+1}{n+1} \frac{\partial F_n}{\partial \theta} \quad (3.11a)$$

and

$$\sigma_y = \frac{M g}{4\pi R^2} \sum_{n=2}^{\infty} \left(\frac{R}{R-D_0} \right)^{n+3} \frac{2n+1}{n+1} \frac{\partial F_n}{\sin \theta \partial \lambda} \quad (3.11b)$$

respectively, where $F_n = T_n R / (GM)$, M is the mass of the Earth, G is the gravitational constant, R is the Earth's mean radius, g is the mean gravity at the Earth's surface, D_0 is the mean Moho depth, T_n is the Laplace disturbing potential harmonic (see Eq.(3.12)), and θ and λ are co-latitude and longitude respectively. In practice the summations in Eqs. (3.11a) and (3.11b) must be finite, say, n_{\max} . By inserting the Laplace disturbing potential harmonic:

$$T_n = \frac{GM}{R} \sum_{m=-n}^n C_{nm} Y_{nm}(P) \quad (3.12)$$

into Eqs. (3.11a) and (3.11b) the stress components become:

$$\sigma_x = \frac{Mg}{4\pi R^2} \sum_{n=2}^{n_{\max}} \left(\frac{R}{R-D_0} \right)^{n+3} \frac{2n+1}{n+1} \sum_{m=-n}^n C_{nm} Q_m(\lambda) \frac{\partial \bar{P}_{n|m}(\theta)}{\partial \theta} \quad (3.13a)$$

$$\sigma_y = \frac{Mg}{4\pi R^2} \sum_{n=2}^{n_{\max}} \left(\frac{R}{R-D_0} \right)^{n+3} \frac{2n+1}{n+1} \sum_{m=-n}^n m C_{nm} Q_{-m}(\lambda) \frac{\bar{P}_{n|m}(\theta)}{\sin \theta} \quad (3.13b)$$

where $Y_{nm} = \bar{P}_{nm}(\theta)Q_{nm}(\lambda)$, and

$$Q_m(\lambda) = \begin{cases} \cos m\lambda & m \leq 0 \\ \sin m\lambda & m > 0 \end{cases} \quad (3.14a)$$

and (Illk,1983, Z.1.44):

$$\frac{\partial \bar{P}_{n|m|}}{\partial \theta} = \frac{1}{2} [(n+|m|)(n-|m|+1)P_{n,|m|-1} - P_{n,|m|+1}] \quad (3.14b)$$

Equation (3.13b) contains a singular term $1/\sin\theta$ in the first order derivative of the Legendre polynomial. Some attempts have been succeeded to exclude this singularity, see for example *Petrovskaya and Vershkov (2006)*. Then, the magnitude (S) and direction (azimuth, α) of the stress can be expressed as:

$$S = \sqrt{\sigma_x^2 + \sigma_y^2} \quad (3.15)$$

$$\alpha = \arctan(\sigma_y/\sigma_x) \quad (3.16)$$

3.6.2 Static horizontal sub-crustal stress using gravimetric-isostatic crustal method: an alternative method

As presented and discussed in (Section 2.1 in **Paper I**), an alternative method to study horizontal stress using gravity disturbance estimated from gravimetric isostatic crustal method can be used. Where we used a known Moho depth model e.g., CRUST1.0, for predicting δg (see *Bagherbandi 2011*, Eq. 2.46b and *Eshagh and Tenzer 2015*) and then the Earth's gravitational potential (T). The obtained disturbing potential (we assumed that it is related to crust and upper mantle) will be used to estimate the sub-lithosphere horizontal stress due to the geodynamical movement e.g., mantle convection. By assuming that $\delta g^l = 0$ (see Eq. 3.1), the disturbing potential T will be obtained (see **Paper I** for more details). Then by using harmonic analysis the coefficients C_{nm} can be obtained using:

$$C_{nm} = \frac{1}{4\pi} \iint_{\sigma} T Y_{nm}(P) d\sigma \quad (3.17)$$

which will be used in Eqs. (3.13a) and (3.13b) to estimate the sub-lithosphere stress components due to the geodynamics movements caused by e.g. the mantle convection.

3.6.3 Temporal variation in sub-crustal horizontal stress using satellite gravimetry data

Long record of the satellite gravimetry data e.g. GRACE, can be used to assess the temporal stress changes. By using regression analysis introduced in (Section 2.2), the secular rate of the disturbing potential T can be also written as:

$$\dot{T} = \frac{GM}{R} \sum_{n=0}^{\infty} \left(\frac{R}{r_p} \right)^{n+1} \sum_{m=-n}^n \dot{C}_{nm} Y_{nm}(P) \quad (3.18)$$

where $\dot{(\)}$ means the derivative with respect to time and \dot{C}_{nm} can therefore be estimated by

$$\dot{C}_{nm} = \frac{1}{4\pi} \iint_{\sigma} \hat{b} Y_{nm}(P) d\sigma \quad (3.19)$$

where \hat{b} is the secular trend (unitless) of the disturbing potential using Eq. (2.12). Furthermore from equations (3.13a and 3.13b) the temporal change of the sub-lithosphere stress components becomes:

$$\dot{\sigma}_x = \frac{Mg}{4\pi R^2} \sum_{n=2}^{\infty} \left(\frac{R}{R-D_0} \right)^{n+3} \frac{2n+1}{n+1} \sum_{m=-n}^n \dot{C}_{nm} Q_m(\lambda) \frac{\partial \bar{P}_{n|m}(\theta)}{\partial \theta} \quad (3.20)$$

$$\dot{\sigma}_y = \frac{Mg}{4\pi R^2} \sum_{n=2}^{\infty} \left(\frac{R}{R-D_0} \right)^{n+3} \frac{2n+1}{n+1} \sum_{m=-n}^n m \dot{C}_{nm} Q_{-m}(\lambda) \frac{\bar{P}_{n|m}(\theta)}{\sin \theta} \quad (3.21)$$

Similarly, the change of magnitude \dot{S} is obtained by

$$\dot{S} = \sqrt{\dot{\sigma}_x^2 + \dot{\sigma}_y^2} \quad (3.22)$$

Here, it is important to emphasize that according to *Runcorn (1967)* the stress changes the gravity and isostatic equilibrium state. In addition, the time derivative of the Earth's gravity field can be used to derive the stress changes.

3.7 Numerical results

3.7.1 Paper IV: A case study in Africa

“A study on the relationship between isostatic balance and seismicity: A case study in Africa”.
Bagherbandi and Gido (In review).

The aim of this study is to highlight the relationship between the isostatic balance and seismicity, and the probable main reasons of geodynamics processes, e.g. seismic activities, by analysing the isostatic state in our study area that includes East Africa, Egypt, Congo, Sudan and Saudi Arabia, using a combined Moho model. Moreover, the sub-crustal stress and its relationship with seismicity is estimated using the gravimetric method introduced in Section 3.5 and **Paper I**. The study area is limited between the latitudes 30 N and 8 S arc-degree and the longitudes 24 E and 58 E arc-degree. The most important phenomenon that occurs in this region is the East African continental rifting, mainly caused by the horizontal extensional forces in the lithosphere. The rift goes through Ethiopia, Kenya, Tanzania and extends into Malawi (see Figure 1 in **Paper IV**). Moreover, there are a number of active volcanoes in the East African Rift Zone, such as Mount Kilimanjaro, Mount Kenya, Mount Longonot, Menengai Crater, Mount Karisimbi, Mount Nyiragongo, Mount Meru, and Mount Elgon, as well as the Crater Highlands in Tanzania. The movement of the African plates, i.e. Nubian and Somali, can lead potentially to the formation of new plate boundaries in the study area, which are the reason for such seismic activities in the form of earthquakes and volcanism. The so often-called “African Superswell” phenomena, i.e. the raise up of the mantle plume and consequently causes the rift, can also result in land uplift, and volcanism (see Figure 2 in **Paper IV**; *Watts 2001, Sect.7.2*). How isostasy and Moho parameters (depth and density contrast) explain the rift valley (cf. Figure 2 in **Paper IV**) is one of the goals of this study.

We combined the seismic and gravimetric-isostatic models using the least squares adjustment technique (Eq. 3.10a) in this study. Our results show that the combined method is better and less affected by the limitation of the seismic (sparse data) and gravimetric-isostatic models (non-isostatic effects).

Gravimetric-isostatic Moho parameters (i.e. crustal thickness and crust-mantle density contrast) were determined using an Erath gravitational model XGM2016 (*Pail et al. 2017*), which is based on more than 10 years of GRACE and other satellite gravity mission data (e.g. GOCE and SLR). The model is a combination of altimetry, satellite gravimetry and ground data. In the combined Moho model, the seismic model presented by *Baranov (2010)* has been also used. The XGM2016 model was used to

estimate the Free-air gravity disturbance (δg^f) up to degree and order 180. This resolution is sufficient for the Moho parameters modelling (regionally) according to *Tenzer et al. (2014)*. GRS80 (*Moritz 2000*) normal gravity parameters was employed to determine δg^f . CRUST1.0 model was used to determine the additive corrections presented in Eq. (3.4) according to *Bagherbandi et al. (2013)* and *Tenzer et al. (2015)*. The topographic, the bathymetry and ice corrections were computed using the Earth2014 model (Figure 3.2). We applied the sediment data using CRUST1.0 model (Figure 3.3b). Figure 3 in **Paper IV** shows the resulted maps of the free-air and Bouguer gravity disturbances (δg^{TBIS}), compensating attraction A_c (using Eq. 3.3 and assuming that Moho parameters are known), and additive corrections due to topography, bathymetry and sediments in the study area. Their values are also shown in Table 3.2. The Bouguer gravity disturbance (δg^{TBIS}) and compensating attraction A_c were used to determine the isostatic gravity disturbances (see Figure 3.6) and then to explain the relationship between the continental rift valley and isostatic state in the study area. Figure 3.6 shows large negative values under rift valley area for A_c , which is probably due to the rift valley, crust density variations and motions in the upper mantle.

Table 3.2. Free-air gravity disturbances, Bouguer gravity disturbances, additive corrections, compensation attraction, and isostatic gravity disturbances. Unit: mGal.

	Min	Mean	Max	STD
Free-air Gravity disturbances	-90	-8	119	27
Bouguer gravity disturbances	-136	179	538	171
Additive corrections	-152	187	598	185
Compensation attraction	-797	-380	344	237
Isostatic gravity disturbances	-715	-200	300	186

By applying the combined method i.e. Eq. (3.10a), the Moho parameters (depth and density contrast) are determined using the above-mentioned data. As it can be seen in Figure 3.6, the isostatic gravity disturbances are not close to zero and one can see large negative numbers. *Kaban et al. (2016)* confirmed that the isostatic anomalies are sensitive to the used isostatic model and configuration of the Moho. We know that the deep masses and dynamics of the Earth are related to the long-wavelength of the isostatic gravity disturbances (up to spherical harmonic degree 15) and medium- and short-wavelengths (regional and local parts) are characterized the density structure and isostatic disturbances the lithosphere (see more in *Bowin 2000*). Our results are based on a regional compensation model (i.e. VMM model) that shows the regional part of the isostatic gravity disturbances. This model should be taken into account, especially in Afar triple junction. By employing the Airy model strong positive

anomalies are calculated. However, the uplift of the lithosphere in Afar region is balanced largely by the mantle lithosphere and it is better to use regional compensation model that means the compensation occurs by deep masses than as in the Airy model. We observed negative isostatic gravity disturbances that are derived from the regional compensation model in Afar region, and we conclude that the positive values using the Airy model are artificial (*Kaban et al. 2016*). This result is consistent with (*Schaeffer and Lebedev 2013*), too.

Figure 4 in **Paper IV** shows the Moho geometry obtained from Baranov seismic model (*Baranov 2010*), the gravimetric-isostatic (VMM) model (Eq. 3.5), and the combined Moho model (Eq. 3.10a). Two seismic models, i.e. Baranov and CRUST1.0 models, were used as observations to estimate the combined Moho model i.e. $l_3 = D_{seismic}$ and $l_4 = \Delta\rho_{CRUST1}$ (see Eq. 3.10b).

For determining the combined Moho model, the prior value (D_o) was set to 30 and 13 km in continental and sea areas, respectively (as average values of Moho depths in the study area). The prior value ($\Delta\rho_o$) of the crust-mantle density contrast was set to 400 kg/m³ in the continental and sea regions (an average value using CRUST1.0 model). Similar to *Čadek and Martinec (1991)*, we assumed 5 and 2 km as the standard errors for the Moho depth ($D_{seismic}$) and 70 and 50 kg/m³ for $\Delta\rho_{CRUST1}$ in the continental and sea areas, respectively.

We expect that the combined model reduces the shortcomings in both seismic and VMM models. For example, by comparing the seismic and VMM models (Figures 4a and b in **Paper IV**), one can see that the Moho is deeper in Ethiopia using the VMM model (see also Figure 3.7a). This problem probably comes by the unmodelled non-isostatic effects in our gravimetric-isostatic model. The disturbing signals due to the non-isostatic effects caused by the remaining (unknown) mass-density variations in the topography, bathymetry, ice and sediment layers, which were not considered in forming the refined Bouguer disturbances (*Sjöberg and Bagherbandi 2017*). However, this problem was solved (almost) by using the combined model that provides a thinned crust (about 30 km) and low crust-mantle density contrast (about 140~200 kg/m³) in Djibouti (Afar triple junction) and also in the region between Ethiopian and Somalian plateau (see Figure 4c and Figure 7 in **Paper IV**).

Figures 5 in **Paper IV** illustrates the large correlation coefficients between the Bouguer gravity disturbances and the Moho depth in the study area. The large correlation shows that the Bouguer gravity disturbances can be used to extract the Moho depth.

The isostatic equilibrium state can be investigated by the calculated isostatic gravity disturbances (Figure 3.6). If all the masses above sea level are compensated, there is a complete equilibrium and $\delta g_I = 0$. This case is hardly possible. It is also possible that the compensating masses are larger than the topographic masses and the isostatic equilibrium state is said to be over-compensated and $\delta g_I < 0$. If only some parts of the topographic masses are compensated, then the isostatic equilibrium state is called under-compensation and $\delta g_I > 0$ (Heiskanen and Vening Meinesz 1958; Bagherbandi 2011). According to Figure 3.6, the over-compensation state is dominant and generally the isostatic gravity disturbances (δg_I) are negative in the study area. Isostatic gravity disturbance varies between -715 and 300 mGal, with a mean of -200 mGal and a standard deviation of 186 mGal (see Table 3.2).

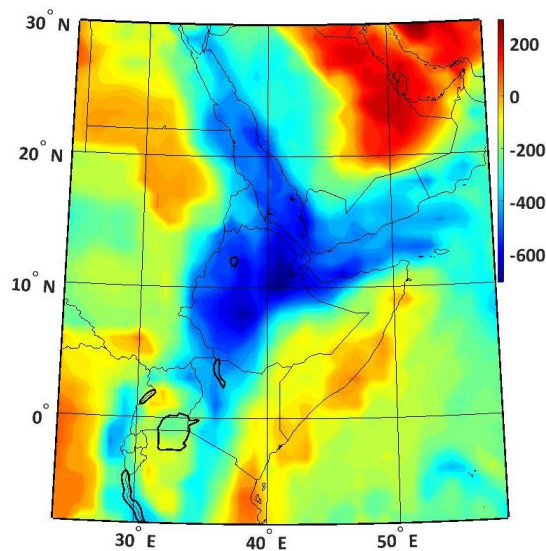


Figure 3.6. Isostatic gravity disturbances using the VMM model. Unit: mGal.

The topographic masses are compensating regionally in the study area, especially, along with the plate boundaries as the crust-mantle density contrasts become smaller (see Figure 3.7b) in the thinned crust areas, starts from Djibouti (Afar triple junction) and continues between the Ethiopian and Somalian Plateau. Furthermore, Ethiopian and Kenya domes are a good examples as the density contrasts become smaller as they rise higher (because of superplume) and isostatic equilibrium is formed by the density differences (Bechtel et al. 1987). The crust-mantle density contrast varies between 520 and 90 kg/m³, with a mean of 335 kg/m³ and a standard deviation of 77 kg/m³ in the study area. There is correlation between the crust-mantle density contrast and isostatic gravity disturbances (Figures 3.6 and 3.7b). The existence of low crust-mantle density contrast and large negative isostatic gravity disturbances, near the triple junction plate tectonics (Afar triple junction), all confirm the state of over-compensation.

The reasons for the presence of the low crust-mantle densities in the rift valley areas (Figure 3.7b) may be attributed to the existence of high mantle conductivities, according to geophysical models and observations beneath the rift valley and the dome areas, which leads to high heat-flow near to the rift valley areas, and the flow helps asthenospheric plume to enter the lithosphere possibly to the lower crust like oceanic ridges. On the other hand, the tectonic plates are moving apart, due to the extension-related or plume-related phenomena, in the rift valley region, and consequently the crustal density will be close to the mantle density. This means that the crust is weak in this region. Moreover, it can be seen in Figure 3.7b that the density structure of the lithosphere is closely related to the earthquake activities and volcanic distribution. The high seismic activity and low crust-mantle density contrast in the vicinity of the tectonic boundaries can be related to the low strength of the crust and deformation due to high temperatures. Generally, this can be observed in regions with negative isostatic gravity disturbances. The most earthquakes are of low and medium magnitudes at shallow depths and are located in the rift valley, which is characterized by the low crust-mantle density contrast (about 100-200 kg/m³). This can be related to weak crust around Afar triple junction. The dark red regions (high density contrast) shows likely strong crust layer and are characterized by low seismic activity. Therefore, there is a correlation between the isostatic gravity disturbances, crust-mantle density contrast and earthquake activities.

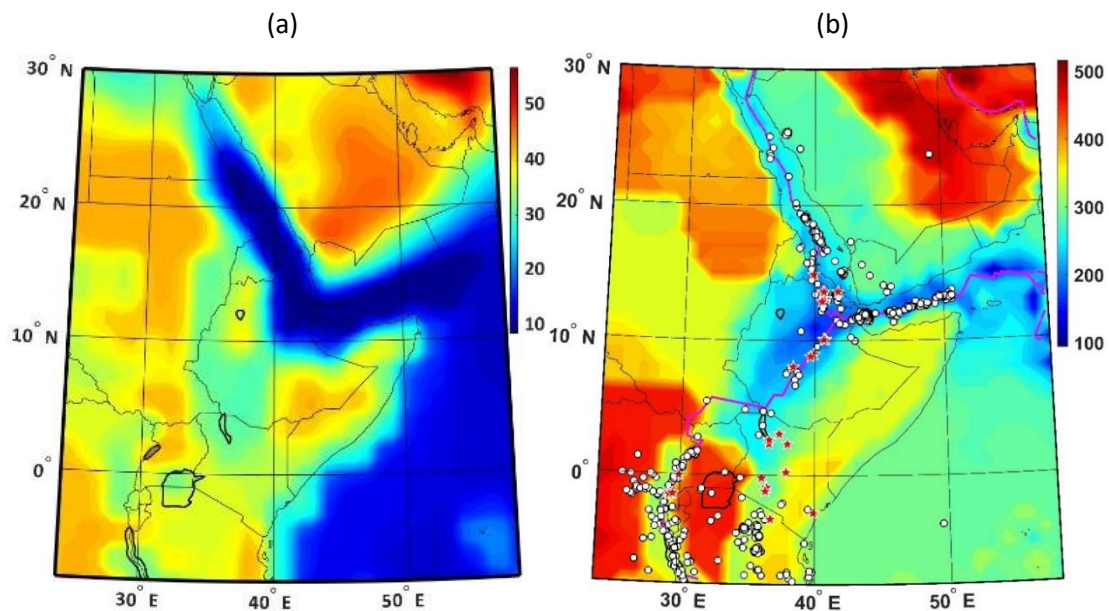


Figure 3.7. a) Crustal thickness using combination of the VMM, CRUST1 and Baranov models (Unit: km), and b) Crust-mantle density contrast determined using combined model (red stars show volcanic areas, white color circles denote on the location of earthquakes larger than 4 Richter magnitude scale between 2008-2018 (no scaled), and solid magenta line shows the main plate boundaries). Unit: kg/m³.

Figure 3.7b shows the distribution of earthquakes and volcanic areas in the study region. The correlation between the large negative isostatic gravity disturbances and earthquake activities is also shown by observed data and theoretically (see also Figures 3.6 and 3.7 b, and *Artemjev et al. (1972)*). Over-compensation state leads to large shear stresses in this region. Therefore, gravimetric methods can be considered for studies of earthquake activities. Following the same method, presented in **Paper I**, and Sect. 3.6, the sub-crustal stresses was estimated (Figure 3.8). The results show that when the tectonic plates are diverging (e.g. Ethiopia and Somalia), the sub-crustal stress increases and consequently the ground deformation (volcano deformation) and earthquake activities is also increased. The arrows in the figure show velocity/gradients vectors of the sub-crustal stress and dark red arrows illustrate larger gradients. The same state happens for the Eurasian and Arabian plates when the tectonic plates are converging and it results in compressive stress.

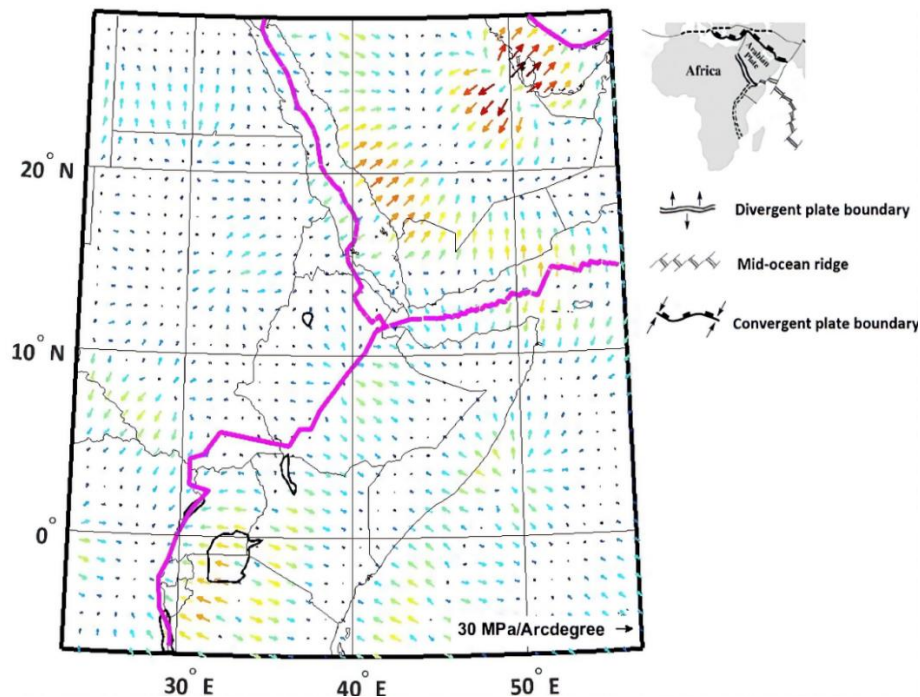


Figure 3.8. Gravimetric sub-crustal stress obtained from modified Runcorn method (*Runcorn 1967*), and solid magenta line shows the main plate boundaries. The arrows in the figure show velocity/gradients vectors of the sub-crustal stress and dark red arrows illustrate larger gradients.

The obtained results showed that isostatic equilibrium and compensation states are closely correlated to the seismicity patterns in East African Rift. The results reveal low-density contrasts and thin crust near the triple junction plate tectonics in the Afar triple junction. The heat transfer from the mantle, mantle flow and stretching (thinning of

the crust) due to tectonic plate motions are the main reasons for the low-density contrast in this region. One can clearly see a correlation between the crustal depth, isostatic anomaly, density contrast, and earthquake activities, as the results showed that the Moho parameters or structure of the lithosphere is closely related to the earthquake distribution. Although, we know that not all earthquakes can attribute to the low-density contrasts. The areas with high seismic activity, in Ethiopia and Somalia, are related to the low strength of the crust and deformation due to the low-density contrast and high temperatures.

3.7.2 Paper I: A case study in Fennoscandia

“A Gravimetric method to determine horizontal stress field due to flow in the mantle in Fennoscandia” Gido et al. (2019).

The purpose in this study is to investigate and derive sub-lithosphere horizontal stress in the Earth’s mantle and its secular rate, due to the dominating deformation of the crust in Fennoscandia e.g., by the ongoing mantle convection and GIA, using gravimetric method.

The static sub-lithosphere horizontal stresses were estimated using the Runcorn traditional approach (Section 3.6.1) and a gravimetric-isostatic model (Section 3.6.2) by applying Eq. (3.17) in Eqs. (3.13a) and (3.13b). For this purpose the DTM2006 Earth elevation model (*Pavlis et al. 2007*) was used, and the Earth’s crustal thickness and Moho density contrast (obtained from CRUST1.0 model) as well. Using regression analysis (Section 2.2), the CSR GRACE data were utilized during the years of 2003 to 2016 for estimating the rate of the gravity field changes, which used to estimate the secular rate of the sub-lithosphere horizontal stress (Section 3.6.3).

According to *Sjöberg (1983)* the gravity field change in Fennoscandia reflects some geodynamical phenomena like the GIA and mantle convection. However, this gravity signal is likely mixed with other effects like plate tectonics, etc. Therefore, we will use certain spherical harmonic degrees of the disturbing potential in order to filter the gravity signals related to the lower mantle and core masses. *Bowin (2000)* model shows that the spherical harmonic degrees between 5 and 40 belong to about 100 to 1600 km depth, where asthenosphere and mantle are located, (see Fig. 5 in **Paper I**). Therefore, we will use this harmonic window (i.e. the degrees 5 to 40) to determine the horizontal stress in this study (Section 3.1 in **Paper I**). Generally, there are different geodynamical phenomena those can be the reasons for the current horizontal stress in the study region such as mantle convection, horizontal and vertical land motion due to plate tectonics and the GIA, and it is very complicated to separate and distinguish the gravity signals due to mantle convection and land motion. Therefore, to prove the outcomes of Bowin’s model, a correlation analysis using land uplift model

NKG2005LU (Ågren and Svensson 2007) was performed. The result shows that the spherical harmonic degrees between 5 to 40 reveal highest correlation (0.87) between land uplift and the obtained horizontal stress, which support the use of degrees 5 to 40 to determine the horizontal stress in this study.

Figure 3.9a shows the estimated static (absolute) sub-lithosphere stress (Section 3.6.2) in the Fennoscandian Shield in GPS stations (*cf. Kierulf et al. 2014*) those have been used for calculating the land uplift model in Fennoscandia. Where we can compare the estimated stresses with the geometry of the land uplift. Table 3.3, shows the statistic of the sub-lithospheric stress components and its total magnitude. The result shows that the stress has its maximum value close to the centre of the land uplift dome and decreases around the ice margin (see Figure 3.9a).

Table 3.3. Horizontal stress due to mantle convection. Unit: MPa

	Min	Max	Mean	STD
σ_x	-16	8	-6	6
σ_y	-27	1.6	-15	7
$S = \sqrt{\sigma_x^2 + \sigma_y^2}$	0.2	29	17	7

Temporal changes in the sub-lithospheric horizontal stress were estimated using the GRACE monthly data (see Section 3.6.3). The results show that the GPS stations outside the uplift dome experience more horizontal stress changes than the stations inside the dome (Figure 3.9b). To see how the estimated stresses agree with the seismic activities in Fennoscandia. The matter was further investigated by comparing the estimated stresses with the geographical distribution of 10 years of seismic activities in Fennoscandia (Figure 8c, **Paper I**) which showed a significant correlation between the secular rate of the estimated stress and seismic activities in Fennoscandia.

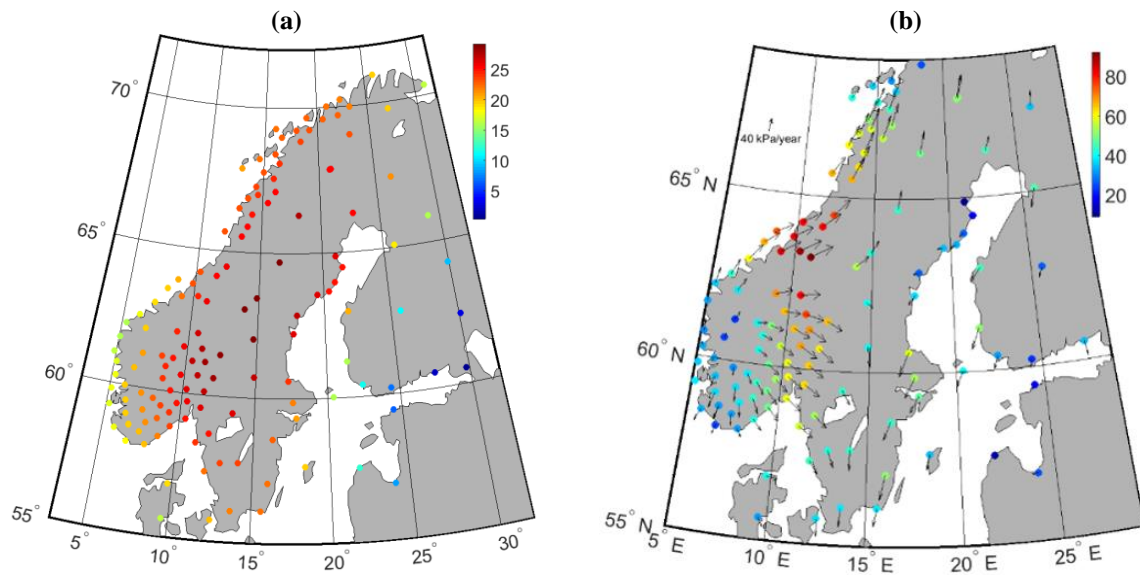


Figure 3.9. a) Absolute sub-crustal horizontal stress due to mantle convection (tectonics), Unit: MPa. b) Temporal variation of sub-crustal horizontal stress using CSR GRACE data for the period of 2003 to 2016 (secular rate of the horizontal stress are shown as color circles (Unit: kPa/year) and direction of the horizontal stress changes with black arrows, Unit: kPa /year).

Therefore, according to the estimated results (the geometrical similarities between the horizontal velocities in Figure 3, **Paper I**, and the estimated stresses in figure 3.9), the GIA and the tectonics could be the potential sources of the stress field that affected Fennoscandia Shield, where the flow in the mantle and the flexure of the lithosphere support vertical and horizontal stresses field of the tectonic plate.

Chapter 4

Earth's surface deformation measurement using InSAR

4.1 Introduction

Monitoring surface deformation is important for understanding, analyzing, and modeling of natural and anthropogenic processes. The outcomes may also increase safety and reduce damages for buildings and infrastructures by evaluating potential risks of surface deformations. Space geodesy is widely used to study and investigate a variety of natural processes such as earthquakes, volcanic activities, and landslides. Among the geodetic techniques, Synthetic Aperture Radar Interferometry (InSAR) is an important one, that could be used for many applications, such as glacier movements, active tectonics and also in ground surface deformation that related to mass changes e.g. groundwater depletion, and sub-surface geology types (*Zhou et al. 2009*). Thus, the radar satellite data are very suitable for the task of surface deformation monitoring.

Synthetic Aperture Radar (SAR) is an active remote sensing system that has a day and night operational and cloud penetration capability i.e. independent of illumination by the sun, and not suffer from cloud covers. The result of radar data processing, normally shows the location and magnitude of the deformation of the study area in a period of time. These findings and results can be considered as a starting point for modeling and evaluation of geodynamical processes and natural hazards. With the availability of a vast amount of globally covering SAR data from e.g. ERS, Envisat, TerraSAR, and Sentinel-1 sensors, a significant progress has been achieved with a wide range of applications in geoscience (*Massonnet and Feigl 1998; Hooper et al. 2007; Crosetto et al. 2015; Castellazzi et al. 2018; Roccheggiani et al. 2019*).

Persistent (or Permanent) Scatterer Interferometry (PSI) is a powerful remote sensing technique that is capable to estimate surface deformation rates with very high accuracy. Since the introduction of the method by *Ferretti et al. (2000 and 2001)* numerous research and studies have been carried out e.g. *Kampes (2006); Hooper et al. (2007); Gernhardt (2011); van Leijen (2014); Fryksten and Nilfouroushan (2019)*. PSI is a radar-based technique that belongs to the group of differential Interferometry

Synthetic Aperture Radar (DInSAR), which provides a unique method for detection and mapping of surface deformation over large temporal and spatial resolution with cm accuracy (*Gabriel et al. 1989*). The techniques exploit the information contained in the radar phase of at least two SAR images acquired over the same area at different times (single-pass or repeat-pass), which used to form an interferometric pair. The method has proven its potential for high precision deformation monitoring using different types of radar images e.g. ENVISAT, Sentinel, and TerraSAR-X. The so-called, Persistent Scatterer (PS) is a certain sign in the radar images that shows a long-term coherence point-like scattering behaviour, and hence is suitable for precise motion analysis by interferometry. These points are estimated within the PSI, and capable to estimate, for example, a subsidence rate in the order of mm/year.

4.2 Synthetic Aperture Radar (SAR)

The Radar (RADio Detection And Ranging) is an active side looking remote sensing system, that emits and receives reflected pulses from the ground at certain microwave wavelengths, and then record the returned amplitude and phase signal to produce a rough two-dimensional image for the ground (*Bürgmann et al. 2000*). In general, the phase value carries information about the distance from the sensor to the reflected target, while the amplitude represents the reflectivity of the surface. Bright areas in a generated radar image represent a high amplitude of the reflected wave energy, which depends on the geometry and roughness and the dielectric characteristic of the surface material. The signal travel time is close to the speed of light, with a slight deviation due to the refraction properties of the atmosphere. In principle, any signal frequency may be used, but the microwaves are the most common (*Skolnik 1990*), especially the L-band (15-30 cm), C-band (3.8-7.5 cm), and the X-band (2.4-3.8) which are favored for the SAR satellite remote sensing. Owing use of the phase measurement to quantify distances, the wavelength of the system is of great importance. Generally, longer wavelengths have some penetration to the vegetation, ice, and dry soils sensitivity. For example, it is reported that use of L-band provided (for instance) by the ALOS-1/2 Japanese satellites, is sensitive for monitoring of surface height and the terrain covered by vegetation (*Wei and Sandwell 2010*). Phase measurements from longer wavelengths tend to be less sensitive to small surface changes over time. Moreover, longer wavelengths are less sensitive to deformation per pixel than shorter wavelengths (*Wempen and McCarter 2017*). Figure 4.1 shows the acquisition geometry of the system, where the flight direction of the satellite is denoted as the azimuth, the side looking direction is defined as (slant) range.

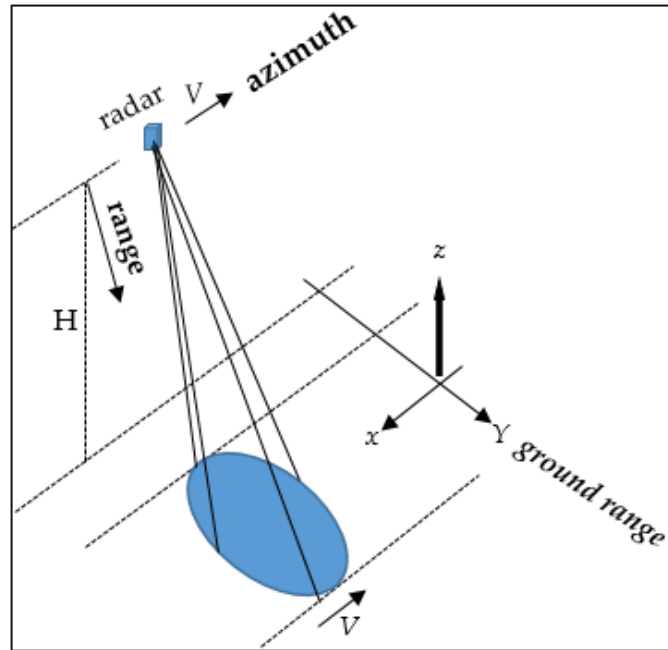


Figure 4.1. Acquisition geometry of SAR system. H and V are the flying height and velocity. The side looking system illuminates a certain area on the ground (blue part).

Synthetic Aperture Radar (SAR) combines signal processing techniques with satellite orbit information to produce a much-higher-resolution (tens of meters) radar image (Bürgmann *et al.* 2000). SAR processing largely improves the resolution of point targets in both the cross-track (range) e.g. by using radar signal of high bandwidth, and along-track (azimuth) direction e.g. relies on the synthetic aperture provided by a moving antenna (Elachi 1988, Curlander and McDonough 1991). There have been many Satellite missions with different characteristics, for example, orbital parameters, repeat cycles and resolution. Table 4.1 lists these characteristics for sentinel-1 A and B.

Table 4.1. Specifications of Sentinel-1 satellite missions.

Satellite mission	Launch	Repeat cycle	Band	Modes and Swath widths	Spatial resolution (azimuth × range)	Incidence angle	Orbital inclination
Sentinel-1A	03 April 2014	175 orbits in 12 days	C-band	Strip Map Mode: 80 km	5 × 5 m	18.3° – 46.8°	98.18°
				Interferometric Wide Swath: 250 km	5 × 20 m		
Extra-Wide Swath Mode: 410 km	20 × 40 m						
Wave-Mode: 20 km × 20 km	5 × 5 m						
Sentinel-1B	25 April 2016						

4.3 SAR Interferometry (InSAR)

SAR Interferometry is the method that employs at least two complex SAR images covering the same ground pixel, to derive more information about the target, i.e. to reveal information about the third dimension (elevation) than in a single SAR image, by exploiting the phase of the SAR signal. To provide this additional information, at least one image parameter (i.e. from the two images) must be different compared to the second one in terms of e.g. acquisition time, flight path, and wavelength (*Bamler and Hartl 1998*). The two coherent SAR images used to form an interferogram can be acquired using single-pass SAR interferometry technique, where the same SAR system (space platform) uses two antennas to emit and receive the signal at the single pass over the area perpendicularly to the flight direction (Azimuth), or by the repeat-pass interferometry i.e. from different passes of the same SAR antenna and at a different time (*Massonnet and Feigl 1998*).

InSAR uses the phase information in the two SAR images to measure the phase difference between each pair of corresponding image points, consequently producing an interferogram. A combination of phases from two images or more, after precisely aligned to a fraction of a pixel width (i.e. co-registration process) can allow for interferogram image generation whose phases are closely correlated to the terrain topography of Earth ground, which could be utilized to monitor displacement trends. Therefore, if the Earth's surface moved toward or away from the radar sensor between the two imaging acquisition passes, the resulted phase changes can be measured with a precision corresponding to millimeter-level displacements. A fringe is a line of equal phase in the interferogram that can be counted from a reference point where the surface deformation is supposed to be zero. One fringe in an interferogram is corresponded to the displacement of half the wavelength in the ground deformation along the line of sight (LOS) direction (*Gabriel et al. 1989*).

The formation of the interferogram is largely affected by many factors such as the stability of ground pixel and the local slope of the terrain which should be small, the different acquisition geometry, the spatial separation of the two antenna position (baseline), in addition, the direction of observation, orbit configuration, and the processing procedure should be exactly the same (*see Massonnet and Feigl 1998*).

4.4 Differential SAR Interferometry (DInSAR)

Any whole ground pixel displacement along the LOS direction between the radar and the target would be translated directly as a phase shift with respect to the rest of the image. The displacement will appear as a complete one fringe if the movement in the LOS direction reaches half its wavelength.

Differential SAR Interferometry (DInSAR) exploits the phase information contained in at least two complex SAR images acquired at different times over the same area, which are used to form an interferometric pair.

By considering P as a single-pixel footprint on the ground (Figure 4.2), measuring a phase φ_M , from a satellite position M is given by:

$$\varphi_M = \frac{4\pi d_{MP}}{\lambda} + \varphi_{M-SC} \quad (4.1a)$$

where d_{MP} is the distance between sensor M and pixel P , λ is the radar wavelength, φ_{M-SC} is the phase shift. Acquiring second images from position S over the same pixel P will result in:

$$\varphi_S = \frac{4\pi d_{SP}}{\lambda} + \varphi_{S-SC} \quad (4.1b)$$

where d_{SP} is distance between sensor S and pixel P . Consequently, the phase shift is obtained by subtracting Eqs. (4.1a) and (4.1b) by:

$$\Delta\varphi_{\text{int}} = \varphi_S - \varphi_M = 4\pi \frac{d_{SP} - d_{MP}}{\lambda} + \varphi_{S-SC} - \varphi_{M-SC} \quad (4.2)$$

where $\Delta\varphi_{\text{int}}$ is the interferometric phase related to the displacement $d_{SP} - d_{MP}$.

In the case of DInSAR deformation i.e. displacement of point P to P' in Figure 4.2 yields:

$$\varphi_S = \frac{4\pi d_{SP'}}{\lambda} + \varphi_{S-SC} \quad (4.3a)$$

which reads an interferometric phase ($\Delta\varphi_{\text{int}}$) as:

$$\Delta\varphi_{\text{int}} = \varphi_S - \varphi_M = 4\pi \frac{d_{SP'} - d_{MP}}{\lambda} + \varphi_{S-SC} - \varphi_{M-SC} \quad (4.3b)$$

By adding and subtracting $\frac{4\pi d_{SP}}{\lambda}$ Eq. (4.3b) can be written:

$$\Delta\varphi_{\text{int}} = \varphi_S - \varphi_M = 4\pi \frac{d_{SP} - d_{MP}}{\lambda} + 4\pi \frac{d_{SP}}{\lambda} + \varphi_{S-SC} - \varphi_{M-SC} \quad (4.4)$$

where the first term denotes the topographic phase components that include the so-called reference ellipsoidal phase components. The second term is the displacement phase components in the LOS direction $\Delta\varphi_{\text{Disp}}$ (related to the LOS displacement d in Figure 4.2).

If a DEM of the imaged scene is available, one can assume that the last two terms in Eq.(4.4) are canceled out, then the topographic term (i.e the first term) $\Delta\varphi_{\text{Top}}$ can be simulated ($\Delta\varphi_{\text{Top-simu}}$) and subtracted from $\Delta\varphi_{\text{int}}$ (InSAR DEM generation) which result in the so-called DInSAR phase components $\Delta\varphi_{\text{D-int}}$ that contains the flat-earth phase components:

$$\Delta\varphi_{\text{D-int}} = \Delta\varphi_{\text{int}} - \Delta\varphi_{\text{Top-simu}} = \Delta\varphi_{\text{Disp}} \quad (4.5)$$

According to *Crosetto et al. (2016)*, Eq.(4.5) represents a simplified DInSAR observation equation. A comprehensive one may read as:

$$\Delta\varphi_{\text{D-int}} = \Delta\varphi_{\text{Disp}} + \Delta\varphi_{\text{Top-res}} + \Delta\varphi_{\text{atm-S}} - \Delta\varphi_{\text{atm-M}} + \Delta\varphi_{\text{orb-S}} - \Delta\varphi_{\text{orb-M}} + \Delta\varphi_{\text{noise}} + 2\pi n \quad (4.6)$$

where $\Delta\varphi_{\text{Top-res}}$ represents the residual topographic error components, $\Delta\varphi_{\text{atm}}$ is the atmospheric phase components at an acquisition time of each image, and it can be reduced by applying stacking technique (*Hanssen 2001*), $\Delta\varphi_{\text{orb}}$ is the orbital error phase components of each image, and it can be estimated using precise orbits (*Closa 1998; Scharroo and Visser 1998*), $\Delta\varphi_{\text{noise}}$ is the phase noise which can be minimized by filtering and multi-look technique in order to reduced (*Massonnet and Feigl 1998; Goldstein and Werner 1998*). The last term of Eq. (4.6) represent the general 2π ambiguity (integer value n) is a result of errors in the phase unwrapping process, which is necessary to solve for this ambiguity i.e. the DInSAR phases are bounded in the range $(-\pi, \pi)$. Numerous studies concerning the unwrapping issue have been performed e.g. *Bamler and Hartl (1998); Costantini (1998)* and *Balzter (2001)*.

The goal of any DInSAR technique is to estimate the displacement phase components $\Delta\varphi_{\text{Disp}}$ from the $\Delta\varphi_{\text{D-int}}$, which requires its separation from the other components in Eq. (4.6). Analyzing pixels characterized by small noises $\Delta\varphi_{\text{noise}}$ is an essential condition for such separation. Those pixels are related to the type of reflectors e.g. constant strong reflecting object over time (Permanent Scatterer, PS). The major limitation of the

DInSAR method includes the temporal and geometrical decorrelation that influence the noise phase components (Hanssen 2001), the phase unwrapping (i.e. estimating n) (Ghiglia and Pritt 1998), and the atmospheric components (Zebker et al. 1997).

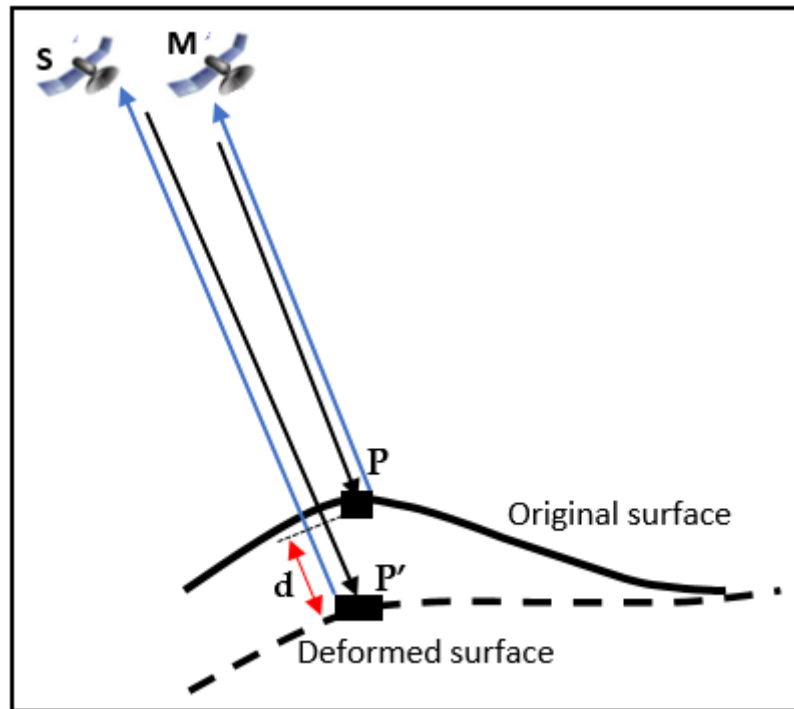


Figure 4.2. Principle of DInSAR deformation measurement. M denotes for image acquired at time (t_1) for ground target P (before deformation), S denotes for image acquired at time (t_2) for target P' (target P after deformation). d is the change in the measured range due to surface deformation.

4.5 Persistent Scatterer Interferometry (PSI) technique

The DInSAR method is mostly used when measuring large deformations induced for instance by earthquakes or volcano activities. For small deformation, the method has considerable limitations, where the most important one is the atmospheric phase components $\Delta\varphi_{atm}$ (mainly of tropospheric origin). In addition, the temporal and geometrical decorrelation limits the operational usage of InSAR to a short baseline in time and space. Therefore, by applying the so-called permanent scatterers interferometry (PSI) the above limits would be overcome (Ferretti et al. 2000 and 2001). The main outcomes of the PSI analysis include the deformation time series and velocity estimated over the analyzed area.

PSI exploits a whole stack of SAR images (typically consist of tens of datasets) acquired over the same area, and appropriate data processing and analysis procedures to separate displacement phase from the other phase components (Crosetto et al. 2015).

Form this stack, and by considering baseline in time and space, one single master acquisition should be selected to ensure high coherence in all interferograms. Furthermore, to reduce temporal and geometrical de-correlation, the estimation is carried out on a reduced set of pixels. The temporal sampling of the SAR images should be regular to some degree (i.e. by avoiding very long gaps). Prior to PS processing, a DEM for the covered area is needed for the removal of the topographic phase terms. The DEM can either be generated from the data using one suitable interferogram or from an external data source e.g. Shuttle Radar Topography Mission (SRTM). According to *Ferretti et al. (2001)*, a DEM with an accuracy of about 20 m is sufficient for mm level of accuracy.

The Permanent Scatters (PS) are the strong reflecting objects that are dominant in a pixel. Stable pixel selection depended on the use of amplitude dispersion index, *Ferretti et al. (2001)*, as follow:

$$D_A = \frac{\sigma_A}{m_A}, \quad (4.7)$$

where σ_A and m_A are the standard deviations and the mean of the amplitude, respectively. Therefore, a pixel with high reflection has a low D_A . The amplitude stability index in the used software in this study is defined as $1 - D_A$.

For every interferogram, the atmospheric phase components is estimated, and the interpolated map for the whole covered area is called Atmospheric Phase Screen (APS). According to *Colesanti et al. (2003)*, at least 25 images are needed, in addition to a PS density of about 5-10 PS/ km², for a proper estimation of these effects. Hence, the larger the number of available images the better the quality of the PSI displacement velocity and time-series estimation (*Crosetto et al. 2016*). In addition, introducing of the deformation model has to be selected prior to velocity estimation, e.g. a linear function of time, seasonal or other non-linear motion can be used (*Ferretti et al. 2000; Colesanti et al. 2003*). For this study, a linear model was used (i.e. in **Papers III and V**).

The PSI method is applicable in many areas, such as disaster monitoring and risk assessment that caused due to landslides and volcanic eruptions, earthquakes, ice sheet motion and glacier flow, and ground subsidence due to sub-surface clay deposits, mass depletion, and artificial fill (*cf. Wang et al. 2010; Gernhardt 2011; Fryksten and Nilfouroushan 2019; Foroughnia et al. 2019 and Papers III and V*) or oil and water depletion (*Galloway and Hoffmann 2007*). The capability to sample deformation phenomena over time is subject to the availability of the data over the study area, which in turn depends on the characteristic of the satellite (e.g. revisiting time, wavelength, etc.).

4.5.1 Case studies

In this section, two case studies are presented, using the freely available C-band Sentinel-1 data, and the PSI technique integrated by some in situ available data to study on land subsidence related to oil depletion and sub-surface geology type. For data processing, SARPROZ software (Perissin and Wang 2011; Perissin et al. 2011) was used. This software has been successfully used in many studies e.g. Colesanti et al. (2003); Parizzi et al. (2005); Perissin et al. (2006); Wang et al. (2010); Mullissa et al. (2018); Foroughnia et al. (2019); and Azadnejad et al. (2019).

Paper III: *"Satellite monitoring of mass changes and ground subsidence in Sudan's oil fields using GRACE and Sentinel-1 data"*, Gido et al. (2020).

This study is a complementary part of that presented in section 2.4.2, where the GRACE and InSAR data integrated with available oil production were utilized to study on mass changes and the associated ground subsidence related to oil extraction in Sudan's oil fields. In this section, the rates of land subsidence due to the oil extraction in different oil fields using Sentinel-1 SAR data and the PSI technique were computed. For this purpose, a freely available C-band Sentinel-1 A and B data from European Space Agency (ESA) were used to detect and quantify ground surface deformation related to the groundwater and oil level change for nine oil fields in the Muglad Basin, Sudan (Figure 4.3). Single Look Complex (SLC) images are co-registered to a single master. Then, the SRTM 3-arc second DEM, and the precise orbits for each image were used to remove the topographic and flat earth components respectively. Reference points (R) (e.g. Figures 7 and S6 in **Paper III**) were chosen among the selected Persistent Scatter Candidates (PSCs), which are relatively unaffected by deformation.

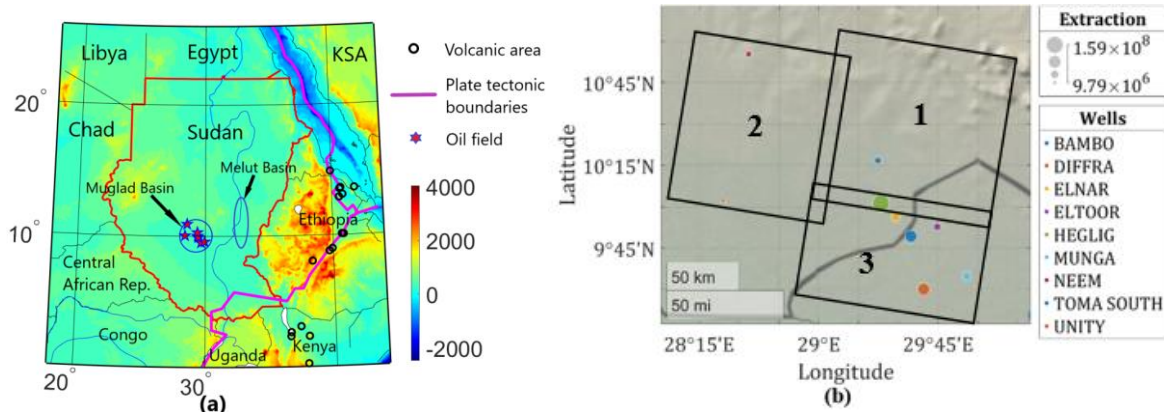


Figure 4.3. a) General map showing digital elevation of the region (Unit: m), the Basins and the study area in oil fields concessions, and b) the location of the nine oil fields in the study area and their total extraction between Jan 2003 and Sep 2012 in m³. The footprint of the three descending Sentinel-1 data sets over the nine oil fields are shown by rectangles, covering the period between November 2015 and April 2019.

The availability of the proper SAR satellite data over given region and revisiting time affects the capability to estimate deformation phenomena over time (*Ferretti 2007*). Despite the suitability of L-band images for vegetated areas in terms of penetration depths, there were not enough free L-band images that could cover the study region for such PSI analysis. As such, only Sentinel-1 data was used for this study. Three Sentinel-1 A and B data sets consisting of 30, 30, and 32 images on descending geometries covering period between Nov 2015 and April 2019, were used (see Table 4.2) to detect ground subsidence associated to oil extraction in nine oil fields using PSI method. As can be seen in the graph (Figure S1, **Paper III**), there is a lack of data during periods of 23 Jan 2016 and 21 July 2016 (6 months) for the first data set, in addition to some sparse periods (2-3 months) between the acquisitions of the three data sets despite the short revisit time of Sentinel-1 sensors which is 6-12 days.

Table 4.2. Details of the Sentinel-1 A and B datasets used for the PSI time series analysis and their properties in the oil fields in Sudan.

Data info	First set	Second set	Third set
Number of scenes	30	30	32
Acquisition period	Jan 2016-March 2019	Oct 2016-April 2019	Nov 2015-June 2018
Relative orbit	94	167	94
Acquisition track	descending	descending	descending
Acquisition mode	Interferometry Wide swath (IW)		
Product type	Single Look Complex (SLC)		
Polarization	VV		

For data processing, the first data set (including 30 images) was used to analyze Heglig and Bamboo's oil fields (see Figure 1b, **Paper III**), where 0.80 and 0.70 amplitude stability indexes were utilized for the PSCs and PS selection, respectively, and temporal coherence of 0.60 was used for masking purposes. The second set of data (including 30 images), was used to analyze Diffra (West of the field) and Neem (North of the field) fields (see Figure 1b, **Paper III**) where 0.85 and 0.70 amplitude stability indexes and 0.70 temporal coherence were utilized for Diffra's PSCs and PS selection and masking, respectively. Then 0.75 was chosen as an amplitude stability index and temporal coherence mask for the Neem field. The third set of data, including 32 images, was used to analyze Unity, Munga, Eltoor, Toma South, and Elnar's oil fields (will be referred to as Unity-area), which lies in the South part of the oil fields. The 0.76 and 0.70 amplitude stability indexes and 0.65 temporal coherence were utilized for the PSCs and PS selection and for masking respectively. Using the mentioned processing criteria, the LOS displacement rates at the selected PS points in Heglig and Bamboo (Figure 7 in **Paper III**), Neem (Figure S6 in **Paper III**), Diffra (Figure 8 in **Paper III**) and the Unity-area fields (Figure S7b in **Paper III**), were computed relative to their reference PS points. Figure 4.4 shows the cumulative displacement in (mm) of some selected PSI points relative to the reference point (H-124) in Heglig and Bamboo oil fields.

Comparison of the subsidence rates for different oil fields (Table 5 in **Paper III**), shows clearly that the Heglig oil field is the most deformed one with an accumulative displacement of about -77.6 mm during a three year period. Its higher production rate may be the reason for such a large subsidence, in addition to the dense PS points which allow for closer inspection (density of points is due to the existing of infrastructure and building in the area). Moreover, and according to *Castellazzi et al. (2016)*, InSAR applications to groundwater depletion are limited to reservoir systems sensitive to measurable deformation (clays and silts), which is the case in the study area.

According to the study, the results show a notable subsidence rate in the area ranged between -24.47 ± 0.85 mm/year and -6 ± 0.88 mm/year, which corresponds to -77.6 mm and -15.4 mm subsidence during the observation periods. This surface subsidence can be assigned to the pore pressure drop due to the vertical compaction of the reservoir (i.e. oil depletion). By integrating this result with the obtained one of the GRACE, GRACE and InSAR data can be consider as a complementary data for monitoring water and oil reservoir, despite their different resolution and application (*Castellazzi et al. 2016*).

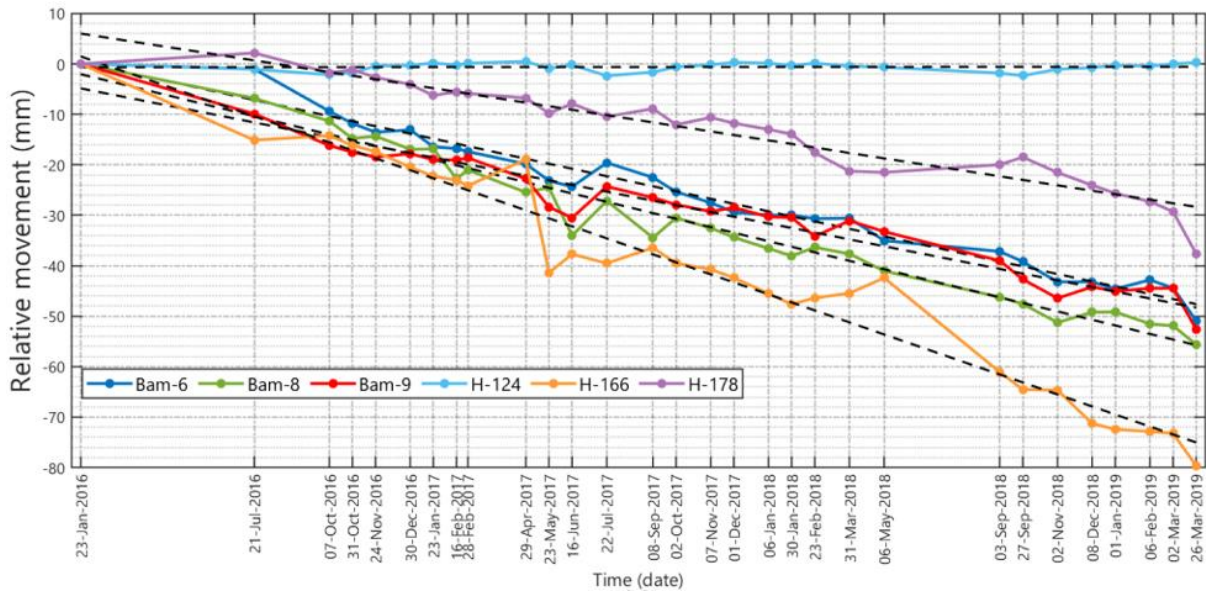


Figure 4.4. Cumulative displacement in (mm) of the selected PSI points relative to reference point (H-124) in Heglig and Bamboo oil fields.

Paper V: “Localized subsidence zones in Gävle City detected by Sentinel-1 PSI and Leveling data”, Gido et al., (Accepted)

The integration of the periodic radar satellite data with the local in situ data (e.g. geology and precise leveling data) would be of great importance for the geo-hazard mapping. In this study, the ground surface deformation of Gävle city in Sweden is investigated using the PSI technique as well as analyzing the historical leveling data. The PSI technique was used to map the location of risk zones and their ongoing subsidence rates. Two ascending and descending Sentinel-1 data sets, collected between Jan 2015 and May 2020, covering the Gävle city were processed and analysed using SARPROZ software. In addition, a long record of leveling data set, covering the period from 1974 to 2019, was used to detect the rate of subsidence in some locations which were not reported before. Furthermore, correlation analysis was performed between the PSI results and the available geological maps for the study area.

Gävle city is one of the old coastal growing cities in Sweden that crosses by Gävleån River, which formed a large delta at the outlet in the Gulf of Gävle. The sub-surface geology of the city includes artificial fill areas that have been used for urban development of the city. According to the Department of the Environment, Transport, and the Regions, and Environment Agency in the UK (DETR/EA, 1998) “the fill material at any site is commonly an admixture of organic, chemical and inert material which can lead to serious problems in the built environment”. Thus, the ongoing and expected development of the city according to the municipality of Gävle (www.Gävle.se), along the coastal

line, within the formed delta and the artificial fill area is prone to subsidence hazard. The availability of long leveling observation records that last for about 45 years in monitoring the stability of some locations in the city, in addition to other information would help for such mapping for the city.

Two data sets consisting of 41 and 50 Single Look Complex (SLC) images on ascending and descending geometries were processed and analyzed over the study area covering periods from Jan 2015 to May 2020 and from June 2015 to May 2020, respectively (see Table 4.3 below, and Figure 7 in Paper V). The temporal resolution for the acquired images was about one month, with some exceptions due to the unavailability of some images with certain characteristics or some images were removed due to the winter season which may reduce image coherence.

Table 4.3. Details of the Sentinel-1 A and B datasets used for the PSI time series analysis and their properties in Gävle city.

Data info	Ascending	Descending
Number of scenes	41	50
Acquisition period	16 Jan 2015-13 May 2020	9 June 2015-19 May 2020
Relative orbit	102	95
Central incidence angle	38.77 degree	38.79 degree
Acquisition mode	Interferometry Wide swath (IW)	
Product type	Single Look Complex (SLC)	
Polarization	VV	

For data processing, the SLC images are co-registered to a single master. Then, the 50 m grid local digital elevation model (DEM), provided by the National Land Survey of Sweden (*Lantmäteriet*), and the precise orbits for each image were used to remove the topographic and flat earth components, respectively. Reference points were chosen among the selected Persistent Scatter Candidates (PSCs), which are relatively unaffected by deformation. Identification of the (PSCs), and (PS) was performed based on the amplitude stability index and the temporal coherence.

The first and second sets of data i.e. the 41 ascending and 50 descending images, were used to analyze the land surface of the study area. We used the images dated by 2016-11-06 (for ascending) and 2017-11-13 (for descending) as a master images, respectively, according to certain characteristics including the length of the baseline, where a high stack coherence was achieved. The atmospheric phase screen (APS) effect was estimated and removed based on amplitude stability indexes of 0.7 and 0.8 as quality parameters for the ascending and descending datasets respectively, and temporal coherence of 0.6 was used for masking purposes. For each dataset, the LOS velocity and displacement time series were estimated using a linear model. To ensure reliable

results the two reference points with zero displacements were selected in the same very stable area and away from the known deformed zones.

A long record of leveling measurements has been conducted and processed by the municipality of the city of Gävle and partially by the University of Gävle, covering the period from 1974 to 2019. This data was also used to examine the obtained PSI results as well as to analyze the stability of some locations in the study area.

At the outlet of the Gulf of Gävle, the Gävleån River, which crosses the city, formed large delta, which has been covered using fill material accordingly and used for urban development. In addition, the associated small river arms are also channelled or have been filled. By combining the geological information of Gävle city with the resulted PSI deformation map, it is possible to assess the risk of land movement in the city.

The combined ascending and descending PSI results and their rate of vertical movement were analyzed based on the provided quaternary deposit map by the Geological Survey of Sweden (SGU) (Figure 4.6). The PS points were overlaid on the geological map where the rate of displacement is evaluated accordingly. By using SARPROZ software and considering 0.6 as temporal coherence mask, the total of 7265 and 9314 PS points were obtained using ascending and descending geometries respectively.

Table 4.4. Comparison between the computed precise leveling rates (Pre. Lev) using four different levelling records relative to four different BMs, and the relative vertical rate of the generated combined PS points in the four validation buildings using the ascending and descending combination of the 41 and 50 SAR images respectively, collected between 2015 to 2020 (see Figure 1 in **Paper V**).

Validation site	Method	Track	Point ID	Relative Vertical Displacement rate (mm/year)	Relative Vertical Cumulative Displacement (mm)	Coherence
Building-1						
(1985-2019)	Pre. Lev		Point 7	- 1.2	-45.0	
(2015-2020)	PSI	AD	498	- 0.9	-5.0	0.86
Building-2						
(2000-2019)	Pre. Lev		Point 6	-0.8	-20.0	
(2015-2020)	PSI	AD	430	-0.7	-5.0	0.88
Building-3						
(1976-1982)	Pre. Lev		Point 6	-2.0	-10.0	
(2015-2020)	PSI	AD	396	-0.6	-4.1	0.95
Building-4						
(1974-1988)	Pre. Lev		Point 4	-1.8	-31.0	
(2015-2020)	PSI	AD	418	0.0	-1.6	0.97

The obtained results show that Gävle city is relatively stable with exceptions of some localized subsiding zones (Figure 4.5). The detected risk zones shows a maximum displacement rate that reaches up to -6 mm/year in the LOS direction. To the northwest of Area-1 (i.e. in Gävle railway station's marshalling yard), the area A5 is experiencing average subsidence ranging from -1 ± 0.47 mm/year to -3 ± 0.53 mm/year. The rest of the city, including the city centre, is almost relatively stable with minor deformation rates ranged between -2.0 mm/year to $+2.0$ mm/year in vertical and East-West components. A comparison between the computed precise leveling rates and the relative vertical rate of the generated PS points in the four validation buildings shows close agreement in Buildings 1 and 2 (see Figure 1 in Paper V). According to the correlation analysis between the obtained PSI results and the geological information of the city, the achieved result is highly correlated with the quaternary deposit map, e.g. in the detected risk zone that is reported as an artificial fill area (Figure 4.6).

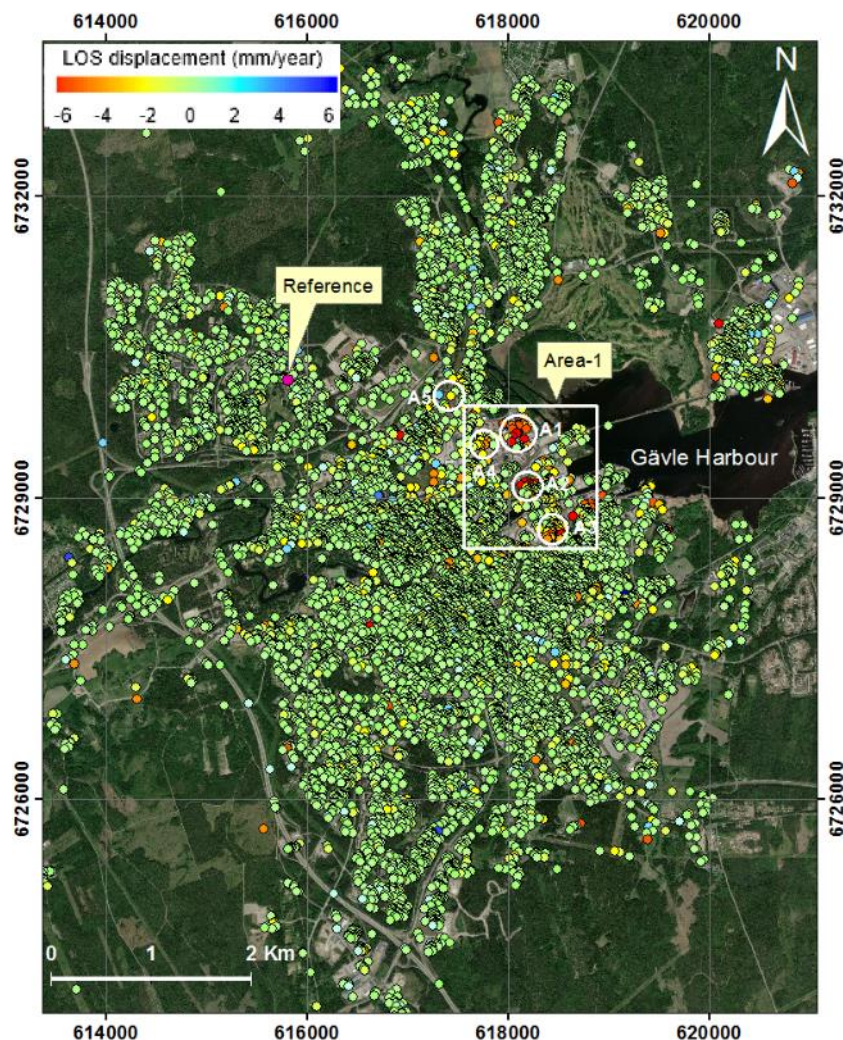


Figure 4.5. LOS displacement rates of all generated descending PS points in Gävle city relative to the reference point (pink color). Area-1 shows the maximum displacement zone. A1, A2, A3, A4, and A5 refer to the five different small areas. The observation period is from June 2015 to May 2020.

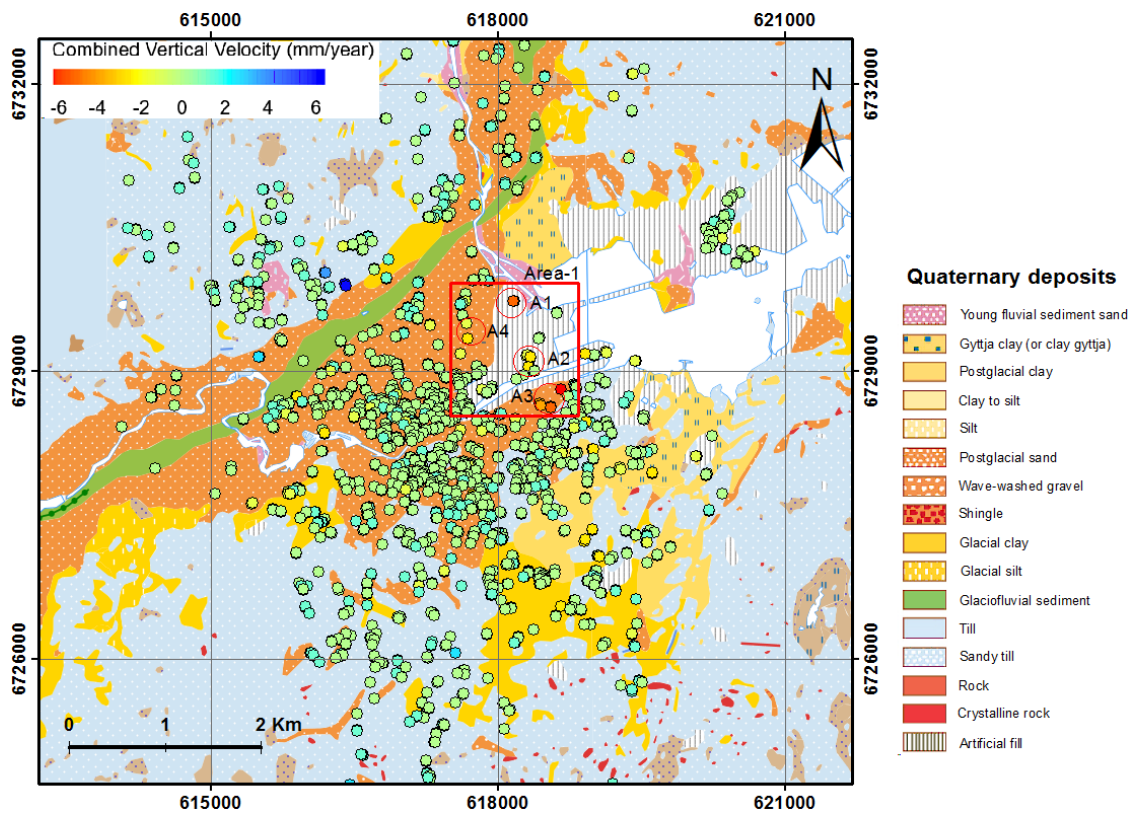


Figure 4.6. The vertical displacement rate of the combined ascending and descending PS points overlaid on the quaternary deposits map of the city of Gävle. Negative values denote for subsidence, while the positive denotes for uplift. Base map: Quaternary deposit © Geological Survey of Sweden (SGU). Coordinate system: SWEREF 99. Unit: mm/year.

Chapter 5

Conclusions and outlook

The study and monitoring of lithospheric deformation, geohazards, and environmental assessment using satellite data help us to better understand the ongoing processes in the Earth's surface and its interior. Based on five peer-reviewed papers, comprehensive studies about monitoring the Earth's lithospheric deformation by satellite geodesy and in situ data were carried out in this thesis. Different observation techniques and methods were employed to achieve this goal. As such the GRACE and SAR satellite missions were used due to their large coverage and reasonable expected results. The data processing step is the most challenging issue for studying the above-mentioned applications. For example, employing the best smoothing filter for GRACE data, using the appropriate hydrological and GIA models, and terrestrial data for evaluation of satellite-derived quantities are crucial.

A brief summary, and the main outcomes of each paper is provided here:

In the first paper, the horizontal sub-crustal stress and its temporal changes induced by crustal motions in Fennoscandia e.g. due to ongoing mantle convection were estimated. The static sub-lithospheric horizontal stress was determined using Runcorn and gravimetric-isostatic models. The sub-crustal stress temporal changes were obtained using 14 years of the CSR GRACE dataset, covered the period between 2003 and 2016. Moreover, an alternative gravimetric approach combined with Runcorn's method was utilized to estimate absolute sub-crustal stress. To determine the stress the disturbing gravity signals should be filtered. The gravity signals related to the lower mantle and core masses were filtered in order to determine the horizontal stress, using 5 to 40 spherical harmonic degrees according to *Bowin (2000)*. Because of the likely mixture of different gravitational effects in the Earth (e.g. plate tectonics). The numerous dominant geodynamical processes in Fennoscandia (e.g. mantle convection, horizontal and vertical motion due to GIA and plate tectonics) are likely the reasons for such stresses. For validation, *Bowin's* outcomes were correlated with NKG2005 land uplift model, which result in highly correlated coefficients. Using this outcomes, the estimated absolute stress result shows its maximum close to the centre of the land uplift dome and decreases around the ice margin. The estimated horizontal stress rates using gravity changes data, which is within 95 kpa/year, show that the GPS stations

(where the stresses were estimated) outside the uplift dome experience more horizontal stress than the stations inside the dome, because of the thinner lithosphere which produces higher stress changes.

In the second paper, permafrost thawing and its associated gravity change, in terms of groundwater storage anomalies (ΔGWS) changes was studied using the GRACE data and other satellites and ground-based observations in the northern high-latitude regions. The most significant factor for a careful monitoring of the permafrost thawing is its probable contribution for releasing an additional enormous amount of greenhouse gases to the atmosphere, most important are the carbon dioxide and methane. In this study, we focused on a large-scale permafrost monitoring as well as an identification of permafrost hotspots in terms of the GRACE-based ΔGWS changes. The total water storage (ΔTWS) change were estimated firstly based on the CSR GRACE solutions covered the period between August 2002 and May 2016. The effect of the GIA signal was estimated in terms of equivalent water height change and subtracted from the estimated ΔTWS rates. Moreover, the rate of changes of the hydrological surface signals were estimated and subtracted as well from the ΔTWS using GLDAS NOAHv1.0 hydrological model. The GIA and GLDAS models were used to correct the gravity signal. The results show the significant effects of the GIA on the determination of the water storage changes. Permafrost thawing might be detected with the positive values of the estimated equivalent water height, and it quantifies the increase in the ground water storage. To compare the obtained results with the greenhouse gases and temperature in the study area, four selected station were utilized (Siberia, North of Alaska, and Canada (Yukon and Hudson Bay)). We showed that the ground water storage is changing by up to 3.4, 3.8, 4.4 and 4.0 cm/year in this stations, respectively, most probably due to permafrost thawing. We also illustrated those greenhouse gases, increased up to 2.2 PPM/year in the study areas over the same period. Temperature also shows positive trend generally and in the study area as well as CO_2 and equivalent water height trend (due to permafrost thawing) which might confirm the permafrost carbon feedback process.

The third paper investigates the large-scale GRACE-based ΔGWS changes together with different hydrological models over the major oil reservoirs in Sudan. The outcomes are correlated with the available oil wells production data. The availability of in situ data in the Muglad basin (i.e. oil data) is the reason to perform this study in this area. Moreover, using the freely available Sentinel-1 data, the ground surface deformation associated with oil and water depletion is studied. For this purposes, the mass variations were estimated in terms of the ΔGWS change and surface deformation in the study region. Firstly, large-scale TWS anomalies (ΔTWS) were studied using CSR GRACE monthly solutions. Both non-isotropic DDK filters and a conventional Gaussian spatial smoothing function with 300 and 500 km smoothing radiuses were utilized to investigate the effect of applying different filters on our ΔGWS estimates over regional scales. To quantify the ΔGWS variations over the area, the estimated

hydrological signal was subtracted from the estimated GRACE-based Δ TWS. Different hydrological models (GLDAS and WGHM models) were used and investigated for this purpose. The results show that using different GRACE filters and hydrological models will result in different patterns of rates of Δ GWS changes. As the total mass extraction (i.e. oil production) should agree with the estimated Δ GWS, the evaluation of the different filters and hydrological models was based on the available oil production data. The correlation coefficients between the monthly total oil extraction and the estimated Δ GWS change using different smoothing filters and hydrological models in the Heglig-area oil fields, reveals a good agreement when using DDK1 filter and CLSM hydrological model (with a correlation coefficient of about 0.74). Except for the resolution of GRACE data, the main source of uncertainty in the estimated Δ GWS is related to the hydrological models, which reveal a strong relation with the rainfall trend in the region. According to the achieved results, GRACE data can help to monitor the mass changes due to heavy oil productions, if we could solve remarkable uncertainty in hydrological models in the future. Moreover, our Sentinel-1 SAR data analysis using Persistent Scatterer Interferometry (PSI) method shows high rate of subsidence ranged between -6 ± 0.88 and -24.5 ± 0.85 mm/year in the study area.

In the fourth paper, a combined Moho model using seismic and gravity data is determined to investigate the relationship between the isostatic state of the lithosphere and seismic activities in the study area (including East Africa, Egypt, Congo and Saudi Arabia). Moreover, the sub-crustal horizontal stress and its relationship with seismicity that is modeled using a gravimetric method was investigated. To do so, the least squares adjustment technique was used to combine the seismic (Baranov 2010) and gravimetric-isostatic (VMM) models. Additive corrections were estimated using CRUST1.0 and Earth2014 models. The results show that the combined method is less affected by the limitation of the seismic (spars data) and gravimetric-isostatic models (e.g. unmodeled non-isostatic effects, etc.). The isostatic equilibrium and compensation state are closely correlated to the seismicity patterns in the study area. Furthermore, low-density contrasts and thin crust near the triple junction plate tectonics in Afar were revealed which confirms the state of over-compensation in the rift valley areas. A possible correlation can be observed between the crustal depth, isostatic anomaly, density contrast, and earthquake activities in the region.

The last and fifth paper investigates the ground surface deformation of Gävle city in Sweden using Sentinel-1 data and PSI technique, as well as analyzing the historical leveling data. The PSI technique is used to map the location of risk zones, and their ongoing subsidence rate. For this purpose, two data sets of Sentinel-1 radar images in ascending and descending geometries, covering period between Jan 2015 to May 2020, were processed and analysed using SARPROZ software. Available long records of precise leveling data, back to early 70s, were utilized to examine the obtained PSI

results. The results show that Gävle city is relatively stable with exceptions of some risk zone areas and sparse points. The detected risk zone areas show a maximum displacement rate that reaches up to -6 mm/year. The comparison at sparse locations shows a close agreement between the subsidence rates obtained from precise leveling and PSI results. The local quaternary deposit distributions was correlated with PSI results, and it shows that the subsidence areas are mostly located in zones where the sub-surface layer is marked by artificial fill materials.

5.1 Future studies

GRACE data are still less sensitive for local scale regions. The sparsity or lack of in situ data affects the accuracy of the hydrological models, especially in the developing regions (e.g. Africa). Moreover, the availability of the SAR data with suitable frequency bands over some regions limit the usage of this technique in some areas. However, despite these limitations (i.e. different resolutions and applications) the GRACE, hydrological models, and InSAR can provide complementary data for such studies. During this study, we have had the opportunity to work and use different sorts of data (satellites and in situ data) to study and investigate various geodynamical and geophysical processes in regional and local scales. However, these studies may initiate some new research works such as:

- Using the GRACE and GRACE-FO data for further analyzing of mass redistribution with its uncertainties e.g. permafrost phenomena and ongoing sub-crustal stress determination studies.
- Using long record of L-band and C-band SAR data (e.g. Envisat) to combine with GRACE and GRACE-FO data for investigation of ground subsidence related to oil production in, for instance Sudan's oil field.
- Employing different hydrological and GIA models for analyzing permafrost using GRACE data (we used only GLDAS NOAHv1.0 model).
- Downscaling GRACE data by employing machine learning-based downscaling algorithms and using in situ and hydrological data for mass transportation studies e.g. mass depletion and permafrost.
- Localized permafrost monitoring using GRACE and SAR techniques (e.g. Siberia), where the related surface deformation can be evaluated.
- Using SAR technique to monitor the ground deformation along plate tectonic boundaries (e.g. in Afar triple junction) in Africa. Previous studies showed that there are significant vertical movements in this area that is very important for geohazard monitoring.
- Analyzing the relationship between groundwater level (obtained from wells data using the Geological Survey of Sweden, SGU, dataset) and ground subsidence detected by the SAR technique in the urban areas.

Author's contributions

Paper I: M.B. initiated the idea and helped to write and prepare the manuscript. I wrote the manuscript, processed, and analyzed the data. L.S. contributed to the interpretation and editing of the manuscript.

Paper II: M.B. initiated the idea with the help of I, and he helped to write and prepare the manuscript. I wrote the manuscript, processed, and analyzed the data. L.S. and R.T. contributed to the interpretations and editing of the manuscript.

Paper III: I initiated the idea, wrote the manuscript, processed, and analyzed the data. H.A. carried out part of data processing and helped to draft the manuscript. M.B. helped to design, write, data processing, and prepare the manuscript. F.M. contributed to data processing and edited the manuscript.

Paper IV: M. Bagherbandi designed the study and helped to write and prepare the manuscript. I wrote the manuscript, processed, and analyzed the data.

Paper V: I initiated the idea, wrote the manuscript, processed, and analyzed the data. M.B. helped to design, write and prepare the manuscript. F.N. contributed to the interpretation and editing of the manuscript.

References

- Ågren J, Svensson R (2007) Postglacial land uplift model and system definition for the new Swedish height system RH 2000. Lantmäteriet-Rapport
- Airy GB (1855) On the Computation of the Effect of the Attraction of Mountain Masses as disturbing the Apparent Astronomical Latitude of Stations in Geodetic Surveys. *Mon Not R Astron Soc.* <https://doi.org/10.1093/mnras/16.2.42>
- Amin H, Bagherbandi M, Sjöberg LE (2020) Quantifying barystatic sea-level change from satellite altimetry, GRACE and Argo observations over 2005–2016. *Adv Sp Res.* <https://doi.org/10.1016/j.asr.2020.01.029>
- Artemjev ME, Bune VI, Dubrovsky VA, Kambarov NS (1972) Seismicity and isostasy. *Phys Earth Planet Inter.* [https://doi.org/10.1016/0031-9201\(72\)90009-X](https://doi.org/10.1016/0031-9201(72)90009-X)
- Azadnejad S, Maghsoudi Y, Perissin D (2019) Investigating the effect of the physical scattering mechanism of the dual-polarization sentinel-1 data on the temporal coherence optimization results. *Int J Remote Sens.* <https://doi.org/10.1080/01431161.2019.1597309>
- Bagherbandi M (2011) An isostatic Earth crustal thickness model and its applications. PhD thesis. Royal Institute of Technology (KTH), 2011.
- Bagherbandi M, Gido NAA (*Submitted*) A study on the relationship between isostatic equilibrium and seismicity: A case study in Africa.
- Bagherbandi M, Sjöberg LE (2012) Non-isostatic effects on crustal thickness: A study using CRUST2.0 in Fennoscandia. *Phys Earth Planet Inter.* <https://doi.org/10.1016/j.pepi.2012.04.001>
- Bagherbandi M, Tenzer R, Sjöberg LE, Novák P (2013) Improved global crustal thickness modeling based on the VMM isostatic model and non-isostatic gravity correction. *J Geodyn.* <https://doi.org/10.1016/j.jog.2013.01.002>
- Baker ML Robert (1960) Orbit determination from range and range-rate data. ARS Preprint 1220-60, May
- Balzter H (2001) Forest mapping and monitoring with interferometric synthetic aperture radar (InSAR). *Prog Phys Geogr.* <https://doi.org/10.1191/030913301666986397>
- Bamler R, Hartl P (1998) Synthetic aperture radar interferometry. *Inverse Probl.* <https://doi.org/10.1088/0266-5611/14/4/001>
- Baranov AA (2010) A new crustal model for central and Southern Asia. *Izv Phys Solid Earth.* <https://doi.org/10.1134/S1069351310010039>
- Bechtel TD, Forsyth DW, Swain CJ (1987) Mechanisms of isostatic compensation in the vicinity of the East African Rift, Kenya. *Geophys J R Astron Soc.* <https://doi.org/10.1111/j.1365-246X.1987.tb00734.x>
- Becker TW, O'Connell RJ (2001) Lithospheric stresses caused by mantle convection: the role of plate rheology. Am Geophys Union, Fall Meeting 2001, abstract #T12C-0921.

- Bettadpur S (2012) CSR Level-2 Processing Standards Document for Product Release 05 GRACE, The GRACE Project, Center for Space Research, University of Texas at Austin, 2012, pp. 327e742.
- Bevis M, Melini D, Spada G (2016) On computing the geoelectric response to a disk load. *Geophys J Int.* <https://doi.org/10.1093/gji/ggw115>
- Blewitt G, Clarke P (2003) Inversion of Earth's changing shape to weigh sea level in static equilibrium with surface mass redistribution. *J Geophys Res Solid Earth.* <https://doi.org/10.1029/2002jb002290>
- Bowie W (1926) Relation of earthquakes to isostasy. *Eos, Trans Am Geophys Union.* <https://doi.org/10.1029/TR007i001p00072>
- Bowin C (2000) Mass anomaly structure of the Earth. *Rev Geophys.* <https://doi.org/10.1029/1999RG000064>
- Bürgmann R, Rosen PA, Fielding EJ (2000) Synthetic Aperture Radar Interferometry to Measure Earth's Surface Topography and Its Deformation. *Annu Rev Earth Planet Sci.* <https://doi.org/10.1146/annurev.earth.28.1.169>
- Čadež O, Martinec Z (1991) Spherical harmonic expansion of the Earth's crustal thickness up to degree and order 30. *Stud Geophys Geod.* <https://doi.org/10.1007/BF01614063>
- Castellazzi P, Longuevergne L, Martel R, et al (2018) Quantitative mapping of groundwater depletion at the water management scale using a combined GRACE/InSAR approach. *Remote Sens Environ.* <https://doi.org/10.1016/j.rse.2017.11.025>
- Castellazzi P, Martel R, Galloway DL, Longuevergne L, Rivera A (2016) Assessing Groundwater Depletion and Dynamics Using GRACE and InSAR: Potential and Limitations. *Groundwater* 2016, vol. 54, 6, pages 768-780
- Cazenave A, Chen J (2010) Time-variable gravity from space and present-day mass redistribution in the Earth system. *Earth Planet Sci Lett.* <https://doi.org/10.1016/j.epsl.2010.07.035>
- Chao BF (2005) On inversion for mass distribution from global (time-variable) gravity field. *J Geodyn.* <https://doi.org/10.1016/j.jog.2004.11.001>
- Chen J (2019) Satellite gravimetry and mass transport in the earth system. *Geod Geodyn.* <https://doi.org/10.1016/j.geog.2018.07.001>
- Chen J, Li J, Zhang Z, Ni S (2014) Long-term groundwater variations in Northwest India from satellite gravity measurements. *Glob Planet Change.* <https://doi.org/10.1016/j.gloplacha.2014.02.007>
- Cheng M, Ries J (2017) The unexpected signal in GRACE estimates of C20. *J Geod.* <https://doi.org/10.1007/s00190-016-0995-5>
- Cheng M, Tapley BD (1999) Seasonal variations in low degree zonal harmonics of the Earth's gravity field from satellite laser ranging observations. *J Geophys Res Solid Earth.* <https://doi.org/10.1029/1998jb900036>

- Closa, J. (2008). The influence of orbit precision in the quality of ERS SAR interferometric data. Tech. Rep. ES-TN-APP-APM-JC01, ESA, 1998. Available at: http://earth.esa.int/ers/sysutil/ORB_QL.html.
- Colesanti C, Ferretti A, Perissin D, Prati C, Rocca F (2003) ERS-ENVISAT Permanent Scatterers Interferometry, in *Proceedings of the IEEE International Geoscience and Remote Sensing Symposium – IGARSS 2003, Toulouse (France)*, 2003, p. Pages: 1130 – 1132.
- Costantini M (1998) A novel phase unwrapping method based on network programming, *IEEE Trans. Geosci. Remote Sensing*, vol. 36, pp. 813–821, 1998.
- Cox CM, Chao BF (2002) Detection of a large-scale mass redistribution in the terrestrial system since 1998. *Science* (80-). <https://doi.org/10.1126/science.1072188>
- Crétau J-F, Soudarin L, Davidson FJM, et al (2002) Seasonal and interannual geocenter motion from SLR and DORIS measurements: Comparison with surface loading data. *J Geophys Res Solid Earth*. <https://doi.org/10.1029/2002jb001820>
- Crosetto M, Monserrat O, Cuevas-González M, et al (2015) Measuring thermal expansion using X-band persistent scatterer interferometry. *ISPRS J Photogramm Remote Sens*. <https://doi.org/10.1016/j.isprsjprs.2014.05.006>
- Crosetto M, Monserrat O, Cuevas-González M, et al (2016) Persistent Scatterer Interferometry: A review. *ISPRS J. Photogramm. Remote Sens*.
- Curlander, J.C., McDonough, R.N. (1991). *Synthetic Aperture Radar: Systems and Signal Processing*. New York: Wiley-Intersci. 647 pp
- Dahle C, Flechtner F, Gruber C, König D, König R, Michalak G, Neumayer K-H (2013) GRACE Level-2 Processing Standards Document for Level-2 Product Release 0005, Scientific Technical Report STR12/02 Data, GFZ, Postdam, 2013.
- Dickey JO, Marcus SL, De Viron O, Fukumori I (2002) Recent earth oblateness variations: Unraveling climate and postglacial rebound effects. *Science* (80-). <https://doi.org/10.1126/science.1077777>
- Döll P, Fritsche M, Eicker A, Müller Schmied H (2014a) Seasonal Water Storage Variations as Impacted by Water Abstractions: Comparing the Output of a Global Hydrological Model with GRACE and GPS Observations. *Surv Geophys*. <https://doi.org/10.1007/s10712-014-9282-2>
- Döll P, Kaspar F, Lehner B (2003) A global hydrological model for deriving water availability indicators: Model tuning and validation. *J Hydrol*. [https://doi.org/10.1016/S0022-1694\(02\)00283-4](https://doi.org/10.1016/S0022-1694(02)00283-4)
- Döll P, Müller Schmied H, Schuh C, et al (2014b) Global-scale assessment of groundwater depletion and related groundwater abstractions: Combining hydrological modeling with information from well observations and GRACE satellites. *Water Resour Res*. <https://doi.org/10.1002/2014WR015595>
- Dong D, Gross RS, Dickey JO (1996) Seasonal variations of the Earth's gravitational field: an analysis of atmospheric pressure, ocean tidal, and surface water excitation. *Geophys Res Lett*. <https://doi.org/10.1029/96GL00740>

- Eicker A, Schumacher M, Kusche J, et al (2014) Calibration/Data Assimilation Approach for Integrating GRACE Data into the WaterGAP Global Hydrology Model (WGHM) Using an Ensemble Kalman Filter: First Results. *Surv Geophys*. <https://doi.org/10.1007/s10712-014-9309-8>
- Ekman M (1991) A concise history of postglacial land uplift research (from its beginning to 1950). *Terra Nov*.
- Elachi C (1988) *Space borne Radar Remote Sensing: Applications and Techniques*. New York: IEEE. 255 pp.
- ESA, Reports for Mission Selection (1999) Gravity Field and Steady-State Ocean Circulation Mission. SP-1233(1), ESA Publication Division, ESTEC, Noordwijk, The Netherlands (available from web site, <http://www.esa.int/livingplanet/goce>)
- Eshagh M (2015) On the relation between Moho and sub-crustal stress induced by mantle convection. *J Geophys Eng*. <https://doi.org/10.1088/1742-2132/12/1/1>
- Eshagh M, Tenzer R (2015) Sub-crustal stress determined using gravity and crust structure models. *Comput Geosci*. <https://doi.org/10.1007/s10596-014-9460-9>
- Famiglietti JS, Lo M, Ho SL, et al (2011) Satellites measure recent rates of groundwater depletion in California's Central Valley. *Geophys Res Lett*. <https://doi.org/10.1029/2010GL046442>
- Farrell WE (1972) Deformation of the Earth by surface loads. *Rev. Geophys*.
- Ferretti A, Prati C, Rocca F (2000) Nonlinear subsidence rate estimation using permanent scatterers in differential SAR interferometry. *IEEE Trans Geosci Remote Sens*. <https://doi.org/10.1109/36.868878>
- Ferretti A, Prati C, Rocca F (2001) Permanent scatterers in SAR interferometry. *IEEE Trans Geosci Remote Sens*. <https://doi.org/10.1109/36.898661>
- Foroughnia F, Nemati S, Maghsoudi Y, Perissin D (2019) An iterative PS-InSAR method for the analysis of large spatio-temporal baseline data stacks for land subsidence estimation. *Int J Appl Earth Obs Geoinf*. <https://doi.org/10.1016/j.jag.2018.09.018>
- Freek van Leijen, (2014) *Persistent Scatterer Interferometry based on geodetic estimation theory*. Delft University of Technology, 2014
- Fryksten J, Nilfouroushan F (2019) Analysis of clay-induced land subsidence in Uppsala City using Sentinel-1 SAR data and precise leveling. *Remote Sens*. <https://doi.org/10.3390/rs11232764>
- Gabriel AK, Goldstein RM, Zebker HA (1989) Mapping small elevation changes over large areas: differential radar interferometry. *J Geophys Res*. <https://doi.org/10.1029/JB094iB07p09183>
- Galloway DL, Hoffmann J (2007) The application of satellite differential SAR interferometry-derived ground displacements in hydrogeology. *Hydrogeology Journal* 2007, 15, no. 1: 133–154.

- Gernhardt SM (2011). High Precision 3D Localization and Motion Analysis of Persistent Scatterers using Meter-Resolution Radar Satellite Data. Technische Universität Munchen. 2011.
- Ghiglia DC, Pritt MD (1998) Two-dimensional phase unwrapping: theory, algorithms, and software
- Gido NAA, Amin H, Bagherbandi M, Nilfouroushan F (2020) Satellite monitoring of mass changes and ground subsidence in Sudan's oil fields using GRACE and Sentinel-1 data. *Remote Sens.* 2020, 12, 1792.
- Gido NAA, Bagherband, M, Nilfouroushan F (*Submitted*) Localized subsidence zones in Gävle City detected by Sentinel-1 PSInSAR and Leveling data.
- Gido NAA, Bagherbandi M, Sjöberg LE (2019) A gravimetric method to determine horizontal stress field due to flow in the mantle in Fennoscandia. *Geosci J* 23:. <https://doi.org/10.1007/s12303-018-0046-8>
- Gido NAA, Bagherbandi M, Sjöberg LE, Tenzer R (2019) Studying permafrost by integrating satellite and in situ data in the northern high-latitude regions. *Acta Geophys* 67:. <https://doi.org/10.1007/s11600-019-00276-4>
- Gladkikh V, Tenzer R (2012) A mathematical model of the global ocean saltwater density distribution. *Pure and Applied Geophysics* 169(1-2): 249-257
- Goldstein RM, Werner CL (1998) Radar interferogram filtering for geophysical applications. *Geophys Res Lett.* <https://doi.org/10.1029/1998GL900033>
- Güntner A, Stuck J, Werth S, et al (2007) A global analysis of temporal and spatial variations in continental water storage. *Water Resour Res.* <https://doi.org/10.1029/2006WR005247>
- Haas R, Scherneck H-G, Gueguen E, Nothnagel A, Campbell J (2002) Large-scale strain-rates in Europe derived from observations in the European geodetic VLBI network. *European Geosciences Union 2002 (EGU) Stephan Mueller Special Publication Series, vol 2*, pp 139–152.
- Han SC, Shum CK, Jekeli C, et al (2005) Non-isotropic filtering of GRACE temporal gravity for geophysical signal enhancement. *Geophys J Int.* <https://doi.org/10.1111/j.1365-246X.2005.02756.x>
- Hanssen RF (2001) *Radar Interferometry: Data Interpretation and Error Analysis (Remote Sensing and Digital Image Processing)*
- Heiskanen WA, Moritz H (1967) *Physical geodesy.* *Bull Géodésique.* <https://doi.org/10.1007/BF02525647>
- Heiskanen WA, Vening Meinesz FA (1958) *The Earth and its Gravity Field.* McGRAW-HILL Book Company, Inc. New York. 1958.
- Henry Pratt VJ (1855) On the Attraction of the Himalaya Mountains and of the elevated Regions beyond them, upon the Plumb-line in India. *Mon Not R Astron Soc.* <https://doi.org/10.1093/mnras/16.2.36>
- Hirt C, Rexer M (2015) *Earth2014: 1 arc-min shape, topography, bedrock and ice-sheet models*

- Available as gridded data and degree-10,800 spherical harmonics. *Int J Appl Earth Obs Geoinf.* <https://doi.org/10.1016/j.jag.2015.03.001>
- Hooper AJ, Segall P, Zebker H (2007) Persistent scatter radar interferometry for crustal deformation studies and modeling of volcanic deformation. *J Geophysical Res Solid Earth*
- Huang Z (2013) The Role of Glacial Isostatic Adjustment (GIA) Process On the Determination of Present-Day Sea-Level Rise. Ohio State University. Geodetic Science. Report. No. 504.
- Ilk KH (1983) Ein Beitrag zur Dynamik ausgedehnter Körper-Gravitationswechselwirkung. Deutsche Geodätische Kommission, Reihe C, Heft Nr. 288, München.
- Jekeli C (1981) Alternative methods to smooth the Earth's gravity field.
- Jin S, Chambers DP, Tapley BD (2010) Hydrological and oceanic effects on polar motion from GRACE and models. *J Geophys Res Solid Earth.* <https://doi.org/10.1029/2009JB006635>
- Joodaki G, Wahr J, Swenson S (2014) Estimating the human contribution to groundwater depletion in the Middle East, from GRACE data, land surface models, and well observations. *Water Resour Res.* <https://doi.org/10.1002/2013WR014633>
- Kaban MK, El Khrepy S, Al-Arifi N (2016) Isostatic Model and Isostatic Gravity Anomalies of the Arabian Plate and Surroundings. *Pure Appl Geophys.* <https://doi.org/10.1007/s00024-015-1164-0>
- Kampes BM (2006) Radar interferometry: Persistent scatterer technique
- Khan SA, Kjær KH, Bevis M, et al (2014) Sustained mass loss of the northeast Greenland ice sheet triggered by regional warming. *Nat Clim Chang.* <https://doi.org/10.1038/nclimate2161>
- Kierulf HP, Steffen H, Simpson MJR, et al (2014) A GPS velocity field for Fennoscandia and a consistent comparison to glacial isostatic adjustment models. *J Geophys Res Solid Earth.* <https://doi.org/10.1002/2013JB010889>
- Kusche J (2007) Approximate decorrelation and non-isotropic smoothing of time-variable GRACE-type gravity field models. *J Geod.* <https://doi.org/10.1007/s00190-007-0143-3>
- Kusche J, Schmidt R, Petrovic S, Rietbroek R (2009) Decorrelated GRACE time-variable gravity solutions by GFZ, and their validation using a hydrological model. *J Geod.* <https://doi.org/10.1007/s00190-009-0308-3>
- Laske G, Masters G, Ma Z, Pasyanos M (2013) Update on CRUST1.0---A 1-degree global model of Earth's crust. In: EGU General Assembly 2013
- Laske, G, Masters, G, Reif, C, (2000) A New Global Crustal Model at 2x2 Degrees (CRUST2.0). <http://igppweb.ucsd.edu/~gabi/crust2.html>.
- Massonnet D, Feigl KL (1998) Radar interferometry and its application to changes in the earth's surface. *Rev Geophys.* <https://doi.org/10.1029/97RG03139>
- Mooney WD, Laske G, Masters G (1998) CRUST 5.1: A global crustal model at 5 degrees x 5 degrees. *J Geophys Res Earth*

- Moritz H (1990) The inverse Vening Meinesz problem in isostasy. *Geophys J Int.* <https://doi.org/10.1111/j.1365-246X.1990.tb04591.x>
- Moritz H (2000) Geodetic Reference System 1980. *J Geod.* <https://doi.org/10.1007/s001900050278>
- Müller Schmied H (2017) Evaluation, modification and application of global hydrological model. Frankfurt Hydrology Paper 16, Institute of Physical Geography, Goethe University Frankfurt, Frankfurt am Main. https://fiona.server.uni-frankfurt.de/default/65883413/Mueller_Schmied_2017_evaluation_modification_and_application_of_a_global_hydrological_model.pdf.
- Müller Schmied H, Eisner S, Franz D, Wattenbach M, Portmann FT, Flörke M, Döll P (2014) Sensitivity of simulated global-scale freshwater fluxes and storages to input data, hydrological model structure, human water use and calibration. *Hydrology and Earth System Sciences*, 18, 3511-3538. doi:10.5194/hess-18.3511-2014.
- Mullissa AG, Perissin D, Tolpekin VA, Stein A (2018) Polarimetry-Based Distributed Scatterer Processing Method for PSI Applications. *IEEE Trans Geosci Remote Sens.* <https://doi.org/10.1109/TGRS.2018.2798705>
- Noomen R, Springer TA, Ambrosius BAC, et al (1996) Crustal deformations in the Mediterranean area computed from SLR and GPS observations. *J Geodyn.* [https://doi.org/10.1016/0264-3707\(95\)00015-1](https://doi.org/10.1016/0264-3707(95)00015-1)
- Pail R, Fecher T, Barnes D, Factor J, Holmes S, Gruber T, Zingerle P (2017) The experimental gravity field model XGM2016. GFZ Data Services 2017. <http://doi.org/10.5880/icgem.2017.003>.
- Parizzi A, Perissin D, Prati C, Rocca F (2005) "Artificial Scatterers in SAR Interferometry," in *Proceedings of Dragon Symposium 2005, Santorini (Greece)*, 2005.
- Pavlis NK, Holmes SA, Kenyon SC, Factor JK (2012) The development and evaluation of the Earth gravitational model 2008 (EGM2008). *J Geophys Res* 117:B04406
- Peltier WR (2004) GLOBAL GLACIAL ISOSTASY AND THE SURFACE OF THE ICE-AGE EARTH: The ICE-5G (VM2) Model and GRACE. *Annu Rev Earth Planet Sci.* <https://doi.org/10.1146/annurev.earth.32.082503.144359>
- Peltier WR, Argus DF, Drummond R (2015) Space geodesy constrains ice age terminal deglaciation: The global ICE-6G-C (VM5a) model. *J Geophys Res Solid Earth.* <https://doi.org/10.1002/2014JB011176>
- Perissin D, Prati C, Engdahl M, Desnos Y-L (2006) "Validating the SAR Wave-Number Shift Principle with ERS-Envisat PS Coherent Combination," *IEEE Transactions on Geoscience and Remote Sensing*, vol. Volume 44, p. Pages: 2343 – 2351. 2006
- Perissin D, Wang T (2011) Time-Series InSAR Applications Over Urban Areas in China. *IEEE J Sel Top Appl Earth Obs Remote Sens.* <https://doi.org/10.1109/JSTARS.2010.2046883>
- Petrovskaya MS, Vershkov AN (2006) Non-singular expressions for the gravity gradients in the local north-oriented and orbital reference frames. *J Geod.* <https://doi.org/10.1007/s00190-006-0031-2>

- Pick M. (1994) Geoid and tectonic forces. P. Vanicek and N. Christou (eds.): Geoid and its geophysical interpretation. CRC Press, Inc., Boca Raton, Ann Arbor, London, Tokyo, Chap. 12.
- Reigber C, Schwintzer P, Lühr H (1999) The CHAMP geopotential mission. *Boll di Geofis Teor ed Appl*
- Roccheggiani M, Piacentini D, Tirincanti E, et al (2019) Detection and monitoring of tunneling induced ground movements using Sentinel-1 SAR interferometry. *Remote Sens.* <https://doi.org/10.3390/rs11060639>
- Rodell M, Famiglietti JS (1999) Detectability of variations in continental water storage from satellite observations of the time dependent gravity field. *Water Resour Res.* <https://doi.org/10.1029/1999WR900141>
- Rodell M, Houser PR, Jambor U, et al (2004) The Global Land Data Assimilation System. *Bull Am Meteorol Soc.* <https://doi.org/10.1175/BAMS-85-3-381>
- Rodell M, Houser PR, Jambor U, Gottschalck J, Mitchell K, Meng, C.-J, Arsenault K, Cosgrove B, Radakovich J, Bosilovich M, Entin JK, Walker JP, Lohmann D, Toll D (2004a) The Global Land Data Assimilation System. *Bull Am Meteorol. Soc.* 2004a, 85:381-394.
- Rodell M, Velicogna I, Famiglietti JS (2009) Satellite-based estimates of groundwater depletion in India. *Nature.* <https://doi.org/10.1038/nature08238>
- Runcorn SK (1967) Flow in the Mantle Inferred from the Low Degree Harmonics of the Geopotential. *Geophys J R Astron Soc.* <https://doi.org/10.1111/j.1365-246X.1967.tb06253.x>
- Scanlon BR, Longuevergne L, Long D (2012) Ground referencing GRACE satellite estimates of groundwater storage changes in the California Central Valley, USA. *Water Resour Res.* <https://doi.org/10.1029/2011WR011312>
- Schaeffer AJ, Lebedev S (2013) Global shear speed structure of the upper mantle and transition zone. *Geophys J Int.* <https://doi.org/10.1093/gji/ggt095>
- Scharroo R, Visser P (1998) Precise orbit determination and gravity field improvement for the ERS satellites. *J Geophys Res Ocean.* <https://doi.org/10.1029/97JC03179>
- Scherneck HG, Lidberg M, Haas R, et al (2010) Fennoscandian strain rates from BIFROST GPS: A gravitating, thick-plate approach. *J Geodyn.* <https://doi.org/10.1016/j.jog.2009.11.005>
- Schmidt R, Flechtner F, Meyer U, et al (2008) Hydrological signals observed by the GRACE satellites. *Surv. Geophys.*
- Schmied HM, Eisner S, Franz D, et al (2014) Sensitivity of simulated global-scale freshwater fluxes and storages to input data, hydrological model structure, human water use and calibration. *Hydrol Earth Syst Sci.* <https://doi.org/10.5194/hess-18-3511-2014>
- Simons M, Hager BH (1997) Localization of the gravity and the signature of glacial rebound. *Nature.* <https://doi.org/10.1038/37339>
- Sjöberg LE (1983) Unbiased estimation of variance covariance components in condition adjustment with unknowns a MINQUE approach. *Zeitschrift für Vermessungswesen*, 108, 9, pp. 382-387, 1983

- Sjöberg LE (1999) An efficient iterative solution to transform rectangular to geocentric coordinates. *Z Vermessungswesen* 126(9):295–297
- Sjöberg LE (2009) Solving Vening Meinesz-Moritz inverse problem in isostasy. *Geophys J Int.* <https://doi.org/10.1111/j.1365-246X.2009.04397.x>
- Sjöberg LE (2013) On the isostatic gravity anomaly and disturbance and their applications to vening meinesz-moritz gravimetric inverse problem. *Geophys J Int.* <https://doi.org/10.1093/gji/ggt008>
- Sjöberg LE, Bagherbandi M (2011) A method of estimating the Moho density contrast with a tentative application of EGM08 and CRUST2.0. *Acta Geophys.* <https://doi.org/10.2478/s11600-011-0004-6>
- Sjöberg LE, Bagherbandi M (2014) Isostasy – Geodesy. In: Grafarend E. (eds) *Encyclopedia of Geodesy*. Springer, Cham.
- Sjöberg LE, Bagherbandi M (2017) *Gravity Inversion and Integration*
- Skolnik MI (1990) *Radar Handbook* (second edition). McGraw Hill. <https://doi.org/10.1007/s10194-006-0268-4>
- Sun W, Sjöberg LE (1999) Gravitational potential changes of a spherically symmetric earth model caused by a surface load. *Geophys J Int.* <https://doi.org/10.1046/j.1365-246X.1999.00792.x>
- Swenson S, Chambers D, Wahr J (2008) Estimating geocenter variations from a combination of GRACE and ocean model output. *J Geophys Res Solid Earth.* <https://doi.org/10.1029/2007JB005338>
- Swenson S, Wahr J (2002) Methods for inferring regional surface-mass anomalies from Gravity Recovery and Climate Experiment (GRACE) measurements of time-variable gravity. *J Geophys Res Solid Earth.* <https://doi.org/10.1029/2001jb000576>
- Swenson S, Wahr J (2006) Post-processing removal of correlated errors in GRACE data. *Geophys Res Lett.* <https://doi.org/10.1029/2005GL025285>
- Tapley BD, Bettadpur S, Ries JC, et al (2004a) GRACE measurements of mass variability in the Earth system. *Science* (80-). <https://doi.org/10.1126/science.1099192>
- Tapley BD, Bettadpur S, Watkins M, Reigber C (2004b) The gravity recovery and climate experiment: Mission overview and early results. *Geophys Res Lett.* <https://doi.org/10.1029/2004GL019920>
- Tenzer R, Bagherbandi M (2012) Reformulation of the Vening-Meinesz Moritz Inverse Problem of Isostasy for Isostatic Gravity Disturbances. *Int J Geosci.* <https://doi.org/10.4236/ijg.2012.325094>
- Tenzer R, Chen W, Tsoulis D, Bagherbandi M, Sjöberg LE, Novák P, Jin S (2015) Analysis of the refined CRUST1.0 crustal model and its gravity field. *Surveys in Geophysics* 36(1): 139-165
- Tenzer R, Chen W, Tsoulis D, et al (2015) Analysis of the Refined CRUST1.0Crustal Model and its Gravity Field. *Surv. Geophys.*

- Tenzer R, Wenjin C, Tsoulis D, Bagherbandi M, Sjöberg LE, Nová P (2014) Analysis of the refined CRUST1.0 crustal model and its gravity field. *Surveys in Geophysics* **2014**, 36:139–165. Doi: 10.1007/s10712-12-014-9299-6.
- Tiwari VM, Wahr J, Swenson S (2009) Dwindling groundwater resources in northern India, from satellite gravity observations. *Geophys Res Lett.* <https://doi.org/10.1029/2009GL039401>
- Vaníček P, Tenzer R, Sjöberg LE, et al (2004) New views of the spherical Bouguer gravity anomaly. *Geophys J Int.* <https://doi.org/10.1111/j.1365-246X.2004.02435.x>
- Velicogna I, Wahr J (2006) Measurements of time-variable gravity show mass loss in Antarctica. *Science* (80-). <https://doi.org/10.1126/science.1123785>
- Vening-Meinesz FA (1931) Une nouvelle méthode pour la réduction isostatique régionale de l'intensité de la pesanteur. *Bull Géodésique*
- Voss KA, Famiglietti JS, Lo M, et al (2013) Groundwater depletion in the Middle East from GRACE with implications for transboundary water management in the Tigris-Euphrates-Western Iran region. *Water Resour Res.* <https://doi.org/10.1002/wrcr.20078>
- Wahr J, Molenaar M, Bryan F (1998) Time variability of the Earth's gravity field: Hydrological and oceanic effects and their possible detection using GRACE. *J Geophys Res Solid Earth.* <https://doi.org/10.1029/98jb02844>
- Wang T, Perissin D, Liao RF M (2010) "Three Gorges Dam Stability Monitoring with Time Series InSAR Analysis," *Science China Earth Sciences*, 2010.
- Watts AB (2001) *Isostasy and flexure of the lithosphere.* Cambridge University Press, Cambridge, U.K.
- Wei M, Sandwell DT (2010) Decorrelation of L-band and C-band interferometry over vegetated areas in California. *IEEE Trans Geosci Remote Sens.* <https://doi.org/10.1109/TGRS.2010.2043442>
- Wempen JM, McCarter MK (2017) Comparison of L-band and X-band differential interferometric synthetic aperture radar for mine subsidence monitoring in central Utah. *Int J Min Sci Technol.* <https://doi.org/10.1016/j.ijmst.2016.11.012>
- WOLFF M (1969) DIRECT MEASUREMENTS OF THE EARTH'S GRAVITATIONAL POTENTIAL USING A SATELLITE PAIR. *J Geophys Res*
- Wouters B, Schrama EJO (2007) Improved accuracy of GRACE gravity solutions through empirical orthogonal function filtering of spherical harmonics. *Geophys Res Lett.* <https://doi.org/10.1029/2007GL032098>
- Yoder CF, Williams JG, Dickey JO, et al (1983) Secular variation of Earth's gravitational harmonic J2 coefficient from Lageos and nontidal acceleration of Earth rotation. *Nature.* <https://doi.org/10.1038/303757a0>
- Zebker HA, Rosen PA, Hensley S (1997) Atmospheric effects in interferometric synthetic aperture radar surface deformation and topographic maps. *J Geophys Res Solid Earth.* <https://doi.org/10.1029/96jb03804>

Zhou X, Chang N Bin, Li S (2009) Applications of SAR interferometry in earth and environmental science research. Sensors

Published papers (I-V)